# Attribution of Seasonally Dependent Extreme Precipitation Characteristics in the Pearl River Delta Region to Anthropogenic Influences

**ZHAO, Rui**

A Thesis Submitted in Partial Fulfilment

of the Requirements for the Degree of

Doctor of Philosophy

in

Earth and Atmospheric Sciences

The Chinese University of Hong Kong

March 2022

# Thesis Assessment Committee

Professor LIU Lin (Chair)

Professor TAM Chi Yung Francis (Thesis Supervisor)

Professor TAI Pui Kuen Amos (Committee Member)

Professor GAN Thian Yew (External Examiner)

# Abstract

of thesis entitled:

**Attribution of Seasonally Dependent Extreme Precipitation Characteristics in the Pearl River Delta Region to Anthropogenic Influences**

Submitted by ZHAO, Rui

for the degree of Doctor of Philosophy

at The Chinese University of Hong Kong in March 2022

The Pearl River Delta (PRD) region, one of China's economic centers with a dense population, has experienced a rising trend in heavy precipitation that caused tremendous damage to society the environment. According to the Clausius–Clapeyron (CC) relation, a warmer climate mainly caused by human activity leads to ~7% increases in water vapor per degree warming, which is usually assumed to intensify heavy rainfall proportionally. Global warming may further affect precipitation via altering atmospheric circulation. This study explores the extent to which PRD heavy rainfall in different seasons responds to human influence by applying the pseudo global warming (PGW) method in the Weather Research and Forecasting (WRF) model integrated at a cloud-resolving spatial resolution of 2 km x 2 km.

We first conducted attribution analysis on 40 extreme rainfall events during 1998-2018 in PRD, including 23 cases from May to September (hereafter MJJAS) and 17 in the rest months (non-MJJAS). The model was forced to reproduce these cases with the factual and "counterfactual" conditions separately. The latter condition was achieved by deriving human-induced changes from differences between historical and natural runs from the Coupled Model Intercomparison Project Phase 5 (CMIP5) models, and then subtracting them from the factual condition (equivalent to the reverse of PGW). By comparing parallel experiments, the near-surface

temperature in PRD has raised by 0.9-1.1 K in MJJAS and 0.6-0.8 K in non-MJJAS season. Due to such anthropogenic warming, the intensity of extreme daily rainfall (> 95$^{th}$ percentile) increased by 8-9.5% (~CC rate) in MJJAS and 12.4% at most (~2×CC rate) in non-MJJAS season; their probability of occurrence increased by 10-30% in MJJAS and 20-40% in non-MJJAS. Moisture-related thermodynamic effects on rainfall change in the two seasons are similar, while dynamic effects on rainfall differ according to the season. Changes in MJJAS rainfall are related to stronger low-level southerly winds and the dominance of stronger ascents and descents. Larger increments in non-MJJAS rainfall are attributable to the strengthened low-level wind convergence and updraft. Moisture budget analysis suggests that thermodynamic effects account for the mean rainfall increase, whereas dynamic effects are responsible for rainfall extremes as inferred from WRF simulations.

Next, the seasonal dependence of extreme rainfall responses to human influence was examined by studying two remarkable extreme events from different seasons. To understand the involved mechanisms, we carried out an additional "counterfactual" run to isolate the human-caused thermodynamic effect. The human-induced dynamic effect can be inferred from the difference between the two "counterfactual" runs. In the record-breaking winter event attribution, human activities have caused the 4-day mean rainfall to increase at the CC rate and the 95$^{th}$ and 99$^{th}$ percentile extreme rainfall to increase at the double of CC rate. It is noteworthy that human-caused dynamic effects can further exacerbate the thermodynamic-driven rainfall increase. This is likely the results of robust land-sea thermal contrast, favoring anomalous southerly winds and strong wind convergence under human-related climate warming, highlighting the dominant role of dynamic effects on extreme rainfall intensification in this event.

We have also conducted attribution experiments for a pre-monsoon heavy rainfall event in May. This is motivated by the fact that PRD heavy rainfall in May is projected to decrease due to human influence based on global climate models. Large ensemble approaches were adopted to

ensure the model's fidelity in simulating this event. Human-induced thermodynamic anomalies have led to over 70% reduction in this pre-monsoon rainfall over eastern PRD and 25%-40% increases in the west for ~0.9 K warming; it also decreases rainfall probability by 20% per degree warming. This is due to decreased relative humidity and higher convection inhabitation energy by human-caused warming. These reductions, however, are mitigated by human-related dynamic effects associated with anomalous southerly winds.

Overall, we applied a new method to generate "counterfactual" conditions in regional models. Results of multi-case attribution highlight the human-induced greater enhancement in non-MJJAS rains compared to that in MJJAS season. All the findings point to the importance of dynamic effects on PRD rainfall extremes. More research into the role of weather type and background circulation played in rainfall responses to human forcing is warranted.

# 摘要

在人為強迫全球增暖的背景下，珠三角地區頻繁遭受強降水，從而對環境和社會造成了嚴重破壞。根據克勞修斯-克拉珀龍(CC)關係，大氣每升溫 1 K，空氣中水汽含量增加約 7%，從而加劇極端降雨。另外，人為變暖通過改變大氣環流強度可能會進一步影響極端降水。本研究使用 2 km 雲解析天氣預報模式 WRF 並基於偽全球變暖法 (PGW)，歸因分析了不同季節珠三角強降水事件對人為強迫的響應。

首先，我們對 40 例發生於 1998 至 2018 年間的珠三角極端降水事件進行歸因分析，其中 23 例發生在 5 至 9 月 (即 MJJAS) 以及 17 例發生在其餘月份 (非 MJJAS)。我們在事實和“反事實”條件下驅動模式。首先得到人為強迫信號，即 CMIP5 多模式中歷史和自然強迫實驗之差，再將該人為強迫從事實條件中剔除，從而得到上述條件(相當於反 PGW 法)。對比這兩組平行實驗可知，由於人為影響，珠三角近地表溫度在 MJJAS 升高了 0.9-1.1K，在非 MJJAS 升高 0.6-0.8K。因此，MJJAS 極端降雨量 (> 95$^{th}$ 百分位數) 增多 8-9.5％ (約 CC 增率)，而非 MJJAS 降水可增至 12.4％ (約兩倍 CC 增率); 降水發生頻率在 MJJAS 增加 10-30%，在非 MJJAS 增加 20-40%。水汽驅動的熱動力過程對兩季節降雨強度的影響類似；而動力過程對降水影響隨季節變化。MJJAS 降水變化與強低層偏南風以及強上升和下沉氣流有關，而非 MJJAS 降水增加的幅度更大是由於低層風輻合增強以及上升氣流更頻繁。水分收支分析表明，人為引起的熱動力變化對平均日降水增加的貢獻最大，而動力變化對極端降水的貢獻最大。

接著，我們通過兩個發生在不同季節的極端降水事件探究了人為影響極端降雨的季節性差異。為深入理解其物理機制，我們實施了另外的“反事實”實驗來分離僅人為引起的熱動力影響。兩次擾動實驗之差則表示人為引起的動力影響。通過對一次罕見的

冬季暴雨進行歸因分析，我們發現人為影響導致 4 日平均降雨量以 CC 速率增加，而極端降水則以約兩倍的 CC 速率增加。人為影響的動力過程可加劇由熱動力過程驅動的極端降水增強。這可能是由於強烈的海陸熱力差促使了異常南風及更強勁的低層輻合。這些發現突出了該事件中動力影響對極端降雨變化的主導作用。

我們還對一次季風前 (5 月) 強降雨事件進行歸因實驗。該部分研究是基於一個發現：全球模式結果表明人為影響導致珠三角 5 月極端降雨減少。歸因實驗採用大型集成方法來確保模式重現此事件的真實度。結果表明，在 0.9K 低層大氣增暖背景下，人為引起的熱動力異常使珠三角東部降雨量減少 70%以上，而西部降雨增加 25%-40%；該異常也導致降雨頻率降低 20% $K^{-1}$。這是由於對流層變暖，致使相對濕度降低，因此對流抑制能量增多。而人為引起的動力異常則緩解了此次降雨減少。

綜上所述，我們提出一個在區域模式中構建“反事實”條件的新方法。多個例歸因結果表明，人為影響使得非 MJJAS 季節降水比 MJJAS 增強更顯著。本研究發現還強調了人為引起的動力強迫對極端降水的影響更重要。此外，對天氣類型和背景環流在降雨對人為強迫響應中的作用仍有待研究。

# Acknowledgments

I would like to express my deepest gratitude to my supervisor Prof. Tam Chi Yung Francis, for his guidance throughout my doctoral research at CUHK. Three years ago, he took me to the emerging field of attribution science and generously shared his invaluable expertise and insights on this field, which helped me develop this research more effectively. I indeed benefit a lot from his constructive suggestions on my research and academic writing skills during every discussion. His rigorous and meticulous attitude towards research has strongly influenced my scientific thinking. The completion of this thesis could not have been possible without his assistance and support. I especially appreciate his patience with my sometimes slow progress and kind understanding of my arbitrary decisions, as well as his efforts to make this thesis readable. I am also grateful to Francis for granting me all the resources and opportunities to communicate with experts in this field, and I feel fortunate to be a member of our atmospheric dynamics group.

My sincere appreciation also goes to the committee members: Prof. Tai Pui Kuen Amos, Prof. Gan Thian Yew, and Prof. Liu Lin for their guidance and time dedicated to reviewing my dissertation. I particularly thank Prof. Chan Man Nin, who serves as my qualifying examiner, for his constant encouragement when I got down in the dumps and for his practical advice and useful comments to my research proposal.

I am thankful to my group members and lab mates, from whom I learned a lot and received timely help when I met tough problems. My greatest thanks go to Dr. Chen Jilong, who taught me patiently on technical issues I've encountered, and more importantly, he is willing to share his knowledge and modeling experiences with me, especially when I am a novice at this project. Also, I appreciate all the faculty and staff of the Department of Earth and Atmospheric Sciences

for organizing regular tea gathering for us to unwind after a busy week of studying. Thanks as well to my special friends in CUHK: Miss Hu Yan (my roommate) and Miss Xu Rongshuang for all the memories we had in Hong Kong and Japan that I will remember forever.

Finally, I would like to say thank you to my parents and lasting friends, who have always been my rock and give me unwavering support and encouragement throughout my journey. This thesis is dedicated to my dearest parents, Guiying Dang and Jianming Zhao.

# Table of Contents

# Abbreviations

| | |
|---|---|
| **CMIP5** | Coupled Model Intercomparison Project Phase 5 |
| **CTL** | Control experiments includes all forcing |
| **DTQ** | Experiments without human forcing on temperature and specific humidity |
| **DTQW** | Experiments without human forcing on temperature, specific humidity, and horizontal wind circulations |
| **ERA** | European Centre for Medium-Range Weather Forecasts re-analysis |
| **FAR** | Fraction of attributable risk |
| **GCMs** | Global climate models |
| **IBCs** | Initial and boundary conditions |
| **IPCC AR6** | Intergovernmental Panel on Climate Change - Assessment Report 6 |
| **MJJAS** | May-Jun-July-August-September |
| **NAT** | Experiments with natural forcing only |
| **Non-MJJAS** | The calendar months except May-to-September |
| **PGW** | Pseudo global warming |
| **PR** | Probability ratio |
| **PRD** | Pearl River Delta |
| **RCMs** | Regional climate models |
| **R95p (R99p)** | Precipitation from days in the top 95% (99%) |
| **Rx1day (Rx5day)** | Maximum precipitation amount in a day/ 5 days |
| **SC** | South China |
| **TRMM** | Tropical Rainfall Measuring Mission |
| **WRF** | Weather Research and Forecasting model |

# Chapter 1 Introduction

The hydrological cycle is strongly affected by climate change. Under the current warming climate, most regions of the globe have suffered robust fluctuations in rainfall, such as floods and droughts that have devastating consequences for the environment, the economy, and society. Regarding hydrological changes over the globe, scientists have raised these general but important questions: 1) what are the past and future changes in precipitation characteristics at various temporal and geographical scales? 2) To what extent can these changes be related or attributed to climate change primarily due to human activities? 3) What is the role of natural climate variability in observed extreme events? This chapter first introduces the research background on precipitation variations and their responses to climate change, followed by a literature review on a very challenging topic: attributing hydrological extremes to human influence. The motivation, objectives, and roadmap of this thesis are finally presented.

## 1.1 Research background

### 1.1.1 Changes in precipitation characteristics

Precipitation is a fundamental component of the hydrological cycle in the climate system. It is mainly characterized by the total amount accumulated over some averaging periods, frequency (i.e., numbers of rainy days), intensity (i.e., mean rainfall per day or hour), rain types (i.e., convective or stratiform), and duration of events (Dai, 2001b, 2001a; Dai, 2006). Precipitation variations have a variety of time scales, from hours to decades, leading to diverse consequences on the environment and society. For instance, steady moderate precipitation soaks the soil and benefits plants (Trenberth, 2011), while heavy rainfall with short durations can cause severe flooding disasters that lead to enormous economic and even human losses (Duan et al., 2016;

Willner et al., 2018). Numerous studies have been devoted to revealing and understanding the historical variations of precipitation and to predicting their variabilities in the future climate.

Long-term trends and changes in the rainfall amount (e.g., monthly, seasonal, annual, and decadal mean) have been analyzed based on in-situ observations over various regions (Hulme, 1992; Shahid, 2011; Groisman et al., 2012; Spracklen & Garcia-Carreras, 2015; Huang et al., 2017; Nicholson et al., 2018; Hoffmann & Spekat, 2021). Many of these regions have experienced increasing precipitation trends over the past century, while drying trends of annual rainfall are also seen, e.g., the Mediterranean (Longobardi & Villani, 2010; Mariotti et al., 2015), North America and Australia (Cook et al., 2018), and Western Africa (Dunn et al., 2020), as well as North China (the latter due to the weakened East Asian monsoon) (see Wang & Ding, 2006; Ding et al., 2008; Zhou et al., 2008; Zhang et al., 2011). The amount change varies not only with regions but also with rainfall categories. For instance, tropical rainfall change shows a decreasing trend of 2.6% per decade for light rainfall but an increasing trend of 1.8% per decade for intense rainfall from 1988 to 2008 (Allan et al., 2010). Further studies demonstrate that the former contributes more to changes in the total rainfall amount (Dai, 2001b; Liu et al., 2005; Trenberth & Zhang, 2018).

Various observational records also show remarkable agreement in changes in extreme rainfall, compared with mean and moderate rains (Karl & Knight, 1998; Groisman & Knight, 2008; Fischer & Knutti, 2016; Huang et al., 2017). They also show an exacerbation of heavy rainfall events in many locations of the globe (Alexander et al., 2006; Min et al., 2011), and with decreased durations (Dwyer & O'Gorman, 2017). Several indices are adopted to quantify precipitation extremes (see Table 1 in Dunn et al. (2020)). The most commonly used indices are the maximum precipitation amount in a day (Rx1day) or in 5 days (Rx5day) and the precipitation from days in the top 95% or 99% (R95p, R99p). On the global scale, the decadal trend and probability of Rx1day were firstly assessed by Easterling et al. (2000). The frequency

of heavy precipitation events (R95p) indicates an increasing probability for many extratropical regions (Groisman et al., 2005). A similar change is also seen in the tropics (Lau & Wu, 2007, 2011). Lately, it was found that Rx1day increased dramatically over the global land since the 1950s (Dunn et al., 2020; Sun et al., 2021); Rx5day has similar long-term trends as Rx1day from a global perspective (Zhang & Zhou, 2019), with a higher increase in Rx5day (4.7%) than in Rx1day (4.0%) over Northern Hemisphere land (Zhang et al., 2013).

On the regional scale, changes in extreme daily rainfall show spatial diversity. Compelling evidence of extreme precipitation intensification has been found in most continental areas, regardless of observational datasets and data processing methods utilized. For example, both Rx1day and Rx5day increased in North America and Europe from 1950 to 2018 (Sun et al., 2021) and in some South Asia areas for 1961-2000 (Sheikh et al., 2015); R99p increased by 0.3 mm per year in Northeast America during 1979-2014 (Howarth et al., 2019), and R95p enhanced from 1972 to 2010 over South Asian monsoon areas (Cheong et al., 2018; Kim et al., 2019). Particularly in China, the accumulated amount of area-averaged heavy daily rainfall has increased by ~2% per decade for 1960-2013 (Ma et al., 2015); the maximum hourly summer rainfall intensity enhanced by ~11% within the 1971-2013 period (Xiao et al., 2016). In contrast, heavy rainfall in Australia tends to increase in the north but decrease in the eastern parts of the continent (Dey et al., 2019; Sun et al., 2021). There exists a significant decline in daily rainfall extremes in the Eastern Mediterranean (Mathbout et al., 2018), as well as an increase in hydrological droughts in California (Diffenbaugh et al., 2015) and the Mediterranean (Gudmundsson & Seneviratne, 2016), probably due to anthropogenic climate change. In East Asia, no systematic trend of extreme rainfall frequency was found (Choi et al., 2009). Moreover, changes in different rain types may differ. Haerter & Berg (2009) suggested that more convective precipitation occurred with shorter durations. The duration of extreme events was also found to decrease as temperature rises (Haerter et al., 2010; Hardwick Jones et al., 2010).

With the knowledge of historical precipitation behaviors, numerous efforts have been devoted to evaluating the performance of current weather and climate models against a variety of observational data and, more importantly, to predicting future changes of precipitation. Model projections suggest that precipitation becomes more unevenly distributed in a future warmer climate. Konapala et al. (2020) examined precipitation changes over global land under three future scenarios of representative concentration pathways (RCP2.6, 4.5, and 8.5) in global climate models (GCMs) participating in the Fifth Phase of Coupled Model Intercomparison Project (CMIP5), suggesting that the annual mean increases across all land, with largest increments in RCP 8.5, under which it reaches 12%±8% in China by the end of 21$^{st}$ century (Tian et al., 2015). The seasonal mean change presents a wet-gets-wetter pattern as previously reported by Chou et al. (2009, 2013) and Greve et al. (2014). However, in southwest Australia, the mean rainfall will continue to decrease based on CMIP5 models (Dey et al., 2019). Similarly, CMIP6 models suggest that annual mean rainfall in Central Asia significantly increases under all Shared Socioeconomic Pathways and the Representative Concentration Pathways (SSP1-2.6, SSP2-4.5, SSP3-7.0, and SSP5-8.5), with the largest rise of 14.4% relative to present-day found in SSP5-8.5 (Jiang et al., 2020). Consistent with observations, models also show a notable enhancement in extreme precipitation from hourly to daily scales over both wet and dry regions (Emori & Brown, 2005; Alexander et al., 2006; Kharin et al., 2013; Donat et al., 2016; Xiao et al., 2016; Prein et al., 2017; Dai et al., 2020).

### 1.1.2 Anthropogenic forcing on precipitation extremes

The above summarizes studies providing compelling evidence of mean and extreme rainfall increase across most continents under a changing climate. It is striking that there are higher increases in the extremes compared to the mean values. In fact, mean rainfall is strongly constrained by atmospheric energy balance, while extreme rainfall scales mostly with

temperature (Allen & Ingram, 2002; Held & Soden, 2006; Trenberth & Zhang, 2018). According to the latest sixth Assessment Report (AR6) of Intergovernmental Panel on Climate Change (IPCC), the observed global mean surface temperature has risen by 0.9℃-1.2℃ from 1850-1900 to 2010-2019, with 0.8℃-1.3℃ attributable to human forcing and only ±0.1℃ owing to natural forcing (IPCC, 2021). In the future, the global mean rainfall is projected to increase by 3-4% $K^{-1}$ (4-5% $K^{-1}$ for global land and 2-4% $K^{-1}$ for ocean) by the end of the 21st century under the RCP8.5 scenario (Pendergrass et al., 2017), which probably resulted from the positive Earth's energy imbalance due to climate change (Raghuraman et al., 2021). Besides the mean, heavy precipitation in response to human influences, such as growing concentrations of greenhouse gas emissions, anthropogenic aerosol emissions, and urbanization effects, is of great concern.

So how does human-induced greenhouse warming modulate precipitation? As the temperature rises, the atmosphere can accommodate more water vapor, such that heavy rainfall is expected to increase for it strongly relies upon moisture availability (Trenberth et al., 2003; Held & Soden, 2006). The relationship between saturation vapor pressure ($e_s$) and temperature ($T$) is expressed by the Clausius-Clapeyron (CC) equation proposed in 1838 (see, e.g., Westra et al. (2014)):

$$\frac{de_s}{dT} = \frac{L_v(T)e_s}{T^2 R_v} \qquad (1.1)$$

where $R_v$ = 461.5 J $kg^{-1}$ $K^{-1}$ (gas constant of water vapor) and $L_v$ = 2.5× $10^6$ J $kg^{-1}$ (latent heat of evaporation of water at 0℃, a weak function of temperature).

Then linearizing Eq. (1.1) at $T$ = 273.15 K:

$$\frac{dlne_s}{dT} \cong 0.073(1 - 0.007T) \qquad (1.2)$$

The saturation specific humidity $q_s$ (the mass of water vapor) can be derived from:

$$q_s \cong \frac{0.622}{P} e_s \qquad (1.3)$$

where $P$ is the pressure ($10^5$ Pa at the surface). From Eq. (1.2) and Eq. (1.3), the saturation specific humidity would increase by 6% (7%) per degree increase in surface temperature at 24℃ (0℃). Assuming that relative humidity remains constant (Willett et al., 2007), the atmospheric moisture content will increase at the CC rate (6-7% $K^{-1}$). Thus, extreme rainfall is expected to enhance at the same rate as moisture does. Indeed, results from both observations and simulations have corroborated the homogeneous increase in water vapor content with warming at the CC scaling (Ross & Elliot, 2001; Trenberth et al., 2005; Santer et al., 2007). In contrast, precipitation increase differs from regions and intensities. Globally, a ~7% increase in heavy rainfall and ~1.8% increase in light rainfall were found for a 1% rise in $CO_2$ emissions per year (Lau et al., 2013). Observational evidence indicates that extreme precipitation in some areas increases at a super-CC rate, e.g., double of increments expected from the CC relation (Lenderink & Meijgaard, 2008; Lenderink et al., 2011, 2017; Fischer & Knutti, 2015; Myhre et al., 2019), implying a positive dynamic effect on heavy precipitation (Nie et al., 2018). The underlying mechanisms for such responses to anthropogenic warming will be demonstrated in section 1.2. In addition, there exist slight changes or decreases in intense rainfall with warming (Watterson, 2008), which might be related to relative humidity changes (Sherwood et al., 2010; Chen et al., 2020).

Human-caused precipitation changes are not only affected by greenhouse-gas emissions, but also by anthropogenic aerosols. The latter can lead to a cooling effect on the climate system, which partly offsets global warming caused by the former (Seong et al., 2021). In contrast to greenhouse warming, anthropogenic aerosols have a complicated effect on rainfall (Rosenfeld et al., 2008). First, aerosol loadings can affect precipitation via altering atmospheric radiative balance by absorbing or scattering short and long-wave radiations to cool the surface (Qian et al., 2007). Second, aerosol particles also serve as cloud condensation nuclei and can alter cloud

properties through the microphysical processes involved in the cloud system and ultimately modify precipitation ( Zhang et al., 2011; Fan et al., 2016).

In addition, with rapid urbanization (e.g., land use/land cover change) over the last few decades, a growing body of literature has explored its impacts on intense precipitation in urban areas. In particular, urban heat island meaning higher temperature in the urban compared to surrounding rural areas (Zhong et al., 2017) can enhance convective initiation and intensify urban rainfall over a downwind of cities at the daily or sub-daily scales (Chen et al., 2015; Wu et al., 2019). The relative contributions of these anthropogenic forcing to precipitation change have been studied (Lau et al., 2017; Ma et al., 2017; Zhong et al., 2017; Seong et al., 2021). It was found that greenhouse gas emissions are estimated to be the main driver of tropospheric warming and contribute most to precipitation change globally (IPCC, 2014). For some cases, anthropogenic aerosols counterbalance the increased risk of floods due to greenhouse warming (Kumari et al., 2019).

## 1.2 A review on attribution of precipitation extremes to human influences

As mentioned, global mean and extreme precipitation have increased dramatically since the second half of the twentieth century, in the context of climate warming induced by human activities. More notably, many regions have been suffering from hydrological extreme events more frequently, despite the mean rainfall being unchanged. The meteorological nature of these events and their impacts and the role of human activity in them are of growing concern of researchers and the general public. Allen (2003) proposed these scientific questions: Is it possible to attribute a specific extreme weather occurrence to climate change (mostly driven by human influence)? How much, if at all, has it influenced the extreme events? Addressing these questions feeds the growing demand to explain human impacts on extreme events and evaluate the contributions of various anthropogenic factors to the event. In late 2014, the World

Weather Attribution (www.worldweatherattribution.org) was launched to provide a real-time attribution assessment of extreme weather events worldwide, which promotes the development of the attribution science. This section reviews current studies on the science of "extreme event attribution" by responding to the above questions from the following aspects: 1) the approaches or procedures for performing an event attribution; 2) attribution results using different methods and some examples of recent event attribution, primarily for hydrological extremes, and 3) the involved potential mechanisms from large-scale and regional perspectives.

### 1.2.1 Methods for attribution analysis

A variety of approaches has been taken to event attribution study. Earth system models are an indispensable tool for attributing extreme events to anthropogenic influence. A typical way for quantitative attribution is to compare an event simulated under the climate with and without anthropogenic forcing (i.e., so-called factual versus counterfactual climates). The latter climate can be easily constructed by modifying initial conditions and forcing in models. Observation-based empirical methods are also used for attributing the events, especially those are not well reproduced by models (Stott et al., 2016). The advantages of employing climate models are that they incorporate the physics of the climate system and can have adequate samples by repeating simulations using different initial conditions or physics schemes, making them more suitable for attribution research. We first introduce the main metrics utilized to quantify the changes of extreme events that are attributable to human forcing, and then review the two most widely used model-based approaches in attribution research.

#### 1.2.1.1 Metrics for attribution assessment

Previous research assessed the potential risk of extreme event occurrences under anthropogenic influences by computing three metrics, including the fraction of attributable risk (FAR), probability ratio (PR, also called risk ratio), and return periods of events (Hannart et al., 2016).

The FAR was originally proposed for extreme precipitation attribution by Allen (2003) and theoretically documented in Stone & Allen (2005). They defined FAR=1-($P_0$/$P_1$) varying from 0 to 1, where $P_0$ and $P_1$ represent the occurrence probability of events exceeding a certain threshold under the counterfactual and factual climate, respectively. It should be noted that FAR describes the risk of a class of similar events rather than the risk of a specific event. For example, a FAR of 0.4 for a heavy rainfall event (R) indicates that two of five R-like events (e.g., they have similar synoptic backgrounds or intensities) in realism would not occur in the counterfactual climate. An alternative estimate is the PR ($P_1$/$P_0$), also known as ratio risks, which is applied to attribute rainfall extremes (Fischer & Knutti, 2015; Herring et al., 2018). The return period of events is used to depict how rarely the event occurs (Kumari et al., 2019). Several more recent studies on the attribution of hydrological extreme events using these estimates are listed in **Table 1.1**. Besides those probability metrics, anthropogenic influence on the intensity of extremes has been estimated by comparing long-term trends of precipitation indices, e.g., Rx1day and Rx5day, under different forcing climates (Paik et al., 2020). More detailed findings regarding these estimates are elaborated on in section 1.1.4.

***Table 1.1*** *Some examples of hydrological extreme events attributable to human influence.*

| Date of event | Location | Event type | Method | Source |
|---|---|---|---|---|
| July 2021 | Western Europe | Heavy rainfall | PR | (Kreienkamp et al., 2021) |
| Summer 2020 | Eastern China | Extreme Meiyu rainfall | PR | (Zhou et al., 2021) |
| April-May 2017 | Bangladesh | Pre-monsoon extreme rainfall | Return period/PR | (Rimi et al., 2019) |
| August 2017 | Texas US | Extreme rainfall (Harvey caused) | PR | (Risser & Wehner, 2017) |
| 2007-2017 | New Zealand | Floods & droughts | FAR | (Frame et al., 2020) |
| 2015-2017 | Western Cape | Droughts | PR | (Otto et al., 2018b) |

#### 1.2.1.2 GCM-based attribution

The GCM-based attribution is more suitable for large-scale extreme events due to the coarse resolution. The most commonly used GCMs are those taken from CMIP. In CMIP5, historical simulations were run mostly from 1850 to 2005 as the baseline. Meanwhile, several suites of perturbed experiments were designed for extreme event attribution, including the *historicalNat*, *historicalGHG*, and *historicalMisc* runs forced by natural agents (e.g., volcanic eruptions and solar radiation), greenhouse gas emissions, and various combinations of other forcing agents (e.g., anthropogenic aerosols), respectively (Taylor et al., 2012). For individual rainfall events occurring before 2005, their responses to anthropogenic forcing can be estimated from the difference between historical and perturbed trials. CMIP6 models are increasingly employed for the attribution of extreme events after 2005 (e.g., Zhou et al., 2021). The experiments in each model contain a large number of ensembles, with the ensemble mean and long-term mean typically utilized to reduce inter-model and interannual variabilities, respectively. Using the large ensemble of GCMs, the circulation analogs method was presented and applied to isolate the human-influenced circulation impacts on extreme precipitation (Vautard et al., 2016; Yiou et al., 2017). This approach and relevant examples were overviewed in detail by Stott et al. (2016).

#### 1.2.1.3 RCM-based attribution

Convection-permitting regional climate models (RCMs) with horizontal grid spacings of less than 5 km are typically employed for attribution of local-scale extreme events related to convection (Zhang et al., 2016; Minamiguchi et al., 2018; Dai et al., 2020), due to their better representation of these events. The pseudo global warming (PGW) method, firstly proposed by Schär et al. (1996) and refined by Kimura & Kitoh (2007), was applied to downscale GCM-derived anthropogenic climate (differences between historical and perturbed runs) in RCMs.

The main procedures of this approach are summarized as follows:

(1) Determine human influence upon relevant field $X$ – differences between $X$ in historical and perturbed trials in GCMs;

(2) Obtain counterfactual IBCs – interpolate the anomalous $X$ from (1) onto each grid of $X$ in the initial and boundary conditions (IBCs) in RCMs, and impose interpolation results onto the latter $X$ field;

(3) Dynamical downscaling in RCMs – reproduce extreme events under the original and future IBCs (additional human forcing) separately;

(4) Conduct attribution analysis by comparing the two sets of experiments in (3).

The main advantage of the PGW method is that it allows one to assess certain characteristics of an individual event which can be attributed to human forcing usually with the help of high-resolution regional models (Kimura & Kitoh, 2007). In addition, a "detrended" method for generating a counterfactual climate in RCMs was introduced and applied for the attribution of hurricane Harvey's extreme precipitation (Wang et al., 2018), in which the long-term historical trends of reanalysis were removed from IBCs in RCMs. For the same purpose, this thesis presents a "reversed PGW approach" and has applied it to the PRD extreme rainfall attribution (see details in Chapter 2.4.3). The disadvantage of PGW – or many events based on attribution methods – is the impacts of climate change on the frequency and occurrence of certain types of events cannot be assessed.

### 1.2.2 Results for extreme rainfall attribution

#### 1.2.2.1 Intensity variations

Attribution studies have provided strong evidence of human influence on extreme precipitation intensity at global and regional scales. Observational and CMIP6 results consistently show the

overall increasing trends of R95p and R99p from 1951 to 2014, relative to the 1961-90 mean baseline, due to anthropogenic forcing, from global to continent scales (see **Figure 1.1**). The global mean Rx1day and Rx5day are observed to increase by 6.6% and 5.7% per 1 K increase in global mean surface temperature during 1950-2018, respectively (Sun et al., 2021). In the entire tropics, changes in magnitudes of extreme rainfall (R99p) reach as high as 4% on average for 1 K global warming, which is nearly the CC scaling (Chou et al., 2012). On a regional basis, Kirchmeier-Young & Zhang (2020) computed the observed and simulated changes in Rx1day and Rx5day using various models and approaches. The results consistently display positive trends for both indices, suggesting that human activities intensified extreme rainfall in North America from 1961 to 2010. A new attribution study on European rainfall extremes pointed to a latitudinal increase of rainfall intensity due to anthropogenic influence, with the increment of 8%, 26%, and up to 41% at low, mid, and high latitudes, respectively (Tabari et al., 2020). Over China, CMIP5 results suggest that anthropogenic forcing has intensified the Rx1day and Rx5day close to the nearly CC scaling (Li et al., 2017). However, it was not detected using different models and attribution procedures (W. Li et al., 2018). This may imply that anthropogenic forcing is not robust and more research on the attribution of extreme rainfall at the regional scale is worth undertaking. Besides using GCMs, results from a high-resolution regional model demonstrate that anthropogenic warming could have increased Hurricane Harvey's extreme precipitation in Texas by 20% (Wang et al., 2018), with comparable changes found using different models (Oldenborgh et al., 2018).

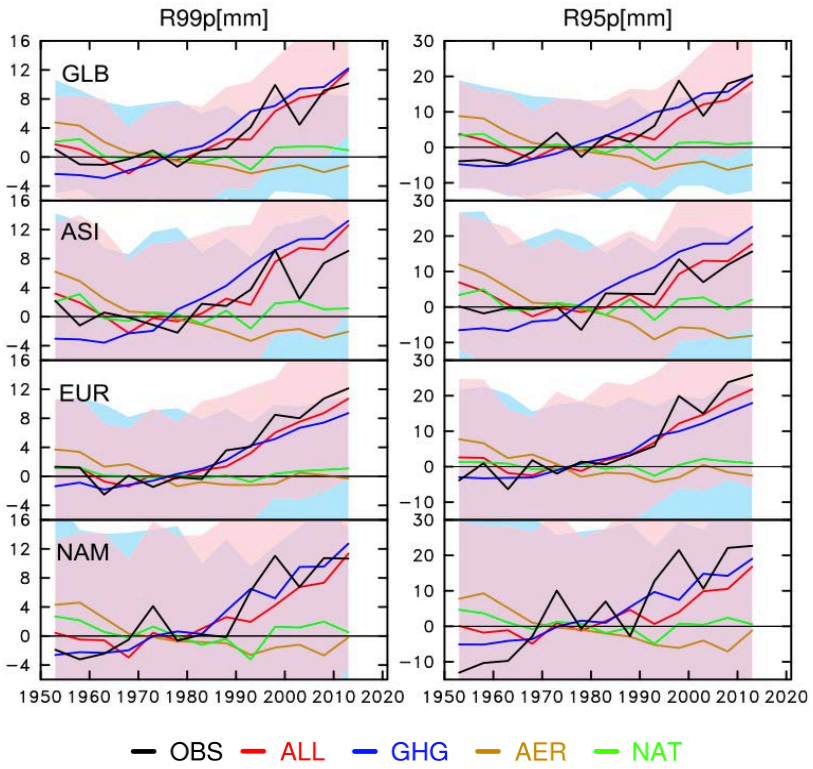


***Figure 1.1*** *Time evolution of extreme rainfall for R99p (left column) and R95p (right column) from 1950 to 2014, relative to the 1961-1990 mean baseline, averaged over the global (GLB), Asia (ASI), Europe (EUR), and North America (NAM). Rainfall series are derived from the observations (OBS, black lines) and CMIP6 simulations with all forcing (ALL, red lines), greenhouse-gas forcing (GHG, blue lines), aerosol forcing (AER, brown lines), and natural forcing (NAT, green lines). From Dong et al. (2021).*

### 1.2.2.2 Probability variations

Precipitation extremes attribution to human influence based on three probability estimates mentioned above have been introduced. Globally, human influence contributed a 40% increase in the probability of extreme precipitation for a 2℃ warming, with most pronounced increases in the tropics and decreases in subsidence regions; this change becomes more remarkable in higher warming scenarios (see **Figure 1.2**). On a regional scale, summer heavy rainfall (> 95$^{th}$ percentile) events in Europe became more frequent under greenhouse-gas warming, despite its summer getting drier (Christensen & Christensen, 2003). Pall et al. (2011) used FAR estimate

to attribute the exceptional year 2000 flood in England and Wales and concluded that anthropogenic greenhouse gas emissions enhanced the risk of such floods by about 20%. The return period of intense rainfall in India in June 2013 also shows a positive contribution from human forcing, but the precise quantification is equivocal due to the coarse resolution and limited ensemble size of models (Singh et al., 2014). For extreme rainfall in May 2015 in China, the FAR estimate suggests that anthropogenic forcing has increased the probability of such or more intense rainfall by at least ~23% in South China (Burke et al., 2016). For another exceptional heavy rainfall event in the Yangtze River basin of China in May 2016, anthropogenic climate change increased the risk of likelihood (PR) in the northern part by 1.64 (~40% in FAR), and a reduction in the southern part (Li et al., 2018); similar increase (~38%) is estimated for the 2016 summer mean (Yuan et al., 2018). Otto et al. (2018a) attributed storm-related severe rainfall in England to anthropogenic climate change using observation- and model-based methods. The results illustrate that anthropogenic influences have increased the probability of such events by ~59%, but with large uncertainties.

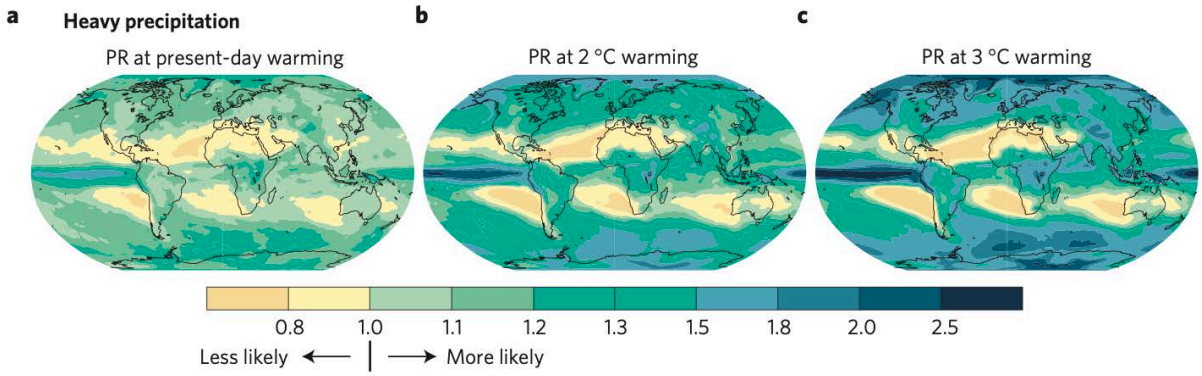


***Figure 1.2*** *Changes in the probability of precipitation extremes exceeding the 99$^{th}$ percentile of daily precipitation for the global-mean warming of (a) 0.85*℃ *(present-day), (b) 2*℃*, and (c) 3*℃ *relative to pre-industrial conditions. From Fischer & Knutti (2015).*

### 1.2.2.3 Seasonal-dependent variations

The seasonality of extreme precipitation influenced by global warming has also been argued in previous studies (Westra et al., 2014; Song et al., 2018; Trenberth & Zhang, 2018). Over the northern tropical land area, the 1979-2019 trend of annual precipitation displayed an obvious seasonal cycle based on observations and simulations. Notably, anthropogenic forcing results in a ~4-day delay of such seasonal cycle (Song et al., 2021). For European daily rainfall extremes, they were observed to increase in winter but decrease in summer when temperature rises (Berg et al., 2009). The response of extreme precipitation in California to global warming also shows a distinct seasonal variation, with more intense and frequent extremes in winter than in spring and fall based on CMIP5 models (Dong et al., 2019). In contrast, for the contiguous United States as a whole, more frequent but less intense wintertime rainstorms under warming were seen in regional model simulations (Dai et al., 2020). In China, the frequency of extreme rainfall shows a positive trend mainly in winter across southern areas, while opposite trends in summer and winter in northern regions are found (Tao et al., 2018).

### 1.2.3 Possible mechanisms

#### 1.2.3.1 Impacts of large-scale circulations

Human-induced global warming affects the behavior of large-scale circulations, which regulate regional moisture transport that feeds heavy precipitation (Liu et al., 2020). Numerous studies found that anthropogenic forcing has an influence on the East Asian Monsoon changes (Burke & Stott, 2017; Zhang & Zhou, 2019), resulting in an increase in precipitation in southern China while a decrease in northern parts (Day et al., 2018), which implies the possible response of monsoon circulation (Song et al., 2014). The western Pacific subtropical high (WPSH) and subtropical westerly jets (SWJ) – components of the East Asian summer monsoon (EASM) – are the main drivers of moisture transport and summer rainfall over eastern China (Wang & Zuo, 2016; Zhang et al., 2017). Under global warming, the WPSH and SWJ shift southward

probably due to the weaker meridional temperature contrast produced by the higher warming in mid-high latitudes than low-latitudes and thus decreased pressure gradient in mid-high latitudes (Li et al., 2010). The southward displacement of WPSH favors strong moisture transport and thus enhances summer rainfall in the Yangtze River valley (Xuan et al., 2011). Recent modeling studies have concluded that in boreal summer, anthropogenic greenhouse-gas emissions lead to an El Niño-like sea surface temperature pattern related to a weakened Walker circulation (Kociuba & Power, 2015), which suppresses convection over SC and thus reduces precipitation there (Lin et al., 2020). Attributions of extreme events conditioning on a particular feature of climate have also been explored. For example, inferred anthropogenic influence on the likelihood of heavy Australia precipitation during 2010-2012 when strong La Niña conditions prevailed was model-dependent and not robust, highlighting the role of internal variability of the climate system (Lewis & Karoly, 2015).

#### 1.2.3.2 Thermodynamic versus dynamic effects

Anthropogenic influences intensify precipitation extremes due to both thermodynamic and dynamic processes. Moisture budget analysis is a very useful tool for quantifying the contributions of these processes to precipitation and has been widely used for heavy rainfall at various scales. Modeling results agree that the thermodynamic component – changes in atmospheric water vapor – has homogeneous positive and dominant contributions to heavy rainfall intensification globally, whereas the dynamic component – wind circulation change – has little or negative contribution at a global scale but modulates regional rainfall extremes (Seager et al., 2010; Chou et al., 2012; Pfahl et al., 2017; Norris et al., 2019). On the regional scale, the thermodynamic effect is the main contributor to sub-seasonal rainfall increases in North America, while dynamic processes dominate rainfall decreases in Mexico due to global warming (Dong et al., 2018). In contrast, positive dynamic contributions amplify the extreme

rainfall intensification in the Asian Monsoon region (Pfahl et al., 2017; Ali & Mishra, 2018) and the deep tropics (Norris et al., 2019).

Besides, statistical methods can also be used to separate the dynamic (related to vertical motion) and thermodynamic contributions to precipitation changes (Emori & Brown, 2005; O'Gorman & Schneider, 2009; Chou et al., 2012; Pfahl et al., 2017; Ali & Mishra, 2018). Similar conclusions are drawn for global rainfall extremes. Contributions to regional extremes, on the other hand, differ according to the event. For example, the dynamic contribution (9% $K^{-1}$) to sub-daily extreme rainfall increases in India is higher than the thermodynamic contribution (6% $K^{-1}$) (Ali & Mishra, 2018). In addition, the human influencing thermal gradients could also modify the frontal circulation that closely affects precipitation changes (Kim & Kim, 2020).

Recall that super-CC scaling of rainfall extremes is found for their past and future changes, highlighting the dynamic effect beyond the moisture-driven thermodynamic influence. To better understand such dynamics, the quasi-geostrophic omega equation has been utilized to examine vertical motion changes and their effects on extreme rainfall (O'Gorman, 2015; Nie et al., 2016, 2018; Li & O'Gorman, 2020). The findings show that as moisture amount increases under global warming, heavy rainfall increases and releases more latent heat, which enhances updraft motions and ultimately intensifies heavy precipitation at a super-CC rate. Another research, using circulation analogs methods to separate thermodynamic and dynamic influence on winter rainfall extremes in Southern UK, found that the former effect contributes two-thirds of the rainfall increase whereas the latter, which is related to circulation changes, contributes about one-third of the increase (Vautard et al., 2016).

## 1.3 Motivation and objectives

Human-induced global warming has substantially affected extreme precipitation worldwide in many aspects, and some of these extremes have caused flooding disasters, as introduced above.

Particularly in China, both hourly and daily precipitation extremes increased at the super-CC rate with global warming during 1970-2017 across eastern China based on high-quality gauge data (Chen et al., 2021). Robust increases in extreme rainfall or flooding events are also seen in southern areas (Zhai et al., 2005; Ding et al., 2007).

The Pearl River Delta (PRD) region (defined as 21.5°N-24°N, 111.9°E-115.1°E), one of the largest megalopolises in China with a dense population and fast-growing economy, is vulnerable to hydrological extremes. Under a human-influenced warming climate, the PRD has been experiencing dramatic increases in the probability, intensity, and tendency of heavy rainfall during the last several decades according to historical records (Lenderink et al., 2011; Fu et al., 2013; Sun & Ao, 2013). The greatest concern from the public and policymakers is that how much of the PRD rainfall fluctuations resulted from human influence. Past studies have tried to address this issue with the use of GCMs outputs (Burke et al., 2016; Li et al., 2018).

However, as previously reported, the current global models usually have large biases when compared to observations. One bias is that most CMIP5 GCMs tend to produce precipitation more frequently but with lower intensity (Dai & Trenberth, 2004; Stephens et al., 2010; Asadieh & Krakauer, 2015; Donat et al., 2016; Trenberth et al., 2017); this is likely associated with the more convective precipitation in models (Sabeerali et al., 2015). Also, global models underestimate the observed trends of heavy precipitation (Min et al., 2011; Asadieh & Krakauer, 2015; Borodina et al., 2017). These biases probably resulted from a wide range of uncertainties in simulating atmospheric circulations due to their coarse resolutions (Shepherd, 2014; Trenberth et al., 2015; Li et al., 2019). In contrast, RCMs with high spatial, convection-permitting resolution can improve the representation of the observed rainfall extremes (Park et al., 2016). To our knowledge, so far there is no attribution study for PRD extreme rainfall using

RCMs. Therefore, a convection-permitting Weather Research and Forecast (WRF) regional model is utilized to fill this research gap.

This thesis aims to achieve the following objectives from the perspective of multi-case statistics and individual case studies:

- To examine the change of PRD precipitation extremes in the presence of human influence**,** for different seasons;
- To investigate the extent to which extreme precipitation variations can be attributed to human forcing; and
- To better understand the underlying mechanisms for human-forced precipitation changes, including both dynamic and thermodynamic influences.

Yet there are many challenges in conducting event attribution analysis for extreme rainfall. For example, model biases in reproducing extreme rainfall (e.g., location, intensity) may affect the reliability of results. To minimize the model bias, a spectral nudging technique and large ensemble approaches are considered in model simulations. There are also technical challenges when creating a "counterfactual climate" in WRF, such as interpolation bias and imbalance of the artificial climate during integrations. Fortunately, many of these difficulties have been resolved, and more details will be presented in the methodology section. Overall, the findings in this thesis complement the attribution map and more importantly, will help us better understand the role of human influence in affecting rainfall extremes in this region.

## 1.4 Roadmap of thesis

In this thesis, impacts of human-induced climatic warming on a series of extreme precipitation events over the PRD region have been analyzed using the regional WRF model. Chapter 2 introduces all data sets, model setting, experiment design, and various methodologies used. In particular, an attribution method of constructing a counterfactual climate in WRF (equivalent

to a reversal of the PGW downscaling technique) is described in Chapter 2.4.3, and its performance has been verified in Chapter 4. Attribution results are presented in Chapters 3, 4, and 5, whereas Chapter 6 encompasses discussions and main conclusions.

In Chapter 3, how PRD extreme precipitation responses to human influence depends on seasons is explored, based on multi-case simulations. In total, forty extreme rainfall cases (23 in MJJAS and 17 in non-MJJAS) are selected, and then reproduced under the present and counterfactual (without human forcing) conditions in the model. Human-contributed warming signals in PRD are first estimated by comparing parallel experiments. Responses of those extremes to this warming are then examined in terms of their intensities and frequencies. Also, the seasonal difference in rainfall responses is analyzed. To further inspect the possible reason, the moisture budget equation is used to estimate the thermodynamic and dynamic contributions to the changes in rainfall extremes.

Chapter 4 focuses on an extraordinary wintertime extreme precipitation event. Attributing this event to human influences is examined by conducting the same experiments as in Chapter 3. To separate human-related thermodynamic and dynamic impacts, an extra experiment (without human-forced thermodynamic influence) is carried out. Human impacts on this heavy rainfall intensity, and associated changes in large-scale atmospheric circulations, contributions from the moisture-driven thermodynamic process as well as vertical motion-related dynamic process are well elucidated.

Similar to Chapter 4, the attribution of a pre-monsoon heavy rainfall event is conducted in Chapter 5 but draws an opposite conclusion. A plausible mechanism for human impacts on this particular event is addressed. Results from these two case studies suggest that human-induced warming climate could either intensify or suppress heavy rainfall in specific events over this region, which also depend on synoptic conditions.

# Chapter 2 Data, model and methodology

## 2.1 Outline of methods

To quantify the seasonally dependent changes in extreme precipitation characteristics due to human influences, a series of extreme rainfall events from different seasons were selected and replicated using a numerical model forced by different initial and boundary conditions, with model results being further analyzed. Since the contribution of TC-induced rainfall to PRD's annual rainfall is only about 20-35% (Khouakhi et al., 2017), this research focuses on non-TC-induced extreme precipitation in PRD, as well as the associated thermodynamic and dynamic changes due to human-induced climatic warming, on both a statistical and case-by-case basis.

In the first part of this thesis, over 200 historical extreme rainfall events that occurred over the PRD region during the 1998-2018 period were initially identified (see Chapter 2.4.1), based on the Tropical Rainfall Measuring Mission (TRMM) 3B42 satellite observations (see Chapter 2.2.1). These cases were reproduced with the use of the Weather Research and Forecasting (WRF) regional model (see Chapter 2.3.1). Simulated rainfall was compared to in-situ observations (see Chapter 2.2.1), based on which 40 well-simulated extreme events were further selected for attribution analysis.

The attribution of those extremes to human-induced warming can be done by re-simulating the selected 40 cases in WRF under an environment without human influences (see Chapter 2.3.2), through the pseudo global warming (PGW) downscaling technique (see Chapter 2.4.3). Human impacts on atmospheric circulations were derived from seven selected general circulation models (GCMs) participating in the Coupled Model Intercomparison Project Phase 5 (CMIP5, see Chapter 2.4.2). A combination of measurements was used to evaluate the capacity of GCMs in simulating surface temperature (see Chapter 2.2.2). By comparing the outcomes of the two

sets of experiments described above, human impacts on extreme precipitation in rainy and non-rainy seasons can be determined. To further explore how human activities affect rainfall extremes by altering the associated thermodynamic and dynamic processes, two individual heavy rainfall events (see Chapters 4 and 5) were focused on, with additional experiments carried out using WRF (see Chapter 2.3.2). Moreover, moisture budget analysis was utilized to address the thermodynamic and dynamic variations as a result of anthropogenic climate change (see Chapter 2.4.4).

## 2.2 Observational and reanalysis data

### 2.2.1 Rainfall datasets

*TRMM 3B42 product*

The Tropical Rainfall Measuring Mission (TRMM) is a research satellite operation from 1997 to 2015, which was jointly overseen by the National Aeronautics and Space Administration (NASA) and Japan Aerospace Exploration Agency (JAXA). It aims at monitoring the spatial-temporal distribution and variability of tropical precipitation. The 3B42 precipitation estimate is one of the TRMM products that combine various measurements of satellites and rain gauges. The TRMM 3B42 version 7 product (Huffman et al., 2007), available at a $0.25° \times 0.25°$ horizontal resolution (approximately 25 by 25 km) from 50°N to 50°S and 3-hourly temporal resolution for the 1998-2018 (https://disc.gsfc.nasa.gov/datasets/TRMM_3B42_7/summary), is used here and 3-hourly data are accumulated to obtain daily mean precipitation in this study.

*Rain gauge-based datasets*

In addition, two rain gauge-based data sets of daily precipitation were used for evaluating the WRF-simulated rainfall. The first in-situ dataset is developed by the National Meteorological Information Center of the Chinese Meteorological Administration (CMA, http://data.cma.cn),

with the locations of 29 weather stations considered within the PRD region depicted in **Figure 2.2**. Grided daily analysis of precipitation from the Climate Prediction Center (CPC) unified precipitation project that is underway at the National Oceanic and Atmospheric Administration (NOAA) was also considered (Chen et al., 2008). It is a long-term continental-scale product based on a dense network of rain-gauge data collected from multiple agencies. The CPC daily precipitation data used has a $0.5° \times 0.5°$ spatial resolution from 1979 onwards (https://psl.noaa.gov/data/gridded/). For model evaluation, all rainfall data are interpolated onto the same spatial grid as in WRF simulations.

### 2.2.2 Temperature datasets

Observed monthly surface temperature data are used for CMIP5 model evaluation. Surface temperature over land from the Climatic Research Unit Time Series (CRU TS) version 3 datasets (Harris et al., 2014) has a spatial resolution of $0.5° \times 0.5°$, for 1901-2006 (https://data.ceda.ac.uk/badc/cru/data/cru_ts/cru_ts_3.00). Global sea surface temperature (SST) is taken from the Hadley Centre Sea Ice and Sea Surface Temperature (HadISST) dataset (Rayner et al., 2003), with a $1.0° \times 1.0°$ resolution from 1870 onwards (https://www.metoffice.gov.uk/hadobs/hadisst/). To facilitate comparison with CMIP5 models, the two datasets are combined by bilinearly interpolating the data onto a uniform grid of 2.5° × 2.5°, from 1901 until 2005.

### 2.2.3 ECMWF reanalysis datasets

The European Centre for Medium-Range Weather Forecasts (ECMWF) produces a set of global atmospheric reanalysis datasets, which were used as the IBCs in WRF simulations. Here six-hourly ERA-Interim reanalysis (Dee et al., 2011) was used, at 0.75° × 0.75° resolution with 37 pressure levels from the ground up to 1 hPa, covering the period from January 1979 through

August 2019. In the attribution of the pre-monsoon heavy rainfall case, ERA5 reanalysis data (Hersbach et al., 2020) was used instead, due to its outperforming the ERA-Interim as forcing data used in simulations (not shown). ERA5 provides hourly estimates of atmospheric variables with a 0.25° × 0.25° spatial resolution and 37 pressure levels.

## 2.3 Model and experiment design

### 2.3.1 Model description

Numerical experiments were conducted using the Advanced Research WRF (WRF-ARM) model version 3.8.1 (Skamarock, 2008) in a one-way nesting setup. The three nested domains centered at the PRD region are shown in **Figure 2.1**. The outermost domain has a horizontal grid resolution of 50 km × 50 km (79 x 61 grid cells), covering most of southeast Asia. The middle and innermost domains encompass the SC and the entire PRD region, with resolutions of 10 km × 10 km (136 x 116 grid cells) and 2 km × 2 km (181 x 166 grid cells), respectively. There are 45 vertical layers from the surface up to 50 hPa, with 18 layers being concentrated in the lowest 1.5 km to resolve the planetary boundary layer (PBL) dynamics.

The main physical schemes employed for all the domains include the Bougeault-Lacarrere PBL scheme (Bougeault and Lacarrere, 1989), the rapid radiative transfer model for both shortwave and longwave radiation parameterizations (Iacono et al., 2008), and the unified Noah land surface model (Tewari et al., 2004). For multi-case analysis (see Chapter 3), the WRF single-moment six-class (WSM6) microphysics (Hong and Lim 2006) and the Grell 3D ensemble cumulus scheme (Grell and Dévényi, 2002) were used. For individual case study (see Chapters 4 and 5), different combinations from two microphysics schemes, i.e., the Thompson (Thompson et al., 2008) and WSM6 microphysics, and three cumulus parameterization schemes, namely the Kain-Fritsch (Kain and Kain, 2004), Betts-Miller-Janjic (Janjic, 1994) and Grell 3D schemes, were used for multi-physics ensemble integrations (see Chapter 2.3.2

for more details). In all simulations, the microphysics schemes were applied for all domains, whereas the cumulus schemes were enabled for the outer and middle domains but disabled for the innermost domain as its horizontal resolution is fine enough for the model to fully resolve the moist convective physics.

In addition, the sensitivity of WRF performance on SST update is checked for eighteen extreme rainfall events that occurred between April and September over the PRD. It was found that the magnitude of daily precipitation offshore is evidently underestimated in fixed SST runs (see **Figure 2.2b**); it becomes more comparable to observations when SST is updated during WRF integrations (see **Figure 2.2c**). As a result, the six-hour updated SST field was used in all simulations.

The spectral nudging approach has been widely adopted in regional model simulations to constrain large-scale features to be close to observations while allowing small-scale features to evolve freely (Aiguo Dai et al., 2020; C. Zhang et al., 2016). For this reason, spectral nudging was applied to the zonal and meridional wind components above 500hPa in the outermost domain only (P. Liu et al., 2012; Y. Ma et al., 2016), at a scale of approximately 1300 km (1500 km) in the zonal (meridional) direction. The strength of nudging is 0.0003 $s^{-1}$. Details about model descriptions can be found at http://www2.mmm.ucar.edu/wrf/users.

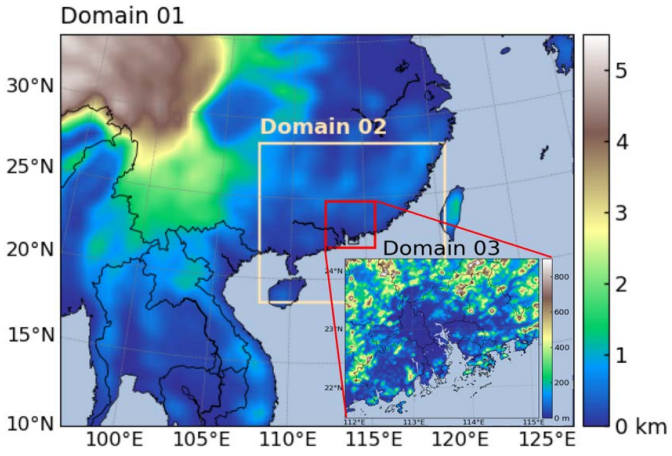

***Figure 2.1*** *Spatial distribution of topographic height (units: km) over the three nested domains in WRF.*

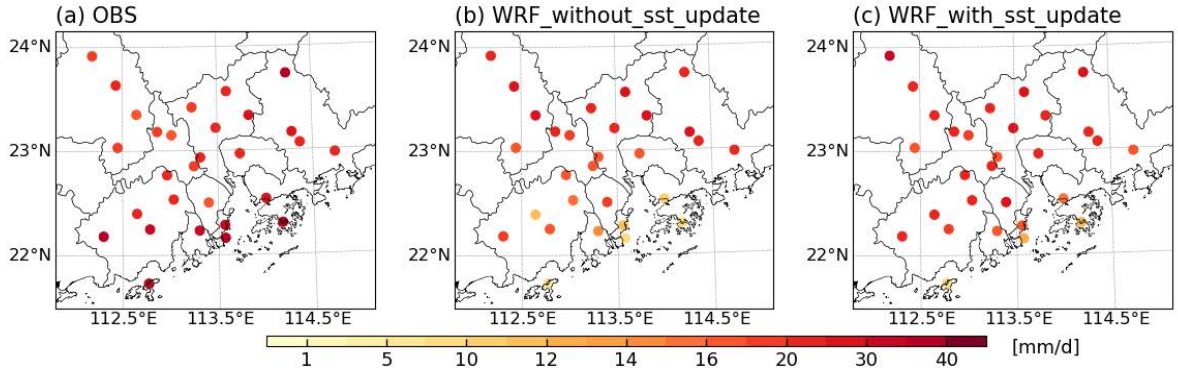


***Figure 2.2*** *Spatial distribution of the averaged daily precipitation (units: mm $d^{-1}$) occurred from April to September, obtained from (a) in-situ observations, (b) WRF simulations with fixed SST, and (c) WRF simulations with SST updated every six hours.*

### 2.3.2 Experiment design

In order to attribute the change in PRD precipitation extremes to human influences, a series of experiments were carried out by dynamically downscaling extreme rainfall events under various IBCs in WRF. In the first part of this work (see Chapter 3), WRF simulations of the selected extreme rainfall cases (see Chapter 2.4.1 for case selection) were conducted under the baseline and counterfactual climate conditions. Control simulations (hereafter referred to as CTL runs) were forced with IBCs taken from ERA-Interim reanalysis, which produces meteorological fields with both anthropogenic and natural forcings. The counterfactual simulations (referred to as NAT runs) were forced by the natural-forcing only IBCs, in which anthropogenic perturbations in the physical fields are removed through the PGW technique (see Chapter 2.4.3). Here the physical fields refer to surface and air temperature, specific humidity, and horizontal wind components. The difference in the two sets of runs thus represents the human impacts on rainfall extremes. Each experiment is integrated over a 5-day

period (see **Table 2.4**), with the first day discarded as spin-up time and the following analyses based on the remaining four days.

For the attribution of two specific extreme cases (see Chapter 4 for a wintertime rainstorm and Chapter 5 for a pre-monsoon heavy rainfall event), three sets of experiments (see **Table 2.1**) were designed to probe thermodynamic and dynamic contributions separately to heavy rainfall changes due to human influences. Besides the control runs mentioned above, two sets of counterfactual simulations were performed by forcing the model at the IBCs with 1) human-induced thermodynamic (i.e., temperature and specific humidity) perturbation removed (hereafter DTQ run), and 2) both human-related thermodynamic and dynamic (i.e., horizontal wind circulation) perturbations removed (hereafter DTQW run) from ERA-Interim. Hence, human-forced thermodynamic and dynamic variations that affect rainfall can be inferred from the difference of CTL and DTQ runs, as well as DTQ and DTQW runs, respectively.

It should be noticed that there might be large model uncertainty when picking one combination of physics parameterizations to do the downscaling using WRF. This is due to the fact that the sensitivity of climate variables to different physics schemes varies (Evans et al., 2012). Such uncertainty can be reduced by taking an average over all the simulated cases. When it comes to the individual case simulations, however, an ensemble of simulations is commonly produced to reduce model bias (S. Y. S. Wang et al., 2018).

For the extreme rainfall event of December 14-17, 2013 (see Chapter 4), a 6-member multi-physics ensemble based on the combination of two microphysics and three cumulus parameterization schemes (listed in **Table 2.2**) was generated, with integrations spanning from 0000 UTC 9 December to 0000 UTC 18 December 2013. The ensemble mean of the multi-physics integrations was used as it outperforms individual ensemble members in replicating the atmospheric circulation and precipitation. The first 48 hours were treated as spin-up and excluded in the subsequent analysis.

For the pre-monsoon precipitation on 15 May 2016 (see Chapter 5), it was found that a large ensemble was needed to reduce model uncertainties. Here, a 14-member ensemble comprising various initialization times and physics schemes was used (see **Table 2.3**). The simulations of ensemble members were initiated at a six-hour interval from 0000 UTC 12 May to 1200 UTC 13 May, all of which ended at 0000 UTC 18 May.

***Table 2.1*** *Model experiments for attribution of specific extreme events.*

| EXP | IBCs | Description |
|---|---|---|
| CTL | ERA-Interim (ERAI) | Factual climate with all forcing |
| DTQ | ERAI - Δ(T, Q) | Climate without human-forced thermodynamic change |
| DTQW | ERAI - Δ(T, Q, U, V) | Climate without human-forced thermodynamic and dynamic changes |

***Table 2.2*** *Six-member ensemble of different microphysics and cumulus schemes used in WRF.*

| No. | EXP | Microphysics | Cumulus schemes |
|---|---|---|---|
| 1 | WG3 | WSM6 | Grell 3D |
| 2 | WKF | WSM6 | Kain–Fritsch |
| 3 | WBMJ | WSM6 | Betts–Miller–Janjic |
| 4 | TG3 | Thompson | Grell 3D |
| 5 | TKF | Thompson | Kain–Fritsch |
| 6 | TBMJ | Thompson | Betts–Miller–Janjic |

***Table 2.3*** *A list of 14 ensemble members performed for the pre-monsoon rainfall simulation. See text for details.*

| No. | Starting time (UTC) | Microphysics | Cumulus schemes |
|---|---|---|---|
| 1 | 0000 12/05 | Thompson | Kain–Fritsch |
| 2 | 0600 12/05 | Thompson | Kain–Fritsch |
| 3 | 1200 12/05 | Thompson | Kain–Fritsch |
| 4 | 1800 12/05 | Thompson | Kain–Fritsch |
| 5 | 0000 13/05 | Thompson | Kain–Fritsch |
| 6 | 0600 13/05 | Thompson | Kain–Fritsch |
| 7 | 1200 13/05 | Thompson | Kain–Fritsch |
| 8 | 0000 12/05 | WSM6 | Kain–Fritsch |
| 9 | 0600 12/05 | WSM6 | Kain–Fritsch |
| 10 | 1200 12/05 | WSM6 | Kain–Fritsch |
| 11 | 1800 12/05 | WSM6 | Kain–Fritsch |
| 12 | 0000 13/05 | WSM6 | Kain–Fritsch |
| 13 | 0600 13/05 | WSM6 | Kain–Fritsch |
| 14 | 1200 13/05 | WSM6 | Kain–Fritsch |

## 2.4 Methods for modeling and analysis

### 2.4.1 Selection of extreme rainfall events

We define extreme precipitation as a day with regional accumulated daily rainfall greater than the 95$^{th}$ percentile of all wet days (> 0.1 mm d$^{-1}$) based on data averaged over the entire PRD region for the 1998-2018 period, using TRMM 3B42 data. The extreme case encompasses two days before and two days after the extreme precipitation day, spanning totally 5 consecutive days. All of the cases were classified as non-TC (tropical cyclones) cases, i.e., they were not induced by TC systems. 215 extreme rainfall cases were identified, and then reproduced by

WRF. They were evaluated against station observations, by comparing the root mean square error (RMSE) of the temporal and spatial distribution of daily precipitation, respectively (see **Figure 2.3**). Among these 200 and more cases, 40 well-reproduced extreme rainfall events (listed in **Table 2.4**) were chosen for attribution analysis. The further selected events were classified into two groups: 23 events during the rainy season (May to September, abbreviated as MJJAS) and 17 events during the rest of the calendar months (non-MJJAS). Only rainfall that falls over land was analyzed in this study.

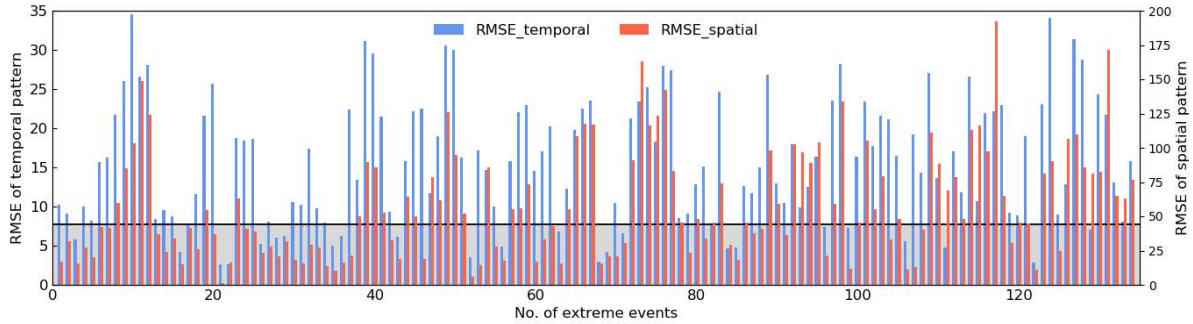


***Figure 2.3*** *The temporal (blue) and spatial (red) RMSE values (units: mm $d^{-1}$) for each extreme rainfall case.*

***Table 2.4*** *A list of case periods of the selected 40 extreme rainfall events that occurred in the rainy season (MJJAS) and non-rainy season (non-MJJAS).*

| **MJJAS (23 cases)** | | **Non-MJJAS (17 cases)** | |
|---|---|---|---|
| 09 - 14/06/2000 | 13 - 18/06/2010 | 13 - 18/02/1998 | 06 - 11/11/2011 |
| 07 - 12/05/2001 | 22 - 27/06/2010 | 29/03 - 03/04/2004 | 13 - 18/01/2012 |
| 09 - 14/06/2002 | 03 - 08/08/2010 | 21 - 26/03/2006 | 29/11 - 04/12/2012 |
| 29/06 - 04/07/2002 | 08 - 13/09/2010 | 19 - 24/11/2006 | 28/04 - 03/05/2013 |
| 11 - 16/06/2003 | 20 - 25/06/2012 | 22 - 27/04/2007 | 13 - 18/12/2013 |
| 10 - 15/05/2004 | 18 - 23/05/2013 | 23 - 28/01/2008 | 10 - 15/01/2015 |
| 06 - 11/06/2006 | 16 - 21/05/2014 | 03 - 08/10/2008 | 18 - 23/03/2016 |
| 24 - 29/07/2006 | 21 - 26/05/2015 | 20 - 25/04/2010 | 04 - 09/01/2018 |
| 17 - 22/05/2007 | 01 - 06/06/2017 | 10 - 15/10/2011 | |

| | | |
|---|---|---|
| 06 - 11/06/2007 | 05 - 10/09/2017 | |
| 26 - 31/05/2008 | 05 - 10/05/2018 | |
| 15 - 20/06/2008 | | |

### 2.4.2 Selection of CMIP5 GCMs

To eliminate the CMIP5 projections that are unable to mimic historical warming (Jones et al., 2013), we evaluated the decadal trends in surface temperature (ST) averaged over SC during the 1901-2005 period, obtained from the historical runs of 18 CMIP5 global models against the observed trend (see **Figure 2.4**). All of these models have both historical and natural-only forcing (historicalNat) runs available for that period. The ST trend was computed by subtracting the 1901-1920 means from the 1986-2005 means, and this difference was divided by the number of decades. 10 CMIP5 models (highlighted by the blue background in **Figure 2.4**) were found to give ST tends (> 0.04 °C per decade) comparable to the observed one (roughly 0.08 °C per decade). ST trend of the ten-model ensemble mean is 0.07 °C per decade. Previous studies also report similar underestimation in global models (Allan and Soden, 2008; Min et al., 2011).

Second, we compared ST in the historical run with that in the historicalNat run from individual GCMs (see **Figure 2.5**). Seven models were found to have noticeable differences between the two runs since 1980 or so (highlighted in blue in **Figure 2.5**), and thus were selected for obtaining robust human forcing signals. Outputs from the selected 7 GCMs were interpolated onto a 2.5° × 2.5° spatial grid for consistency. More detailed information about the selected CMIP5 models is listed in **Table 2.5**.

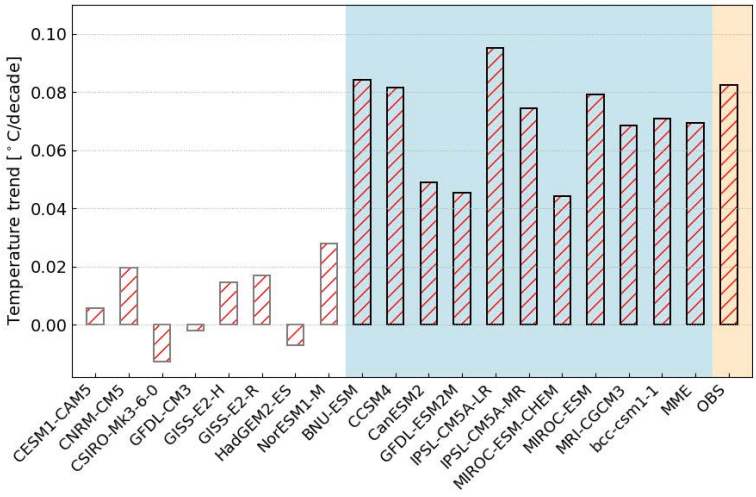


***Figure 2.4*** *Surface temperature trends (units: °C per decade) for the period of 1901-2005, averaged over domain 2 (SC), derived from the historical run of individual CMIP5 models. Also shown the selected models and multi-model ensemble mean (MME) highlighted by a blue background, as well as the observed trends (OBS) highlighted by an orange background. See text for details.*

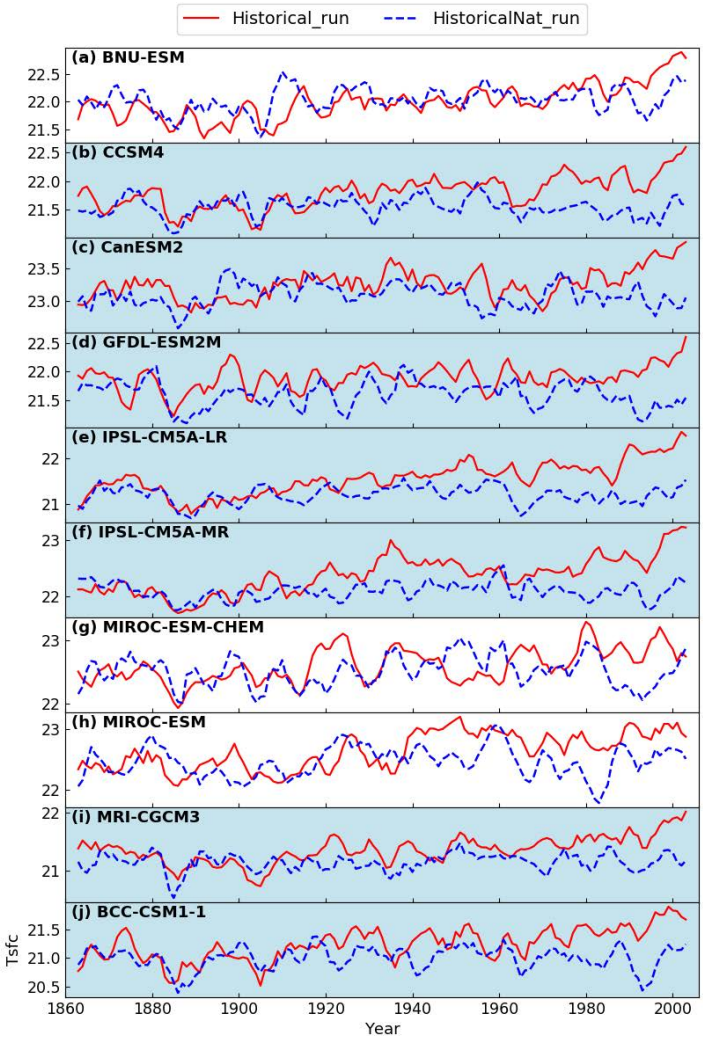


***Figure 2.5*** *Time evolution of annual mean surface temperature (units: °C) over the SC from 1861-2005 from the (a) BNU-ESM, (b) CCSM4, (c) CanESM2, (d) GFDL-ESM3M, (e) IPSL-CM5A-LR, (f) IPSL-CM5A-MR, (g) MIROC-ESM-CHEM, (h) MIROC-ESM, (i) MRI-CGCM3, (j) BCC-CSM1-1. Red and blue lines represent results from historical and historicalNat runs, respectively. Models selected for obtaining anthropogenic forcing signals are highlighted by the blue background. See text for details.*

***Table 2.5*** *Descriptions of the CMIP5 GCMs used in this study.*

| No. | IPCC ID | Institute and Country | Resolution (Lon×Lat) | Mean anomaly of initial $T_{sfc}$ in D02 (℃) |
|---|---|---|---|---|
| 1 | Bcc-csm1-1 | Beijing Climate Center, China Meteorological Administration, China | 128×64 | 0.63 |
| 2 | CanESM2 | Canadian Centre for Climate Modelling and Analysis, Canada | 128×64 | 0.61 |
| 3 | CCSM4 | National Center for Atmospheric Research, USA | 288×192 | 0.74 |
| 4 | GFDL_ESM2M | Geophysical Fluid Dynamics Laboratory, USA | 144×90 | 0.72 |
| 5 | IPSL-CM5A-LR | L'Institut Pierre-Simon Laplace, France | 96×96 | 1.03 |
| 6 | IPSL-CM5A-MR | L'Institut Pierre-Simon Laplace, France | 96×96 | 0.79 |
| 7 | MRI-CGCM3 | Meteorological Research Institute, Japan | 256×128 | 0.62 |

### 2.4.3 PGW downscaling technique

The PGW technique was applied in our counterfactual simulations with the absence of human influences. Human-induced perturbation of field *X*, i.e., $\Delta X_{CMIP5}$, is derived from the monthly average of the twenty-year (1986-2005) mean difference between historical and historicalNat runs of the CMIP5 seven-model ensemble mean:

$$\Delta X_{\_CMIP5} = \overline{(X_{\_historical} - X_{\_historicalNat})}|_{1986\text{-}2005} \qquad (2.1)$$

It should be recalled that the ensemble mean of the selected 7 GCMs underrates the observed ST trend (see Chapter 2.4.2). Here we defined a ratio of observations (OBS) to multi-model ensemble-mean (MME) projections as the scale factor that is multiplied by the ensemble-mean perturbations, to resolve a more realistic anthropogenic perturbation, $\Delta X_{\_CMIP5}|_{adjusted}$:

$$\Delta X_{\_CMIP5}|_{adjusted} = \frac{OBS}{MME} \times \Delta X_{\_CMIP5} \quad (2.2)$$

where OBS and MME refer to the observed and CMIP5-produced trends of ST, respectively, derived from **Figure 2.4**. Consider that the difference between temperature in GCM's simulations and observations varies slightly with seasons (not shown), we adjusted human-induced perturbations in different seasons by the same scale factor. Then, the adjusted monthly perturbations were interpolated linearly on each model grid over the outermost domain for the corresponding case simulations, after that, subtracted from the IBCs (ERA-Interim) in WRF. One potential drawback of applying this adjustment approach is that we used the scale factor derived from temperature trends to adjust perturbations in all physical fields (see details in Chapter 2.3.2). In fact, with the exception of temperature observations, there are few good-coverage and high-quality gauge-based data available for model validation. We thus assume that the GCM's bias on temperature is representative of biases on other variables, and that this would not substantially alter the results.

Noted that changes in meteorological fields due to anthropogenic influences vary significantly among the individual CMIP5 models (Lauer et al., 2013). The use of the multi-model ensemble mean in Eq. (2.1) can minimize such model uncertainty and internal climate variability (Liu et al., 2017). Based on this seven-model ensemble mean, monthly anomalies of surface and 1000-300 hPa tropospheric temperature, as well as low-level specific humidity (1000-850 hPa), are computed (see **Figure 2.6**). During the MJJAS season, the mean surface (troposphere) has warmed by about 1℃ (1.2℃), and low-level water vapor increment reaches approximately 0.7 g $kg^{-1}$ under warming.

The above approach is equivalent to the reverse of the PGW method described by Kimura and Kitoh (2007) and Sato et al. (2007). The method allows one to estimate the anthropogenic influences on a specific extreme event, which makes it easier to perform event attribution

analysis based on dynamical downscaling. However, one should also note the difference in resolution, parameterization schemes used between the regional and global models (Chen et al., 2019); sufficient spin-up time is required to ensure the regional model components reach equilibrium after applying climate perturbations. For each case, the 11-day WRF simulations over the outermost domain for the baseline and counterfactual climates were carried out, starting from 3 days before the control run. The latter 8-day mean differences in output fields (see Chapter 2.3.2 for physical fields used in each experiment) between the control and counterfactual runs were computed as adjusted natural-forced perturbations. They were then subtracted from baseline IBCs and regarded as adjusted anthropogenic perturbations.

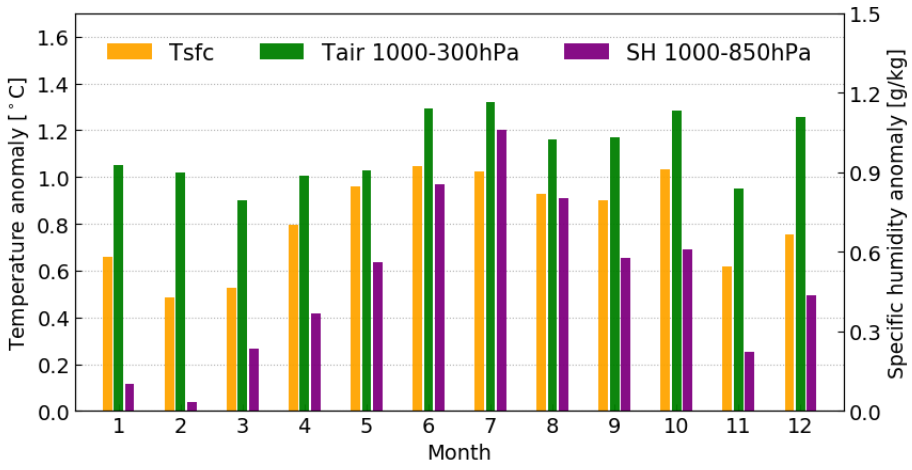


***Figure 2.6*** *Monthly differences in surface temperature (orange bar, units:* ℃*), tropospheric temperature (green bar, units:* ℃*) averaged from 1000-300 hPa and specific humidity (purple bar, units: g kg$^{-1}$) averaged from 1000-850 hPa averaged from 1986-2005 over the SC between historical and historicalNat runs of CMIP5 seven-model ensemble mean. See text for details.*

### 2.4.4 Moisture budget analysis

The moisture budget analysis was also used to study extreme rainfall changes under a human-induced warming climate. The moisture budget equation is expressed as follows:

$$\frac{\partial < q >}{\partial t} = E - P - < \nabla \cdot \vec{V} q > \qquad (2.3)$$

where $<\cdot> = -\frac{1}{\rho_\omega g}\int \cdot \, dp$, denotes column-integration through the 1000-100 hPa troposphere, $\rho_\omega$ and $g$ are the density of water and the acceleration of gravity, respectively, and $p$ is pressure. The LHS term in Eq. (2.3) is the rate of change of total water vapor. On the RHS, $E$ is surface evaporation, $P$ is precipitation, q is specific humidity, and $\vec{V}$ is horizontal vector winds. The third term on the RHS describes vertical-integrated moisture flux convergence (VIMFC).

Noted that evaporation ($E$) and water vapor changes ($\frac{\partial <q>}{\partial t}$) are relatively small for intense rainfall events (Banacos & Schultz, 2005), precipitation is primarily balanced by the VIMFC term. Hence, the human-induced changes in precipitation $\delta P$ could be estimated by

$$\delta P \approx -\delta < \nabla \cdot \vec{V} q >$$

$$\approx -< \delta q \nabla \cdot \vec{V}_{CTL} > - < \delta \vec{V} \cdot \nabla q_{CTL} >$$

$$- < q_{CTL} \nabla \cdot \delta \vec{V} > - < \vec{V}_{CTL} \cdot \nabla \delta q > + NL \qquad (2.4)$$

where $\delta$ represents for the variations resulting from human influences, i.e., the control minus counterfactual runs. Subscripts CTL denotes the control run. The nonlinear term ($NL$), such as surface quantities and changes in both mean humidity and winds, is ignorable due to its small contribution (Seager et al., 2010). The transient eddies are also neglected in progressing Eq. (2.3) to Eq. (2.4) because of the small deviation from their time mean.

In order to examine the thermodynamic and dynamic contributions to precipitation changes, Eq. (2.4) is further divided into

$$TH = -< \nabla \cdot \left( \vec{V}_{CTL} \, \delta q \right) > \qquad (2.5)$$

$$DY = -< \nabla \cdot \left( q_{CTL} \, \delta \vec{V} \right) > \qquad (2.6)$$

following Seager et al. (2010) and Lee et al. (2017). The thermodynamic contribution ($TH$) in Eq. (2.5) is associated with changes in water vapor; the dynamic contribution ($DY$) in Eq. (2.6)

is related to wind circulation changes. All these terms were calculated based on daily outputs in each model grid.

# Chapter 3 Attribution of extreme rainfall characteristics to human influences based on multi-case simulations

In this chapter, 40 extreme rainfall events that occurred over PRD are chosen and reproduced using the WRF model, under climate conditions with and without human forcing. Differences between the two sets of simulations can be attributed to human influences. Variations in both frequency and magnitude of those extremes caused by human activities are quantified. The seasonal dependence of rainfall changes is further examined, in terms of the MJJAS and non-MJJAS seasons. To understand the mechanism responsible for these changes, moisture budget analysis was used to assess changes in dynamic and thermodynamic components that affect rainfall changes.

## 3.1 WRF model evaluation

### 3.1.1 Evaluation of synoptic conditions

Before carrying out the attribution analysis, we first evaluate the model's performance in capturing prognostic variables that affect the rainfall processes, and also characteristics of precipitation extremes. **Figure 3.1** compares the multi-case mean temperature, geopotential height, and horizontal wind circulation at different pressure levels simulated by WRF CTL runs with ERA-Interim data. Both wind patterns and magnitudes at various levels over the South China PRD area were replicated by WRF reasonably well, with improved capability to simulate the 250-hPa wind circulation due to the use of spectral nudging. Over PRD, WRF reproduces a warmer mid-to-upper troposphere, especially at the 500-hPa level, while there is no appreciable difference in low-level temperature as compared to observations (see **Figure 3.1c, f, i**). It can also be seen that WRF slightly overpredicts the geopotential heights at 250 hPa and 500 hPa,

but underestimates the 850-hPa geopotential height in this domain. During extreme rainfall events, a strong upper-level westerly is observed over the mid-latitudes, accompanied by a low-level southwesterly wind over SCS and northeast flow over the northern area (see **Figure 3.1a, d, g**). It is noticed that winds at 250-hPa and 500-hPa levels become strong in the East China Sea in the WRF simulations, but the location is far from our target region.

Simulated precipitable water, moisture flux transport, and 500-hPa vertical velocity are also compared with ERA-Interim (see **Figure 3.2**). The results indicate that precipitable water and moisture transport over SC match well with reanalysis, although moisture amounts over some inland areas are slightly overestimated (see **Figure 3.2c**). On the other hand, there is a negative bias in precipitable water over the ocean and marine continents of ~7 mm (i.e., ~9% relative to reanalysis), with enhanced northward moisture transport also seen in the WRF simulations. The observed ascending centers (see black contours in **Figure 3.2a**) are accurately captured by the model, albeit with a slight westward shift over SC. These comparisons overall demonstrate WRF's ability to reproduce essential synoptic features in the region.

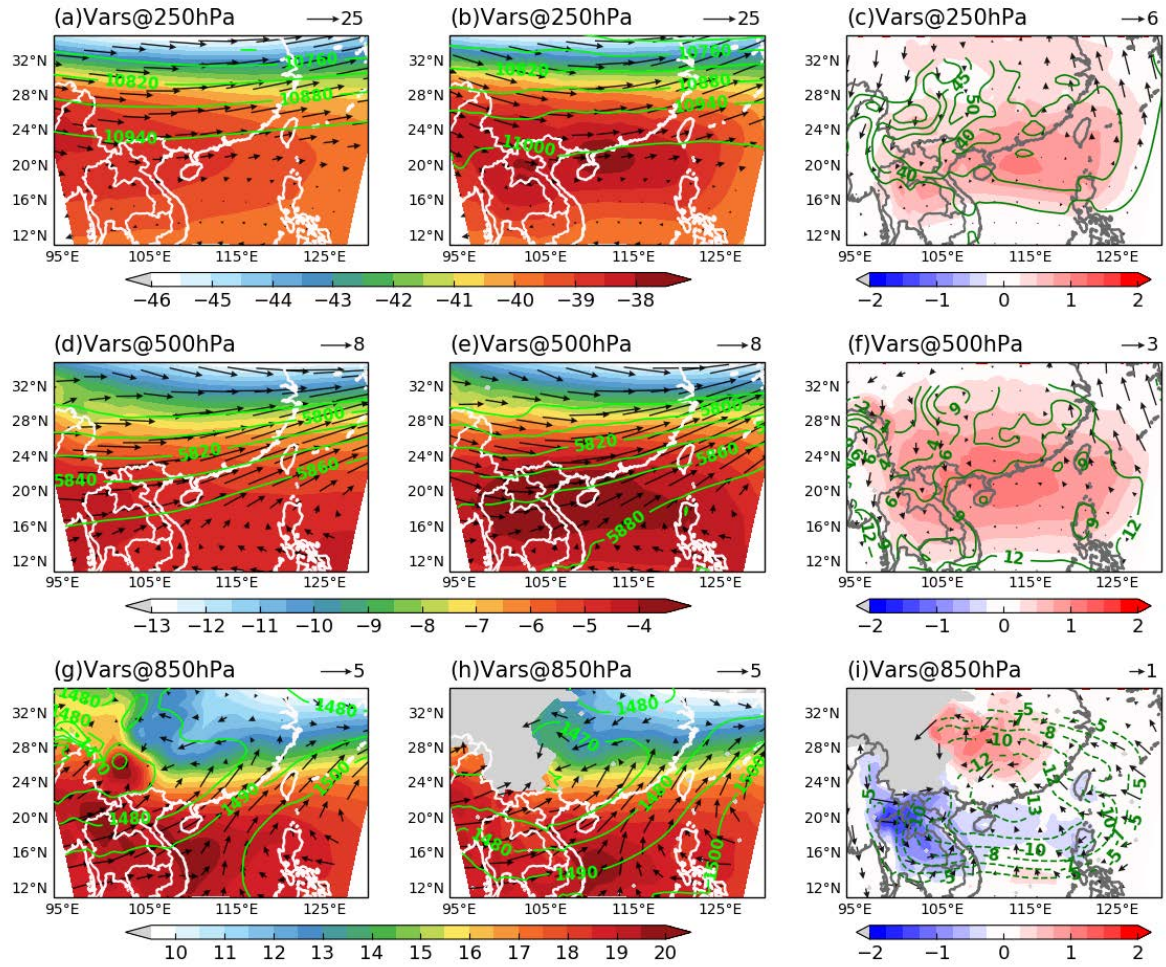


***Figure 3.1*** *Comparison in composite fields between model simulations and observations. Air temperature (shading, units: ℃), geopotential height (contour, units: m) and horizontal wind circulation (vectors, units: m* $s^{-1}$*) at (a, b, c) 250 hPa, (d, e, f) 500 hPa and (g, h, i) 850 hPa, respectively. These fields are computed from the temporal average of the entire extreme rainfall cases over the outermost domain from (a, d, g) ERA-Interim reanalysis and (b, e, h) WRF CTL simulations, as well as (c, f, i) their differences, i.e., CTL simulations minus ERA-Interim. The reference scale vectors are shown at the top right.*

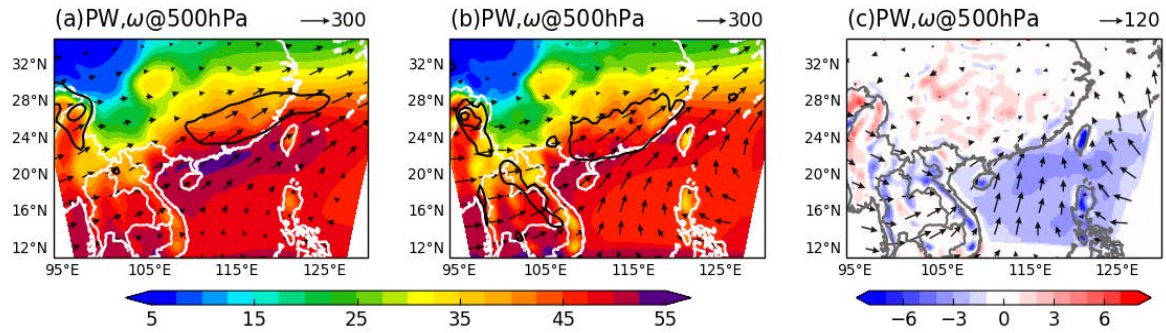


***Figure 3.2*** *Same as* ***Figure 3.1****, but for precipitable water (shading, units: mm), 500-hPa pressure velocity (< -0.1 Pa* $s^{-1}$ *shown by black contours), and column-integrated moisture flux transport (vectors, units: kg* $m^{-1}$ $s^{-1}$*). The reference scale vectors are shown at the top right.*

### 3.1.2 Rainfall validation

Simulated intensity and frequency of daily rainfall extremes are also compared with comparing with observations. **Figure 3.3** presents the daily-mean rainfall in the outermost WRF domain and those based on TRMM satellite and rain gauges. The maximum rainfall zone concentrated over Guangdong Province (109.6˚-117.3˚E, 20.1˚-25.6˚N) of China is successfully captured by the model, with intensities comparable to gauge-based observations (see **Figure 3.3b, c**). However, the simulated magnitude of daily precipitation in the middle and eastern Guangdong Province is found to be about 8 mm per day (~28%) smaller than TRMM 3B42 data (see **Figure 3.3a**). This, however, might be due to the overestimation of heavy precipitation by TRMM 3B42 (X. Huang et al., 2018; Prakash et al., 2016).

We use stational observations to further examine the simulated daily rainfall over PRD. Each station observation is directly compared with the nearest model grid output. It can be seen that rainfall over inland areas agrees well with in-situ observations, with a low bias of within 7 mm $d^{-1}$; on the other hand, the coastal rainfall is noticeably underpredicted by WRF, with a relatively large bias of ~10 mm $d^{-1}$ or more (see **Figure 3.4a, b, c**). The probability density function (PDF) of daily rain intensities based on wet days (> 0.1 mm $d^{-1}$) from all selected extreme events is

shown in **Figure 3.4d**. There is a less frequent occurrence of moderate to heavy precipitation (> 20 mm $d^{-1}$), and a higher frequency of light rainfall (< 10 mm $d^{-1}$) in WRF when compared with observations. The relative bias of simulated frequency is roughly 15.6% averaged for rain rates in 10~200 mm $d^{-1}$, demonstrating that WRF overestimates the rainfall frequency. This underestimation of heavy rainfall frequency probably resulted from the less intense coastal rainfall in WRF (see **Figure 3.4b**). In general, the model is able to reproduce the large-scale synoptic conditions of those extreme events over the PRD region, with reasonable magnitude and frequency of daily precipitation.

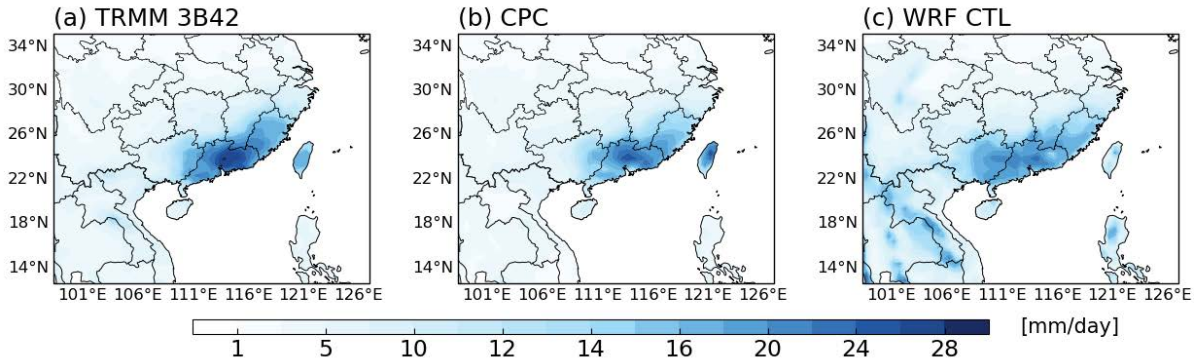


***Figure 3.3*** *Daily precipitation (units: mm $d^{-1}$) averaged from all the selected extreme rainfall events during the period of 1998-2015 over the outermost domain, obtained from (a) TRMM 3B42 satellite product, (b) CPC gauge-based observations, and (c) WRF CTL simulations.*

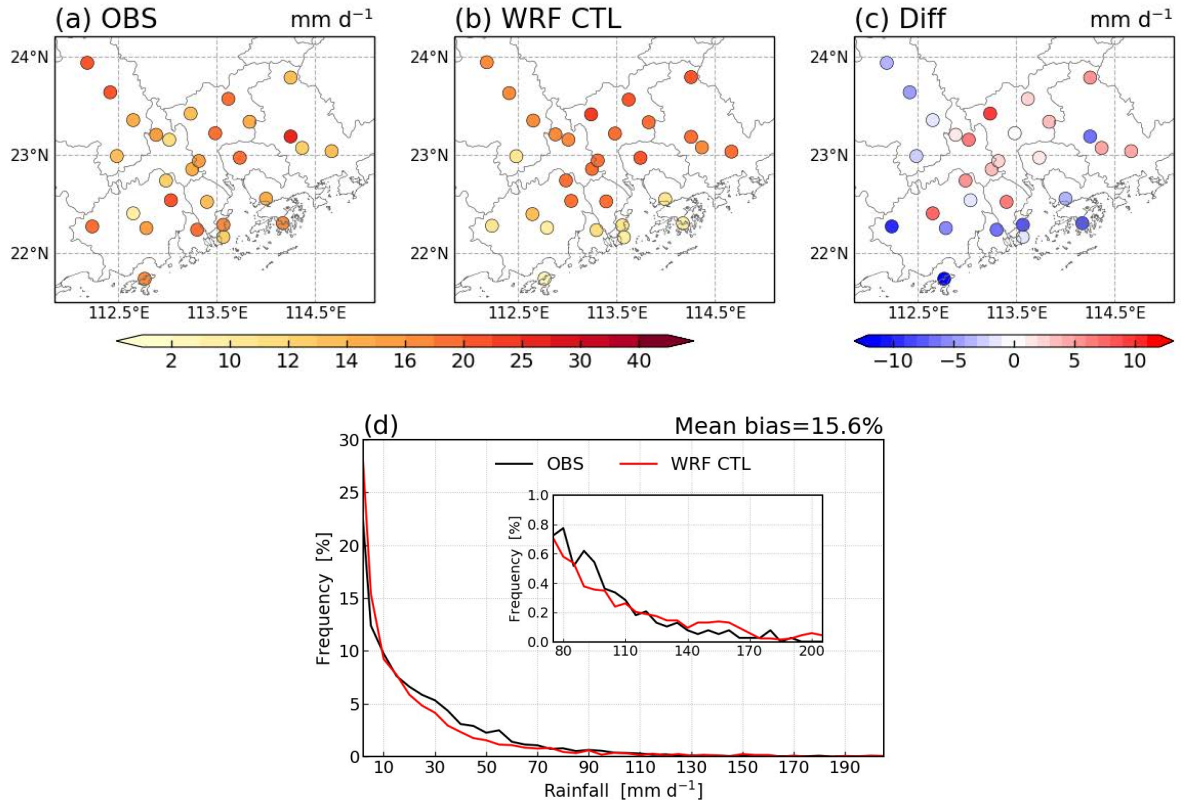


***Figure 3.4*** *Daily precipitation (units: mm $d^{-1}$) averaged from all the extreme rainfall events over the PRD (D03), from (a) station observations (OBS), (b) WRF control runs (CTL), and (c) their difference, i.e., CTL minus OBS. (d) Probability density function (PDF) distribution of daily rainfall over the PRD from OBS (black) and CTL (red). Mean bias shown at the upper right, is defined as the frequency difference between CTL and OBS relative to OBS. The insert figure depicts the PDF of heavy to extreme rainfall that rain rates greater than 80 mm $d^{-1}$.*

## 3.2 Attribution analysis

### 3.2.1 Human influences on temperature

Human influences on PRD rainfall extremes and related regional climate are now investigated by comparing the control and counterfactual simulations (see Chapter 2.3.2 for details of experiments design). **Figure 3.5** depicts human impacts on the near-surface and tropospheric temperature averaged over extreme events selected for MJJAS and non-MJJAS seasons. As

seen from vertical profiles of air temperature anomaly, i.e., the CTL minus NAT runs (see **Figure 3.5a**), the 1000-500 hPa tropospheric temperature averaged from the entire events in PRD has increased by roughly 0.9 ℃, which can be attributed to human activities. Within the 1000-300 hPa layer, extreme cases in the non-MJJAS season clearly show a stronger vertical gradient of temperature anomaly than cases in MJJAS do. The spatial distribution of 2-m temperature change over PRD suggests that anthropogenic forcing has led to an increase of near-surface temperature by 0.9 to 1.1 ℃ for cases in MJJAS and 0.6 to 0.8 ℃ in non-MJJAS season (see **Figure 3.5 b, c**). More robust anthropogenic warming is seen over PRD megacities than in surrounding rural areas, regardless of seasons. Also, the land surface tends to warm up more noticeably than oceanic areas, indicating a larger land-sea contrast in MJJAS due to human influences, which is consistent with previous research (Joshi et al., 2008).

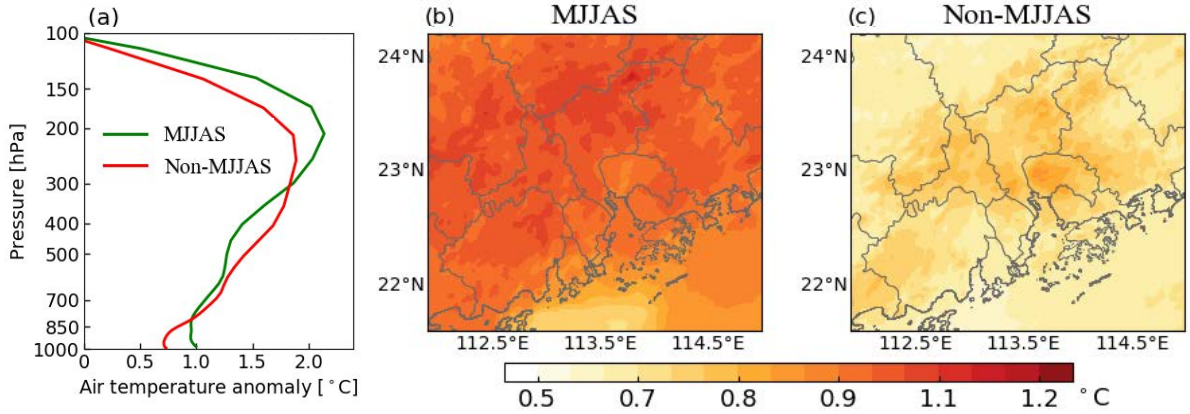


***Figure 3.5*** *Difference between temperature (units: °C) from CTL and NAT runs over the PRD region during MJJAS (b) and (c) non-MJJAS season at 2m, as well as (a) vertical profiles of its area-averaged values.*

### 3.2.2 Human-induced variations in rainfall characteristics

The magnitudes of daily-mean and extreme (above 95$^{th}$ percentile) precipitation based on all the selected cases from the CTL and NAT simulations, as well as the corresponding relative changes, are depicted in **Figure 3.6** and **Figure 3.7**, respectively. Relative changes in rainfall

here are computed from the difference between CTL and NAT runs relative to NAT runs. As seen from daily-mean rainfall in CTL (see **Figure 3.6a, d**), the maximum rainfall is over 45 mm $d^{-1}$ in MJJAS, and it reaches 34 mm $d^{-1}$ in the non-MJJAS season. The rainfall center in MJJAS is located in the northeastern part of PRD, while it is seen over Guangzhou city (23.07°N in latitude and 113.15°E in longitude) for non-MJJAS. In addition, low-level southwesterly winds are dominant over PRD in MJJAS; in non-MJJAS season, the winds have more southerly components. Rainfall in NAT becomes less intense over most inland areas in the absence of human influences, especially in non-MJJAS as the rainfall core disappeared (see **Figure 3.6b, e**). In particular, human-related warming has intensified daily-mean rainfall substantially by 10~70% over inland while suppressing coastal rainfall by around 20%, as seen from the relative changes in **Figure 3.6c, f**. This reflects a slight northward shift of heaviest rainfall in CTL, which is likely contributed by the relatively stronger southerly winds in this run, bringing adequate moisture from SCS to inland areas. For extreme rainfall (above 95$^{th}$ percentile), the maximum rainfall reaches 243.5 mm $d^{-1}$ (247.5 mm $d^{-1}$) in CTL and 230 mm $d^{-1}$ (234.3 mm $d^{-1}$) in NAT runs for the cases in MJJAS (non-MJJAS) season (see **Figure 3.7a, b, d, e**). Similar results of rainfall pattern changes are found for extreme precipitation, but with more robust anomalous signals (see **Figure 3.7c, f**). These greater changes reflect that extreme rainfall in PRD is more sensitive than the mean to anthropogenic warming, regardless of seasons. This result is corroborated in many regions of the globe based on climate models (M. R. Allen & Ingram, 2002; Emori & Brown, 2005; Myhre et al., 2019).

Human-induced variations in daily rainfall frequency during different seasons are also analyzed based on all wet days. Compared to the CTL runs, the frequencies in NAT are enhanced for light to moderate rainfall ($\leq$ 50 mm $d^{-1}$ in MJJAS and 30 mm $d^{-1}$ in non-MJJAS), but are reduced for heavy to extreme rainfall as a result of anthropogenic warming (see **Figure 3.8**). To quantify such human-induced frequency changes, the ratio of rainfall frequency in the CTL

runs relative to the NAT runs is computed and given by the black line in the insert figure of **Figure 3.8**. It can be seen from **Figure 3.8a** that for cases in MJJAS, their frequency ratios increase gradually from 1.1 to over 1.3, with increasing rain rates of above 80 mm $d^{-1}$. In other words, human influences are responsible for a 10~30% increment in the occurrence of extreme daily rainfall in MJJAS. For non-MJJAS cases, their probability ratio increases linearly up to over 1.4 and then decrease below 1.1 when rain rates exceed 150 mm $d^{-1}$ (see **Figure 3.8b**), corresponding to above 99$^{th}$ percentile (see **Figure 3.9b**). The reduction of frequency ratio may be related to the short number of such extreme rain rates in non-MJJAS compared to MJJAS. The further comparison indicates that the ratios in non-MJJAS are greater than those in MJJAS for rain rates between 80 and 170 mm $d^{-1}$, implying that non-MJJAS rainfall occurs more frequently with warming. The more extreme precipitation occurs, the more latent heat can be released to warm up the middle troposphere (see red line in **Figure 3.5a**). Overall, anthropogenic warming contributes to an increase in the frequency of heavy precipitation (> 80 mm $d^{-1}$) of at most 34% and 42% for the MJJAS and non-MJJAS season, respectively. Similar changes in precipitation frequency are also found for tropic rainfall extremes (Chou et al., 2012).

We next examine changes in daily precipitation intensity in response to human-induced warming. **Figure 3.9** provides the distribution of rainfall intensity in the CTL and NAT runs, as well as the corresponding relative changes, for percentiles from 85% to 99.5% of daily rainfall, with a 0.1% bin interval. The relative changes of rainfall in MJJAS show a continuous increase from 6% to 10% for 85$^{th}$ to 97$^{th}$ percentile rainfall and then drop to 8% when rain rates exceed 97$^{th}$ percentile (see **Figure 3.9a**), though the corresponding frequency keeps rising along with rain rate increases (see **Figure 3.8a**). The mean rate of increase with a 0.9~1.1 ℃ domain-averaged near-surface warming derived from **Figure 3.5b** reaches roughly 8%, nearly the CC scaling of 7% $K^{-1}$ (see **Figure 3.9a**). By contrast, increases in non-MJJAS rainfall intensity (< 95$^{th}$ percentile) are found to be more variable, peaking at 12.4%, followed by a substantial

reduction when rain rates exceed the 97$^{th}$ percentile (see **Figure 3.9b**). The overall magnitude in the 85-99$^{th}$ percentile rainfall (above 40 mm d$^{-1}$) is enhanced by 7~12% for a 0.6~0.8 ℃ warming (see **Figure 3.5c**), representing a super-CC increase (see **Figure 3.9b**). This suggests that, in addition to the thermodynamic effect, there is positive dynamic feedback on non-MJJAS heavy rainfall, which will be analyzed in the following section. In particular, the rates of increase in the 95$^{th}$ (99$^{th}$) percentile rainfall are 9% (8.4%) and 12% (7%) for MJJAS and non-MJJAS, respectively.

To summarize, human-induced climatic warming has resulted in more frequent and heavier precipitation in both seasons over PRD, with non-MJJAS experiencing a greater increase in extreme rainfall (95$^{th}$-98$^{th}$ percentile). Nonetheless, for very extreme rainfall (> 99$^{th}$ percentile), both frequency and intensity increase less robustly in non-MJJAS than in MJJAS, based on the multi-case simulations. The possible mechanism will be discussed in the following section.

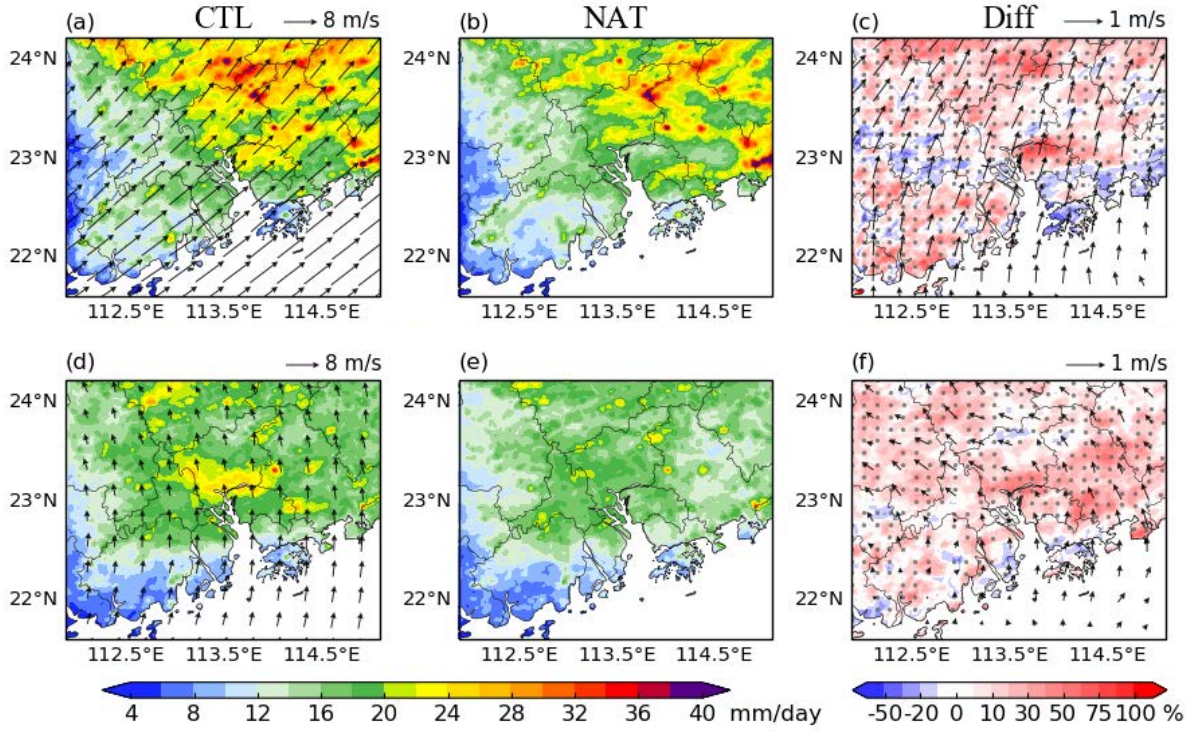


***Figure 3.6*** *Daily precipitation (shading; units: mm d$^{-1}$) and 850-hPa horizontal winds (arrows; see the scale at upper right in units of m s$^{-1}$) averaged from the cases in (a, b, c) MJJAS and (d,*

*e, f) non-MJJAS seasons over PRD area for (a, d) CTL, and (b, e) NAT runs, as well as (c, f) the relative change (Diff) between the two runs. Grey dots indicate rainfall changes passing the 90% significance level according to the Student's t-test. See text for details.*

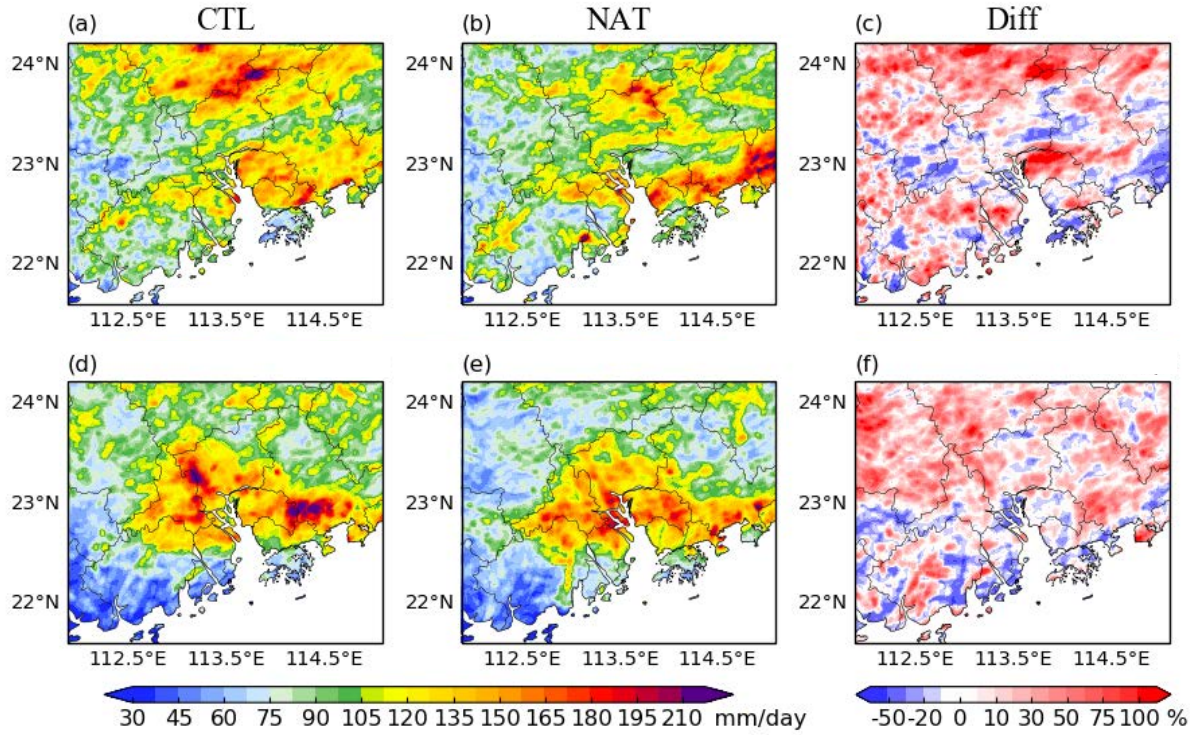


***Figure 3.7*** *Same as* ***Figure 3.6****, but for extreme daily precipitation (above 95$^{th}$ percentile).*

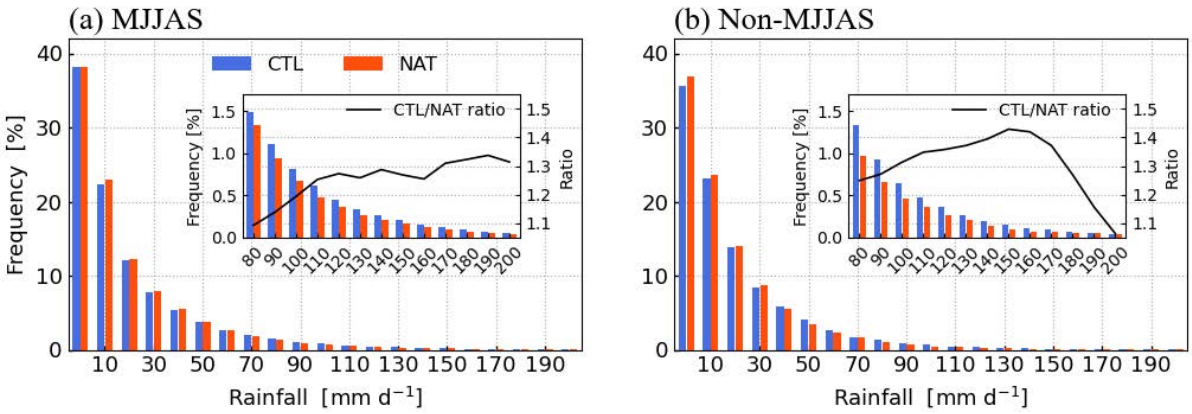


***Figure 3.8*** *Probability density function (PDF) of daily precipitation (units: mm d$^{-1}$) in CTL (blue bar) and NAT (red bar) runs over PRD region for the events in (a) MJJAS and (b) non-MJJAS seasons. The ratio between rainfall frequency given by CTL and NAT runs for rain rates*

*greater than 80 mm per day is also shown by black lines in the insert figures.*

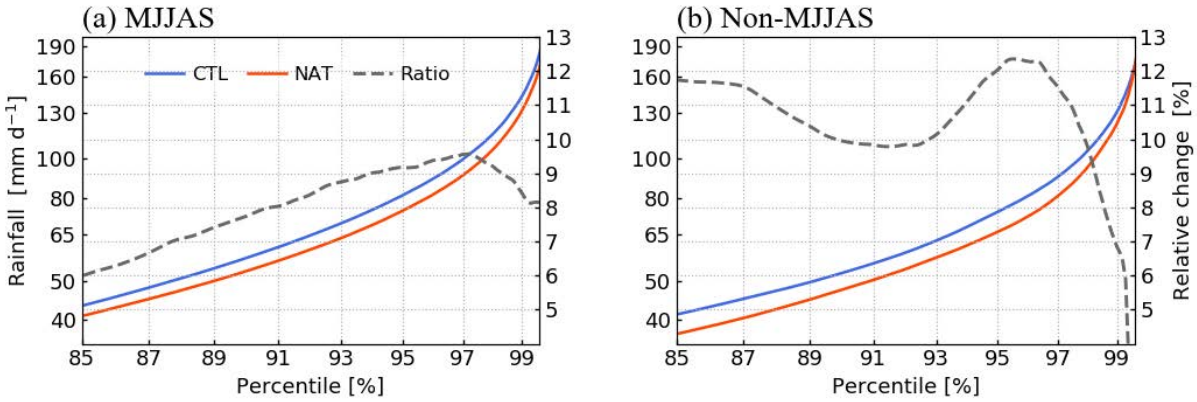


***Figure 3.9*** *Distributions of daily precipitation (units: mm $d^{-1}$) over PRD from CTL (blue line) and NAT (red line) runs, as well as their relative changes (grey dashed line) for (a) MJJAS and (b) non-MJJAS seasons.*

## 3.3 Contributions from thermodynamic and dynamic processes

The above results suggest that human-forced variations in extreme precipitation in non-MJJAS do not meet the moisture-driven CC relationship. Thus, we inspected changes in dynamic and thermodynamic components that contribute to extreme precipitation variability. Human influence on 850-hPa wind circulation is depicted in **Figure 3.10**, based on an average of cases from different seasons. For cases in MJJAS, a low-level anticyclonic anomaly is found to be centered over the eastern Guangdong province (see **Figure 3.10a**). Its southerly wind branch supports wetter-than-normal conditions over PRD and thus intensifies rainfall; In non-MJJAS, the stronger northeasterly winds south of 30°N along the east coast are favorable for cold and dry air moving southward, whereas easterly and southeasterly winds over SCS transport moist and warm air to the PRD region (see **Figure 3.10b**). The confluence of these two air streams strengthens the low-level moisture convergence. Besides, it can be inferred from the prominent northeasterly flow in non-MJJAS that the East Asian winter monsoon appears to be stronger under the anthropogenic warming climate.

Besides horizontal wind circulation, the vertical motion also changes as the climate warms. Following Emori and Brown (2005), the pressure velocity at 500 hPa was used to inspect changes in the vertical motion. **Figure 3.11** gives the PDF of 500-hPa pressure velocity over PRD from CTL and the corresponding changes relative to NAT for both seasons. The vertical velocity associated with nonprecipitating days is excluded here. Positive (negative) values indicate a downward (upward) movement. Interestingly, the MJJAS rainfall is not always strictly related to the 500-hPa upward motion (see **Figure 3.11a**). The frequency of ascends and descends in CTL distributes nearly symmetrically. Their relative changes exhibit a "V" shape, with less frequent occurrence of the weaker vertical motion and more occurrence of the stronger vertical motion, in terms of both ascending and descending branches (see grey dashed line in **Figure 3.11a**). Unlike MJJAS, CTL simulations for non-MJJAS indicate preferred upward motion than downward motion (see **Figure 3.11b**). Under anthropogenic warming, it is evident that the ascent tends to be more frequent while descent becomes less frequent, with relative changes of less than $\pm$5%. The stronger the ascent is, the more frequently the stream occurs. The redistribution of 500-hPa vertical velocity frequency in non-MJJAS implies strengthening of the mean vertical motion. This could account for the pronounced increase in the frequency and intensity of heavy rainfall in non-MJJAS (see **Figure 3.8** and **Figure 3.9**). On the other hand, there is a wider range of vertical velocity change in MJJAS than in non-MJJAS, especially for stronger ascent and descent. This indicates that human activities exert a more remarkable influence on vertical motion in MJJAS.

The total moisture flux transport and convergence over PRD in two seasons are now examined (**Figure 3.12**). The distribution of 1000-100hPa vertical-integrated moisture flux convergence (MFC) difference between CTL and NAT is similar to the distribution of precipitation difference, as can be seen in **Figure 3.6c, f**. The domain-averaged MFC rise to 4.7 mm $d^{-1}$ in MJJAS and 3.6 mm $d^{-1}$ in non-MJJAS. In both seasons, southwesterly winds transport moisture

to the inland areas of PRD, with the increased moisture flux transport in MJJAS is attributable to human-induced warming (see **Figure 3.12a**). Enhanced moisture transport in MJJAS contributes to the more intense rainfall over the northern PRD (see **Figure 3.6c**).

**Figure 3.13** gives the relative changes between CTL and NAT of precipitable water, defined as column-integrated water vapor, and 500-hPa pressure velocity with different percentile bins of daily precipitation. To estimate upward motion changes, only negative pressure velocity is computed. Regardless of the season, human-induced precipitable water and vertical velocity changes are positive for almost every percentile bin, indicating positive thermodynamic and dynamic contributions to precipitation intensification. Further inspection reveals that cases in MJJAS have a more consistent increase in both water vapor and vertical motion than cases in non-MJJAS. In particular, the associated precipitable water in MJJAS is enhanced as large as 6~7%, which adheres to the CC relation, and the 500-hPa pressure velocity increases by 4~8% (see **Figure 3.13a**). In the non-MJJAS season, both of them peak at about 12% at the 97$^{th}$ percentile of rainfall (see **Figure 3.13b**). Variations in precipitable water are similar to changes in rainfall intensity (see **Figure 3.9b**), ranging from 4% to 12%. It is noteworthy that the less increment in the very extreme rainfall (> 99$^{th}$ percentile) in non-MJJAS than in MJJAS mentioned above is limited by water vapor changes, albeit with the greater enhancement of vertical motion is seen in non-MJJAS. This suggests that the thermodynamic effect of increased water vapor has a dominant contribution to extreme rainfall variations, which is consistent with previous studies (Chou et al., 2012; Emori & Brown, 2005).

Dynamic effects of stronger wind circulation contribute more to very extreme rainfall (>97$^{th}$ percentile) compared to the thermodynamic effect in non-MJJAS season, while the opposite is true for MJJAS. Furthermore, a greater enhancement in precipitable water amount and ascend is found in non-MJJAS days, which is responsible for more intense and frequent rainfall for the 95$^{th}$~98$^{th}$ percentile (see **Figure 3.8b** and **Figure 3.9b**). Apart from seasonal differences,

vertical motion variations differ significantly from precipitable water, with percentile bins increasing in both seasons.

Finally, we quantify the human-forced change in total moisture flux convergence, as well as thermodynamic and dynamic components based on the moisture budget balance, as shown in **Figure 3.14**. Variations in column-integrated moisture flux convergence, notably for non-MJJAS season, agree well with rainfall changes in terms of daily-mean and 95$^{th}$ percentile daily precipitation (see the first two bars in each panel of **Figure 3.14**). For daily-mean rainfall changes, the thermodynamic effect is the predominant process in both seasons, consistent with previous findings (Seager et al., 2010; Ma et al., 2017); the dynamic effect amplifies rainfall increase and becomes a secondary contributor, especially to non-MJJAS rainfall. While for the 95$^{th}$ percentile extreme precipitation, the dynamic effect tends to be the most important factor for both seasons. A similar dynamic amplification was found for Asian monsoon extreme rainfall (Pfahl et al., 2017; Tandon et al., 2018). In other words, changes in daily-mean rainfall intensity are mainly associated with the thermodynamic component, i.e., increased moisture. Extreme precipitation variations, however, are predominantly controlled by the dynamic effect, for example, those due to changes in wind circulations. In addition, the thermodynamic term exhibits high consistency in case simulations, whereas the dynamic term varies a lot throughout simulations. Large biases in the dynamic component are also found among global climate models, due to their poor performances in reproducing wind circulation (Chou et al., 2012). Thus, the case-to-case area-averaged rainfall variations could be due to the variations in the dynamic component (O'Gorman & Schneider, 2009), especially in the MJJAS season.

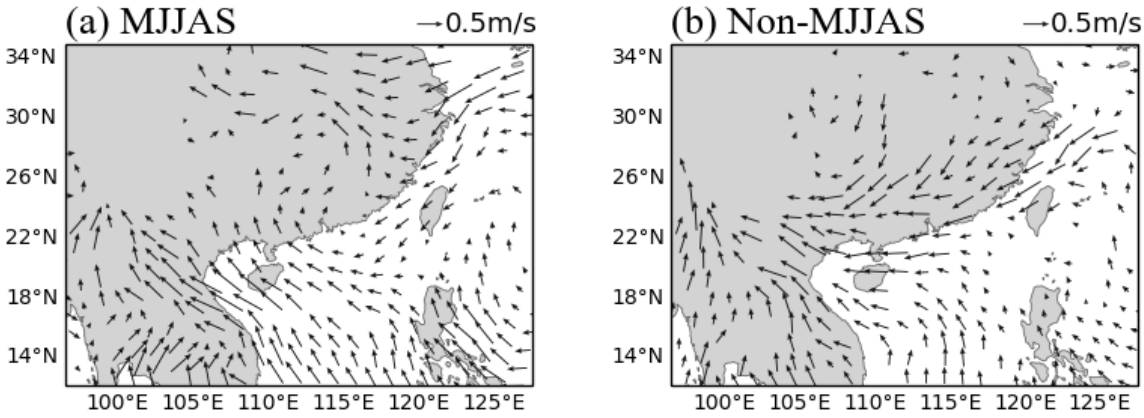


***Figure 3.10*** *Difference (CTL - NAT) in wind fields at 850 hPa (units: m $s^{-1}$, see the scale at the upper right of each panel), averaged from the cases in (a) MJJAS and (b) non-MJJAS seasons. Only wind differences that exceed the 90% significance level are depicted with black arrows.*

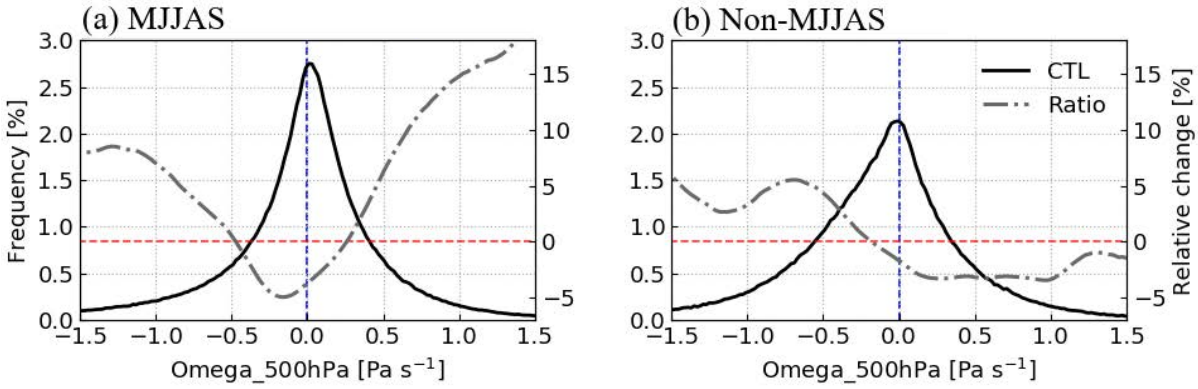


***Figure 3.11*** *PDF of 500-hPa pressure velocity (units: Pa $s^{-1}$) in the CTL (black line) and the relative changes from NAT to CTL (grey dashed line) over PRD, for (a) MJJAS and (b) non-MJJAS seasons.*

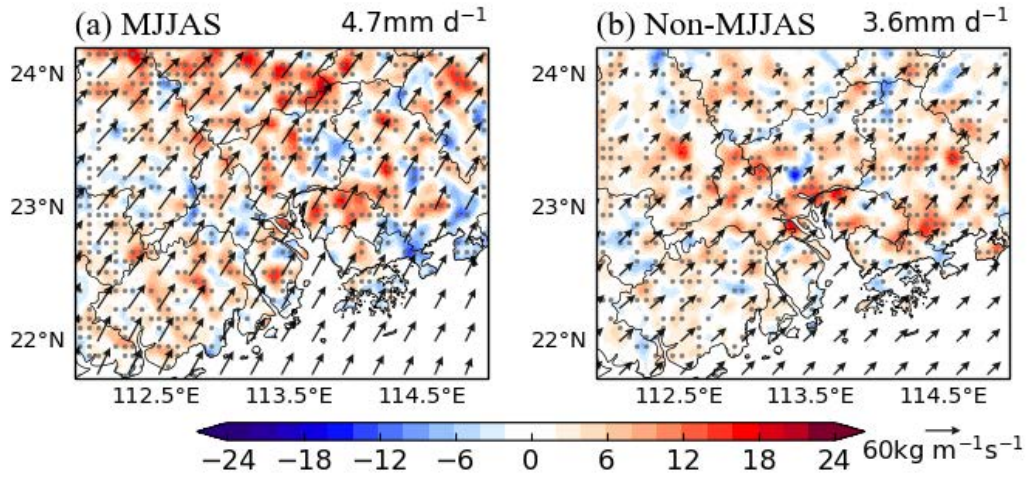


***Figure 3.12*** *Difference (CTL-NAT) in vertically-integrated moisture flux (arrows, units: kg m$^{-1}$ s$^{-1}$; see the scale at the bottom right) and its convergence (shading, units: mm d$^{-1}$; positive corresponds to moisture convergence) over PRD, averaged from the events in (a) MJJAS and (b) non-MJJAS seasons. Grey dots indicate the difference exceeding 90% confidence level. Numbers at the upper-right corner of each panel represent PRD land-averaged values.*

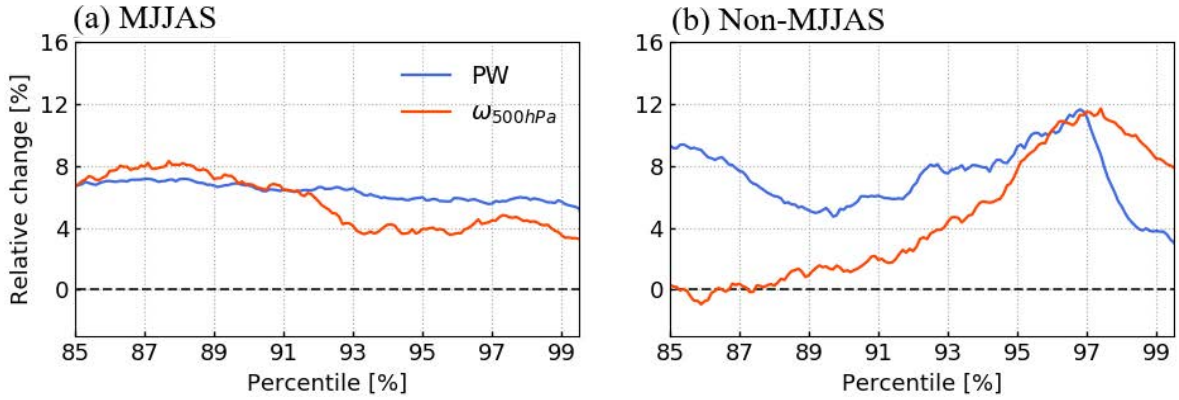


***Figure 3.13*** *Relative change from NAT to CTL of precipitable water (blue line; units: kg m$^{-2}$) and 500-hPa pressure velocity (red line; units: Pa s$^{-1}$), based on data taken from heavy to extreme precipitation occurrence (> 85$^{th}$ percentile of daily rainfall) over PRD for (a) MJJAS and (b) non-MJJAS seasons. Only positive values of pressure velocity are included to represent upward motion change.*

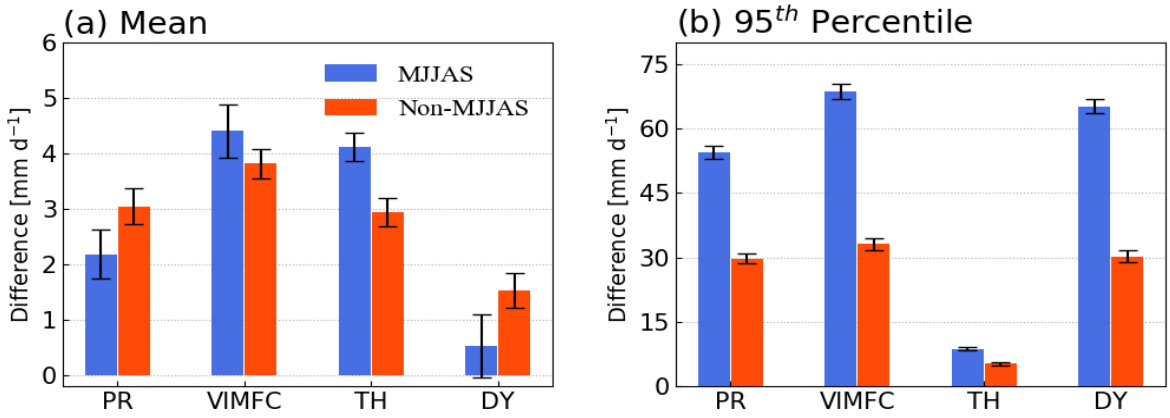


***Figure 3.14*** *Differences (i.e., CTL – NAT; units: mm d$^{-1}$) in daily precipitation (PR), vertically-integrated moisture flux convergence (VIMFC), thermodynamic (TH), and dynamic (DY) contributions for MJJAS (blue bar) and non-MJJAS (red bar) seasons, based on the average of (a) daily-mean rainfall and (b) 95$^{th}$ percentile extreme rainfall over PRD land area. The error bars denote the bias among extreme rainfall cases.*

## 3.4 Brief summary

This chapter elaborates the human-contributed variations in daily-mean and extreme rainfall over the PRD region, based on the WRF simulations of selected 40 extreme rainfall events. To address human influences, the model was forced by the initial and boundary conditions with human forcing (control run, denoted as CTL), and with those in which human forcing was removed (NAT run). Model's capacity to replicate large-scale patterns of synoptic conditions and precipitation was evaluated based on observations. The WRF model reproduces reasonable low-level temperature and thus precipitable water over PRD land, though an underestimation of both is found over SCS when compared to observations. WRF also captured horizontal wind circulation over the target area reasonably well, especially in the upper layers, due to spectral nudging. With the help of the well-simulated wind fields and moisture amounts, the gauge-observed rainband pattern along the South China coastal area is accurately captured. The WRF-simulated rainfall intensity over the inland PRD closely matches in-situ observations, albeit

with coastal rainfall being underpredicted. The simulated frequency of PRD rainfall also compares favorably with observations.

Attributing precipitation changes to human influences is conducted by comparing CTL with NAT simulations. Based on the average of all selected cases, human activities have caused the low-to-mid (1000-500 hPa) troposphere to warm by 0.9 ℃ over the PRD. The near-surface temperature in PRD increases by 0.9-1.1 ℃ in MJJAS, while it climbs by 0.6-0.8 ℃ in non-MJJAS. Under such a human-induced warmer climate, spatial distribution illustrates that daily-mean precipitation increases substantially by 10~70% over inland, while coastal rainfall is inhibited by about 20%. For the 95$^{th}$ percentile extreme rainfall, a similar pattern is found, but with more significant variations. We also found that anthropogenic warming provokes stronger low-level southerly winds over the PRD, which is probably responsible for the greater increase of inland precipitation. Besides the rainfall pattern, precipitation frequency decreases for light to moderate rainfall but increases for heavier rainfall in both seasons. For heavy rain rates at 80~150 mm d$^{-1}$, the increase of frequency reaches 10~30% in MJJAS, with a more noticeable enhancement of 20~40% in non-MJJAS. Nevertheless, very extreme rainfall (> 99$^{th}$ percentile) in MJJAS tends to occur more frequently and become heavier as a result of warming. Moreover, for heavy rainfall (> 85$^{th}$ percentile), the mean rate of increase of precipitation intensity in MJJAS is estimated to be 8-9.5%, which is nearly CC scaling. In contrast, it reaches a super-CC rate of 12.4% at the 96$^{th}$ percentile of the non-MJJAS rainfall, which in turn leads to a stronger vertical temperature gradient due to more latent heat released.

The super-CC increase in non-MJJAS heavy rain results not only from a more robust increase in precipitable water amount, but more importantly from stronger and more persistent upward motion (see also Nie et al., 2018). It is also associated with changes in large-scale wind circulation, that is, the enhanced northward winds over PRD in MJJAS whereas strengthened wind convergence over the coast of South China in non-MJJAS. Last but not least, moisture

budget analysis reveals that the increase in daily-mean precipitation is primarily contributed by thermodynamic changes in both seasons, with dynamic changes being of secondary importance for non-MJJAS rainfall. While dynamic components contribute most to the 95$^{th}$ percentile precipitation. The indispensable dynamic feedback on PRD extreme rainfall in non-MJJAS will be further explored in Chapter 4 by studying a wintertime rainstorm.

# Chapter 4 Attributing a wintertime extreme rainfall event to anthropogenic influences

In Chapter 3, attribution of extreme precipitation characteristics to anthropogenic influences was carried out based on WRF simulations of multiple extreme cases. The findings suggest that extreme rainfall response to human impacts varies seasonally. Notably, the increase in heavy to extreme precipitation ($85^{th}$-$99^{th}$ percentiles) during the non-MJJAS season peaks at 12.4%, implying a super-CC scaling. This super-CC increase highlights the importance of dynamic contributions to non-MJJAS rainfall increase, in addition to thermodynamic influence.

To further explore such human-induced dynamic and thermodynamic effects on non-MJJAS extreme rainfall, we carried out an additional attribution analysis on a record-breaking rainfall event in boreal winter 2013.

## 4.1 Meteorological overview

In December 2013, a rare flooding disaster struck Hainan Province in South China, causing enormous damages to the local infrastructure. Heavy rainfall affected the Guangdong Province during December 14-17 and contributed to the largest 4-day cumulative rainfall with more than 100 mm $d^{-1}$ averaged over the entire PRD for winter (i.e., November-December-January) of 1998-2018 (see the red dot in **Figure 4.1**). The monthly total precipitation averaged over Hong Kong SAR was the tenth highest for December since 1884 (source: https://www.hko.gov.hk/en/wxinfo/pastwx/ywx2013.htm).

To examine the synoptic conditions of this heavy rainfall, we provided composite maps of wind circulation, wind divergence, and geopotential height at different pressure levels (see **Figure 4.2**). In the upper troposphere (see **Figure 4.2a**), there was an intense westerly jet from North

Africa to Southeast Asia and the North Pacific. Disturbances within such a Rossby waveguide were found to be responsible for the initiation of this event (W. Huang et al., 2019; Chun Li & Sun, 2015). The strongest 250-hPa wind divergence is found over SC. In the middle troposphere (see **Figure 4.2b**), a deep low was located over the northwest of Russia, accompanied by the strongest northerly winds that brought plenty of cold air down to mid-latitudes. A ridge lying over the northeastern Tibet Plateau and a trough over the western Indochinese Peninsula further facilitated the southward transportation of cold and dry air (see contours in **Figure 4.2b**). Warm moist air was transported northward by a southwesterly branch of the subtropical high over the western Pacific to feed rain-bearing systems (see vectors in **Figure 4.2b**). The two airflows converged in SC, accompanied by a noticeable ascend in the mid troposphere. We also noted that the mid-level upward motion was coupled with wind divergence in the upper layer (see shading in **Figures 4.2a, b**). In the lower troposphere (see **Figure 4.2c**), the subtropical high persisted over the western Pacific, transporting warm moist air mainly from SCS to SC (W. Huang et al., 2018). Meanwhile, cold dry air moved southward by northerly and northeasterly winds. Wind convergence occurs when the warm and cold airflows collided. The low-level convergence coupled with the upper-level divergence promoted strong atmospheric convection that triggered heavy precipitation (see shading in **Figure 4.2c**). During this event, the cold and dry air invaded the PRD region on December 15, causing a sudden drop in dewpoint temperature of around 10 ℃ by December 17 (see blue line in **Figure 4.3**). According to HKO records, the surface temperature reached the annual minimum temperature of 9.2 ℃ on December 18.

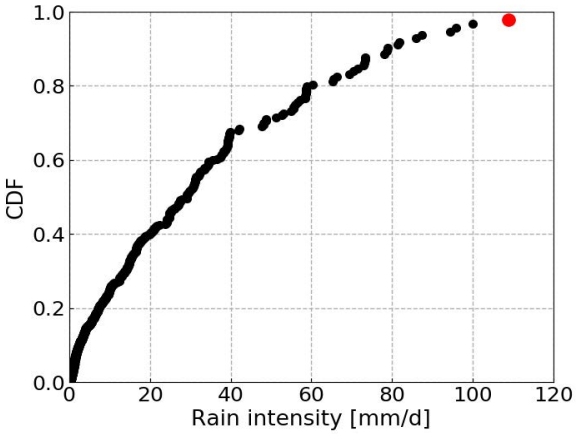


***Figure 4.1*** *Cumulative distribution function (CDF) distribution of four-day cumulative rainfall (units: mm* $d^{-1}$*) during wintertime over the PRD region from 1998 to 2018, based on TRMM 3B42 observations. The red dot denotes the extreme rainfall event that occurred during December 14-17, 2013.*

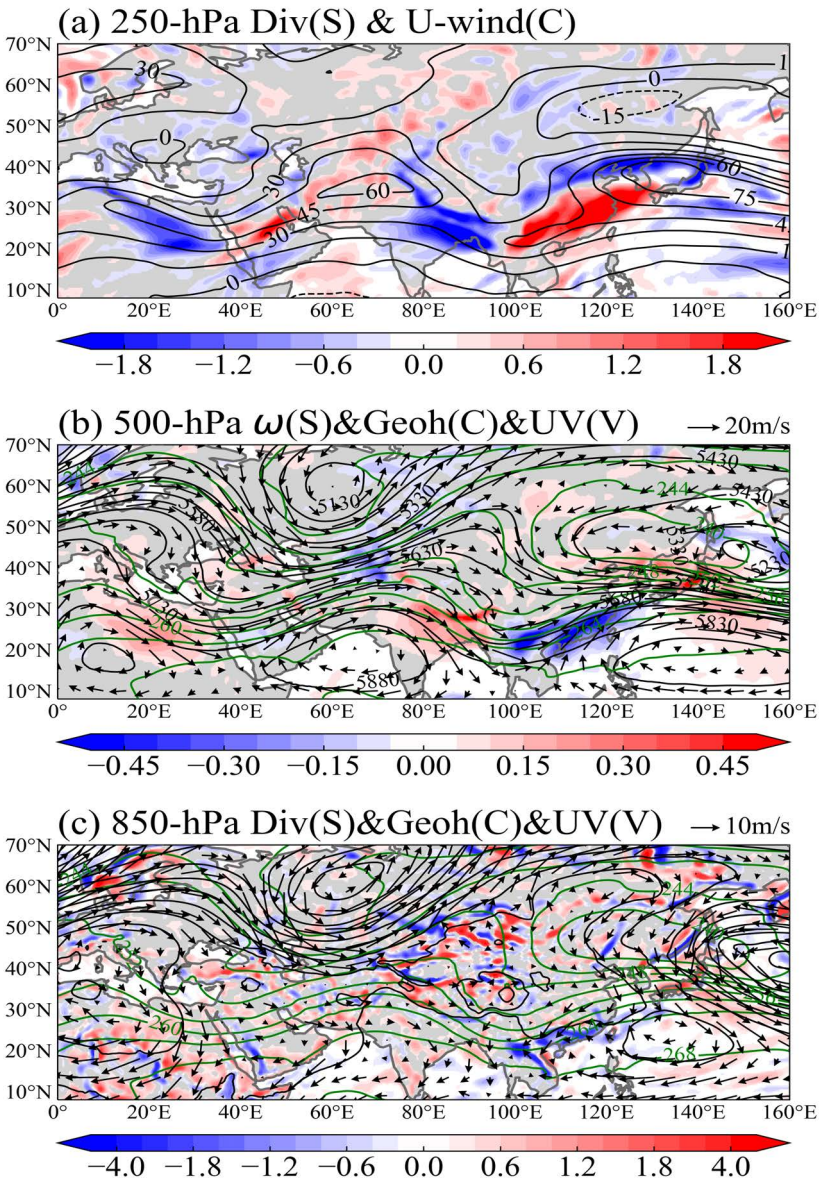


***Figure 4.2*** *Composite patterns: (a) 250-hPa wind divergence (shading, units: $10^{-5}$ $s^{-1}$) and zonal wind (contours, units: m $s^{-1}$), (b) 500-hPa pressure velocity (shading, units: Pa $s^{-1}$), geopotential height (black contours, units: m), temperature (green contours, units: K) and horizontal winds (vectors; see the scale at top right in units of m $s^{-1}$), (c) 850-hPa wind divergence (shading), geopotential height (black contours), temperature (green contours) and horizontal winds (vectors; see the scale at top right in units of m $s^{-1}$) averaged for December 14-17, based on ERA-Interim data.*

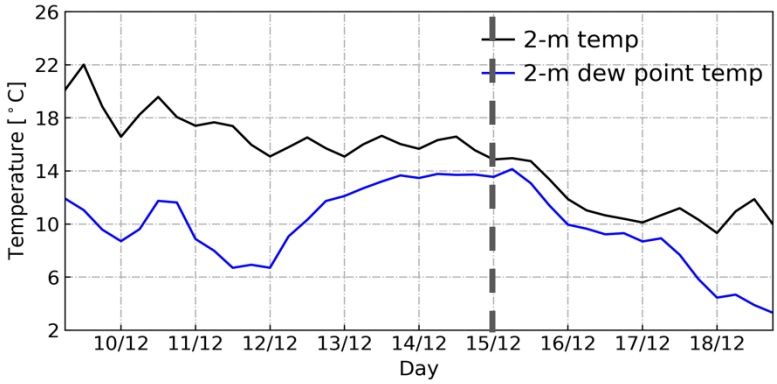


***Figure 4.3*** *Time evolution of 6-hourly air temperature (black, units: ℃) and 2-m dewpoint temperature (blue, units: ℃) averaged over the PRD region from December 9 to 18, based on ERA-Interim data.*

## 4.2 Model evaluation

### 4.2.1 Rainfall evaluation

The WRF model's performance in reproducing the synoptic variables, such as specific humidity, horizontal wind components, and pressure velocity, during this extreme rainfall process are assessed based on ERA-Interim data (see **Figure 4.4**). The model successfully captured the evolution of specific humidity, with maximum values of ~10 g $kg^{-1}$ distributed below 800 hPa from December 14 to 15 (see **Figure 4.4a, b**). However, there is an underprediction of humidity prior to the onset of rainfall but an overestimation on December 16. The simulated wind evolution, especially for the zonal wind, is in good agreement with observations (see **Figure 4.4c, d, e, f**). Compared with ERA-Interim, the model reproduced weaker mid-to-upper-level (above 600 hPa) southerly winds (positive), and low-level (below 700 hPa) northerly winds (negative) over PRD during the precipitation period from December 14 to 17. For pressure velocity, the observed main ascend (negative) centers on December 15 and 16 were well simulated, although the model gave a slightly stronger low-level (below 800 hPa) ascending motion during the rainfall period (see **Figure 4.4g, h**).

We also evaluated the model-simulated precipitation using satellite- and rain gauge-based observations. **Figure 4.5** presents daily precipitation averaged from December 14 to 17 over SC, obtained from the WRF control runs (CTL) using different physics schemes, and TRMM 3B42 product and gauge-based CPC observations. In general, the ensemble mean of the CTL simulations agrees better with TRMM 3B42 than CPC data. Furthermore, it is noted that the ensemble mean performs better than simulations with individual schemes by comparing to observations, in terms of both pattern and intensity of the rainband. In particular, the WG3 and WKF schemes overestimate the observed rainfall intensity, whereas TBMJ is comparable to CPC observations but less than TRMM-observed rainfall. However, the simulated rainband is shifted to the northwest by 110 km, compared with the observed rainband, although it still covers our study area. Despite the fact that the ensemble mean simulations and TRMM 3B42 data appear to be stronger than the CPC-observed rain rates, the model has a good capability of capturing the precipitation patterns. Previous studies concluded that the CPC dataset tends to smooth out the precipitation structure and underestimates rainfall intensity over Mainland China (Shen & Xiong, 2016).

Besides the spatial patterns, it is noteworthy that the WRF-simulated time evolution of daily precipitation in PRD matches closely both the observations (see **Figure 4.6**). The model gives maximum rainfall on December 15 and 16 more than 40 mm $d^{-1}$, with a slight underestimation of mean rainfall when compared with CPC data (see numbers in brackets in **Figure 4.6**). Overall, WRF can well simulate the precipitation pattern and evolution, as well as the associated atmospheric fields of this event.

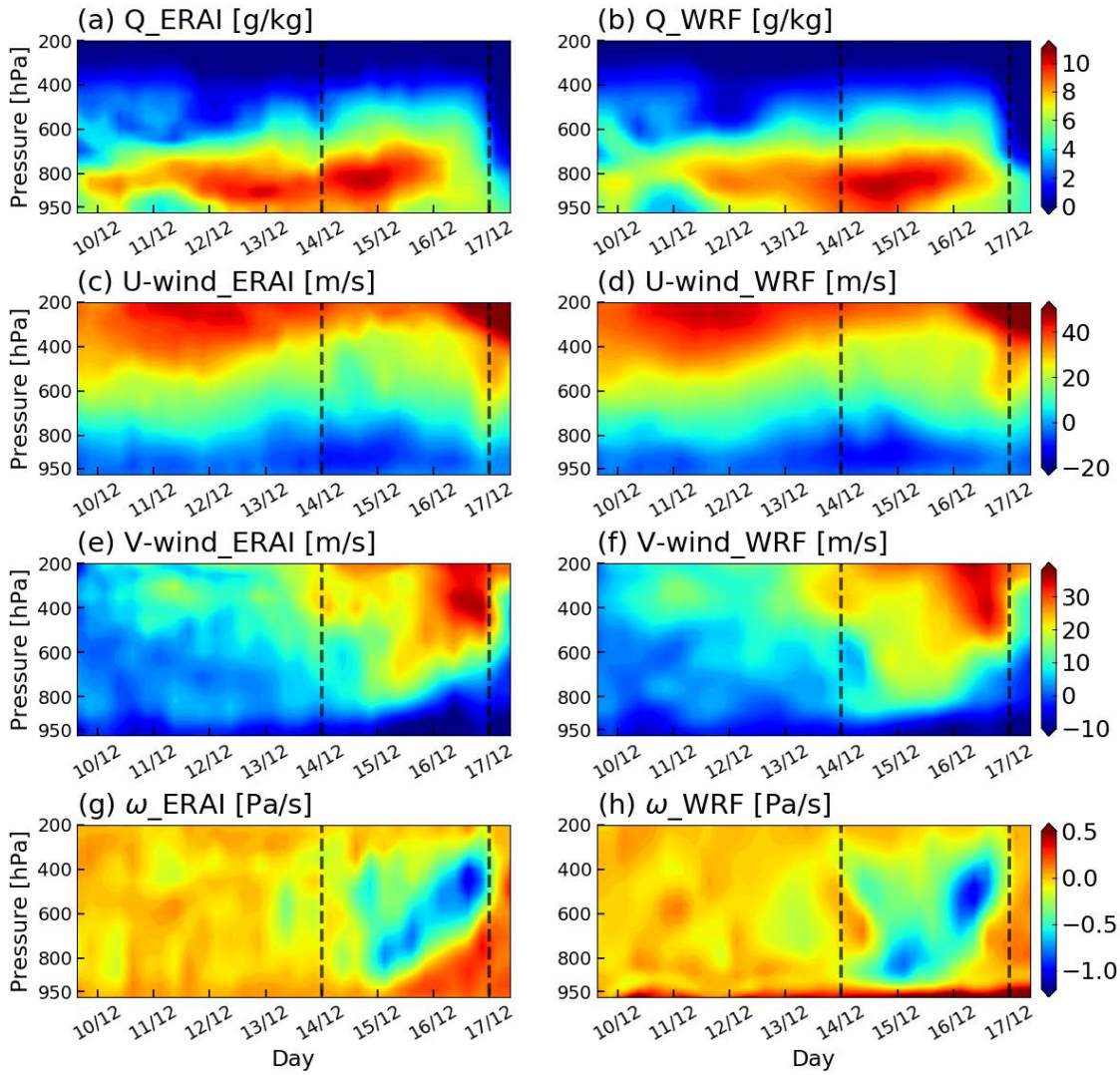


***Figure 4.4*** *Comparison of time evolution of (a, b) 6-hourly specific humidity (units: g kg$^{-1}$), (c, d) U-wind (units: m s$^{-1}$), (e, f) V-wind component (units: m s$^{-1}$), and (g, h) pressure velocity (units: Pa s$^{-1}$) averaged over the PRD region from ERA-Interim (left column) and WRF control run (right column). The rainfall period is marked by the black dashed lines.*

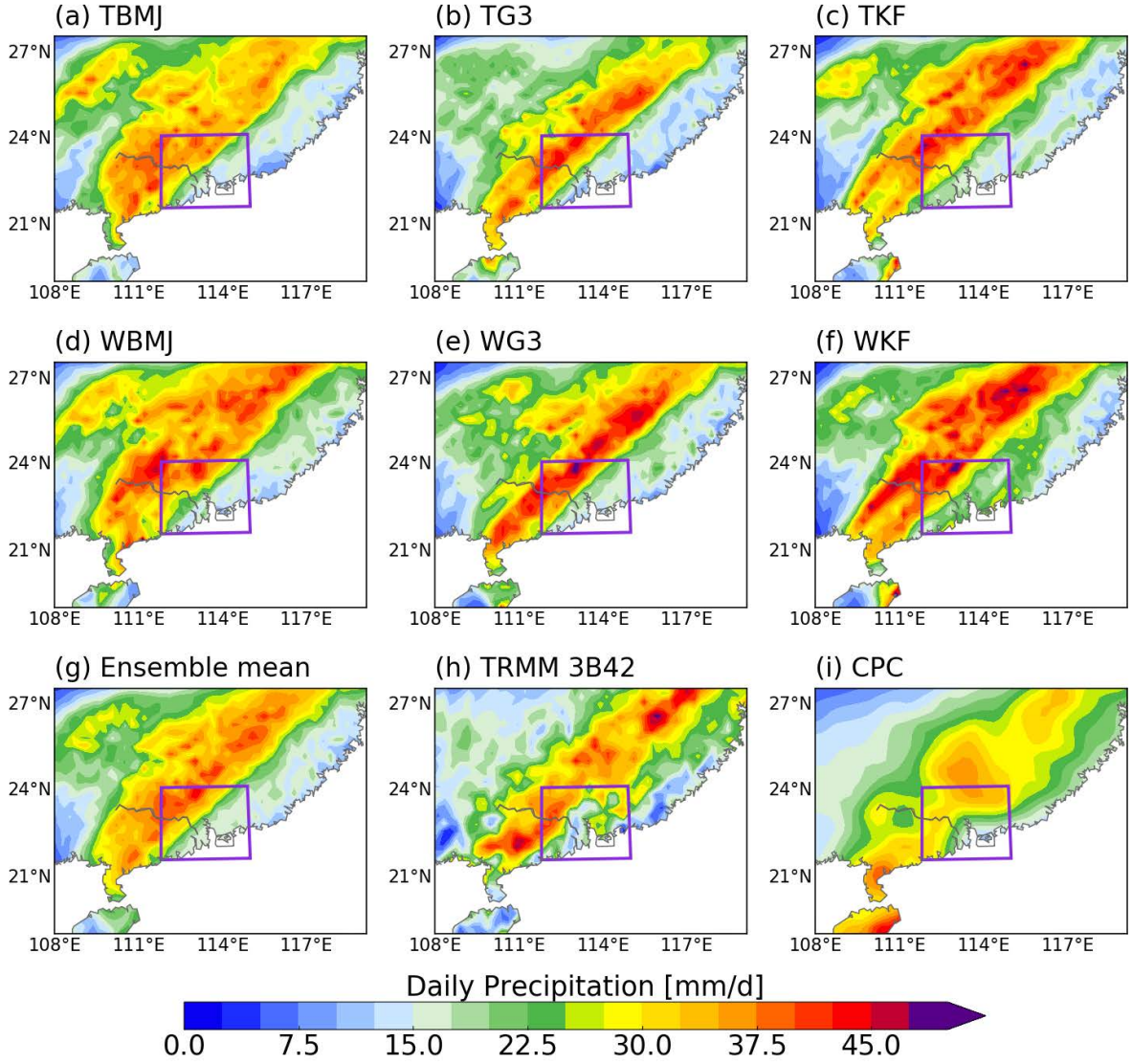


***Figure 4.5*** *Daily mean precipitation (units: mm $d^{-1}$) between December 14 and 17 over South China, obtained from the WRF control runs using (a) Thompson-BMJ, (b) Thompson-Grell 3D, (c) Thompson-KF, (d) WSM6-BMJ, (e) WSM6-Grell 3D, (f) WSM6-KF schemes and (g) the ensemble mean of the multi-physics members, as well as from (h) TRMM 3B42 product, and (i) gauge-based CPC observations. The purple box in each panel outlines the PRD region.*

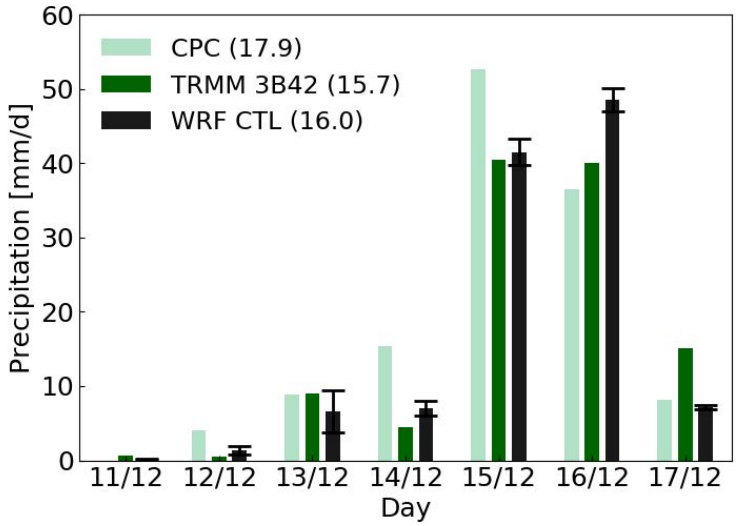


***Figure 4.6*** *Time evolution of daily precipitation over the PRD, obtained from rain gauge-based CPC observations (light green), satellite-based TRMM 3B42 product (dark green), and WRF CTL simulations (black). Error bars indicate the standard deviation among the six ensemble members with different physics schemes. Numbers in brackets are the 4-day mean precipitation between December 14 and 17.*

### 4.2.2 Comparison of WRF-simulated human forcing with CMIP5 projections

Furthermore, we have evaluated the WRF's ability to replicate anthropogenic forcing over the outermost domain projected by CMIP5 GCMs. We see from CMIP5 projections (left panels in **Figure 4.7)** that human activities have caused temperatures in December to rise from ~1 K near the surface to around 2 K at upper levels (above 300 hPa); the low-latitudes tend to have a greater vertical temperature gradient of troposphere than the mid-latitudes (see **Figure 4.7a**). The specific humidity increased with warming, reaching the largest increase of approximately 0.8 g $kg^{-1}$ in the low-level tropics (see **Figure 4.7c**). These anomalies are consistent with the changes under $CO_2$ warming from 33 CMIP5 model mean (see Fig. S8 in Laua & Kim, 2015). The wind fields in December show stronger upper-level (above 300 hPa) westerlies due to the increased temperature gradients, while weaker zonal winds are found below 300 hPa,

particularly at mid-latitudes of 20-30°N (see **Figure 4.7e**); meridional winds are strengthened as a result of anthropogenic influences (see **Figure 4.7g**). These human-forced temperature and humidity anomalies were removed from variables in IBCs in the WRF DTQ experiments, and anomalous wind circulations were removed in DTQW. Differences between the control and two perturbed runs represent the WRF-simulated human forcing. By comparing with CMIP5 ensemble, the WRF model reproduced temperature and humidity anomalies reasonably well (see **Figures 4.7b, d**); the vertical profiles of horizontal wind anomalies were also replicated in general (see **Figures 4.7f, h**), albeit with stronger westerlies and meridional winds in mid-latitudes (30°N-34°N).

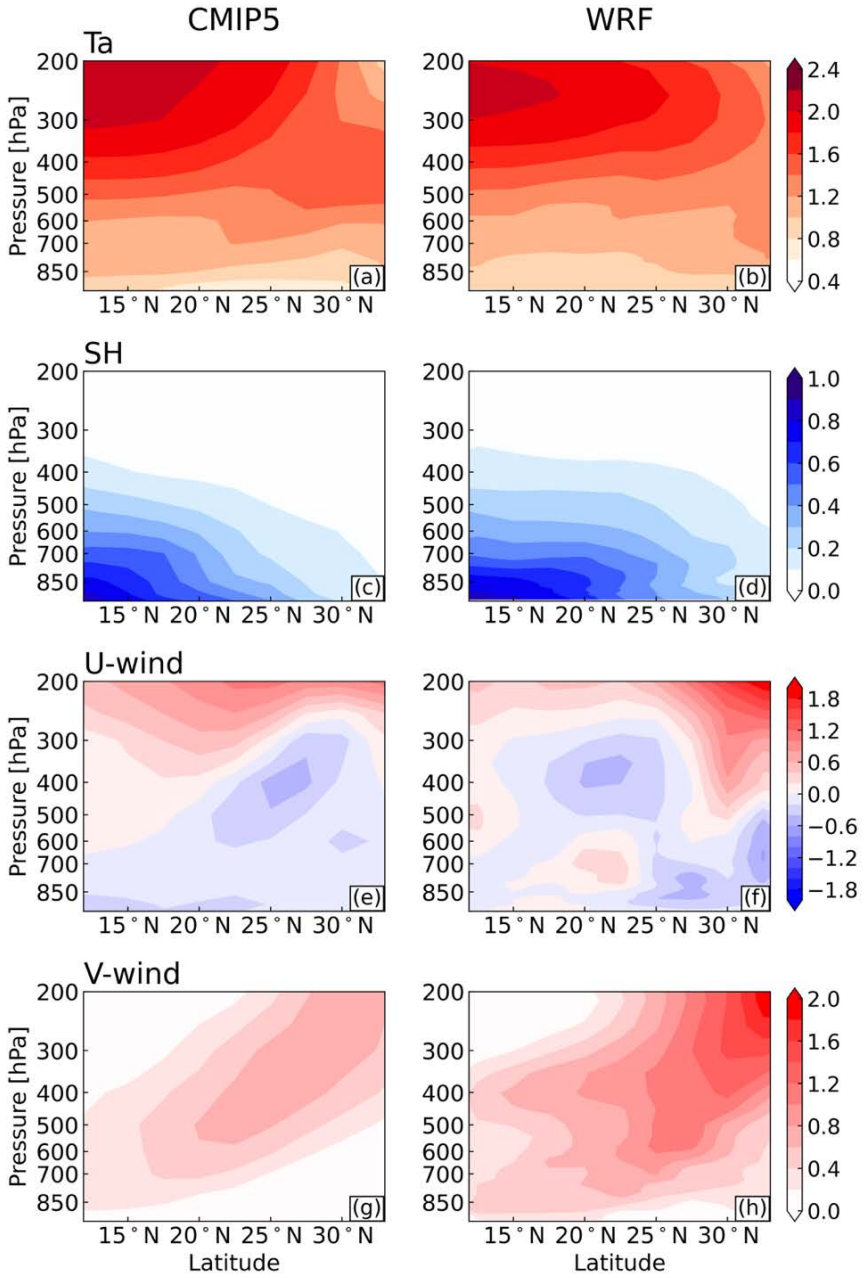


***Figure 4.7*** *Latitude-height cross section of human-forced anomalies for (a, b) air temperature (units: K), (c, d) specific humidity (units: g kg$^{-1}$), (e, f) zonal wind (units: m s$^{-1}$), and (g, h) meridional wind (units: m s$^{-1}$) averaged between 97-127°E (outermost domain of WRF). The left panels are derived from the mean difference in December of 1986-2005 between historical and historicalNat runs from CMIP5 seven-model ensemble (see also Chapters 2.4.2 and 2.4.3 for more details). The right panels are the difference between WRF control and perturbed runs averaged over this case period. See text for details.*

## 4.3 Rainfall responses to anthropogenic forcing

The sensitivity of precipitation to anthropogenic forcing depicted in **Figure 4.7** is now examined by comparing rainfall from the control with that from counterfactual experiments. We first focus on the spatial distribution of the 4-day mean precipitation during the period of December 14 to 17, from CTL and two perturbed simulations (see **Figure 4.8**), based on their 6-member ensemble mean. CTL shows that rainfall mainly occurred over the northwestern areas (known as Qingyuan and Zhaoqing city), accompanied by strong low-level southeasterly winds that facilitate moisture transport from SCS to inland PRD (see **Figure 4.8a**). The maximum rainfall in CTL can reach 45 mm $d^{-1}$, which was reduced by 7-10% in DTQ and 13-15% in DTQW (see **Figures 4.8d, e**), associated with at least 1 K near-surface temperature difference (see **Figure 4.7b**). The results indicate the consistency with CC relation, i.e., around 7% moisture increase per degree of warming (Allen & Ingram, 2002; Viatcheslav V. Kharin et al., 2007; Trenberth et al., 2003). Precipitation over the coastal PRD was also suppressed in two perturbed runs, showing a minor reduction of less than 5% in DTQ and a 7-14% decrease in DTQW; the larger reduction in DTQW mainly occurred over the cities of Zhongshan and Zhuhai. On the contrary, precipitation in between rainfall centers and coastal areas was somehow intensified by no more than 3% in DTQ and DTQW runs. However, the precipitation intensification in DTQW does not pass the 90% significance level. Overall, the daily mean precipitation in PRD tends to be more intense under such a human-induced warming environment. Furthermore, CTL-DTQW shows a larger increase in rainfall intensity than CTL-DTQ, accompanied by the anomalous southerly winds that can deliver more abundant moisture to the rainfall locations (see vectors in **Figure 4.8e**).

Here we also assess the time series of PRD daily rainfall from the control and counterfactual runs (see **Figure 4.9**). Compared to the CTL run, daily rain rates decrease in two perturbed runs on each day of the rainfall period. These reductions are apparently larger than the typical

reductions within ensemble members. It is clear that the daily rainfall was intensified as a result of human-induced warmer and wetter climate; the rainfall could become even stronger due to human-induced wind circulation changes in addition to thermodynamic changes.

To quantify such precipitation variations that are attributable to anthropogenic influences, we calculated the rate of change in daily rainfall with near-surface temperature for each model grid over PRD. The frequency or probability distribution of these grided rates during the rainfall period is given in **Figure 4.10**. Here the change for, say DTQ (red line in **Figure 4.10**), was computed from the relative change in rainfall, i.e., (CTL-DTQ)/DTQ, dividing by the 2-m temperature difference of CTL-DTQ. The same computation was done for the DTQW run. Unanimously in the perturbed runs, the frequencies of rain rates peak at 10% $K^{-1}$, which exceeds the CC scaling of 7% $K^{-1}$. We also found that the probability exhibits a bimodal distribution in DTQW, with a secondary peak at around 36% $K^{-1}$.

We further quantified the 4-day mean and extreme precipitation changes by computing the ratio of rainfall in CTL relative to DTQ and DTQW separately, as shown in the box and whisker diagram (see **Figure 4.11**). Based on the mean, the change in four-day average rainfall intensity in CTL was a 1.11 (11%) increase compared to DTQ with an interquartile range from 8% to 14%, and a 17% increase relative to DTQW with a range of 15-20%. For changes in extreme rainfall, i.e., $95^{th}$ and $99^{th}$ percentiles, it shows a 13% increase relative to DTQ with a spread of 10-17%, and 19% and 21% increases for $95^{th}$ and $99^{th}$ percentiles compared to DTQW, with wider interquartile ranges of 10-18% and 10-32%, respectively. In other words, human-forced thermodynamic changes contributed to at least 11% rainfall increases, whereas human-forced thermodynamic and dynamic changes can result in a larger increment of both mean and extreme precipitation during this event. On average, extreme rainfall increase is more robust than the daily mean, regardless of anthropogenic forcing, which is consistent with previous studies (Alexander et al., 2006; Myhre et al., 2019). Besides, the ratio of CTL to DTQW shows

a large increase in the 99$^{th}$ percentile than the 95$^{th}$ percentile rainfall, suggesting that human-caused dynamic anomalies could intensify very extreme rainfall even further. It was also noteworthy that variations in these extremes can reach or even exceed the CC scaling; a similar super-CC behavior was reported for hourly rainfall changes (Lenderink et al., 2011; Westra et al., 2014). Such additional intensification in both the daily mean and extreme precipitation suggests the important role played by the dynamic effect (Nie et al., 2018).

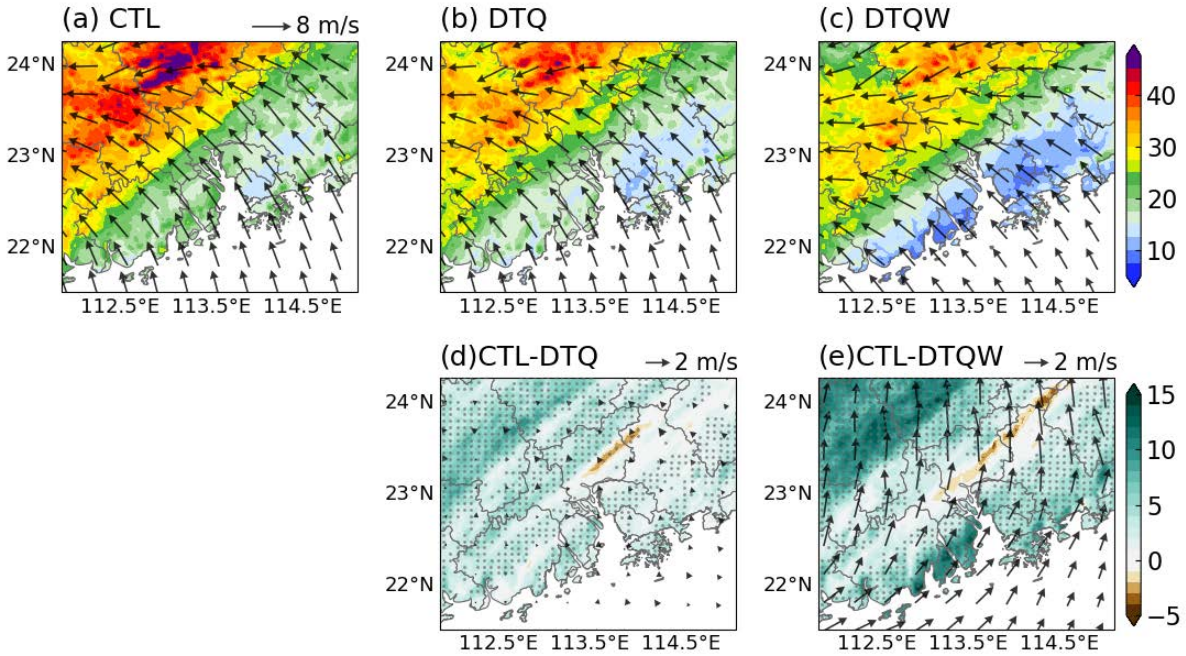


***Figure 4.8*** *Daily precipitation (shading, units: mm d$^{-1}$) overlapped with the 850-hPa horizontal winds (vectors, units: m s$^{-1}$), averaged from December 14 to 17 over the PRD, from the (a) CTL, (b) DTQ, and (c) DTQW runs, as well as differences between (d) CTL and DTQ, (e) CTL and DTQW, relative to DTQ and DTQW, respectively. The significant relative changes in rain intensity at the 90% confidence level are marked by grey dots.*

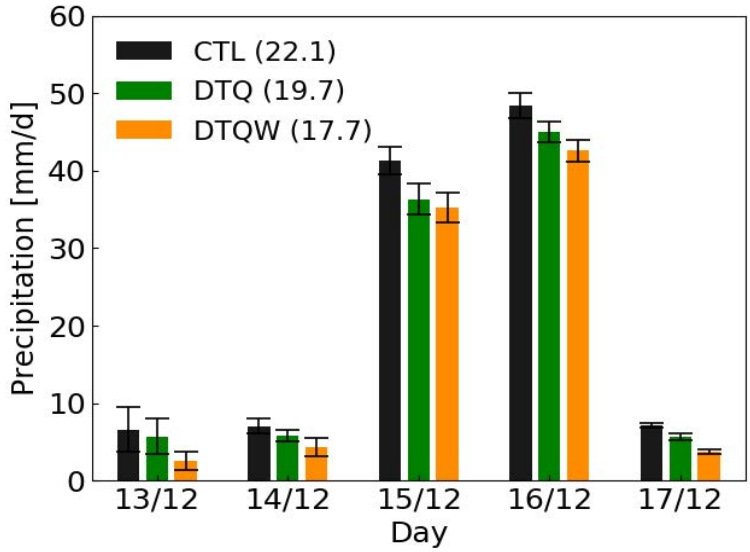


***Figure 4.9*** *Time evolution of daily precipitation in the WRF CTL (black bars), DTQ (green bars), and DTQW (orange bars) averaged over PRD. Error bars denote the standard deviation among six ensemble members with different physics schemes.*

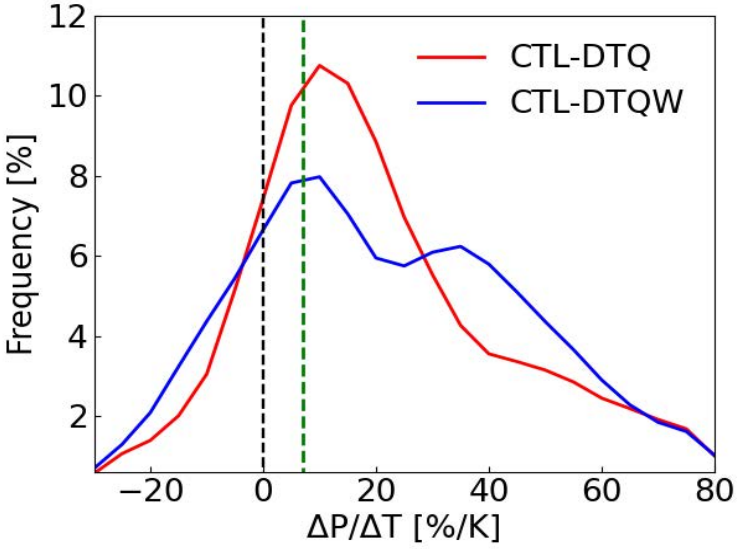


***Figure 4.10*** *Frequency distribution of percentage changes in the daily precipitation per degree of 2-m temperature increases on each model grid over the PRD for December 14-17, from CTL relative to DTQ (red) and DTQW (blue). The green dashed line indicates the CC scaling of 7% $K^{-1}$.*

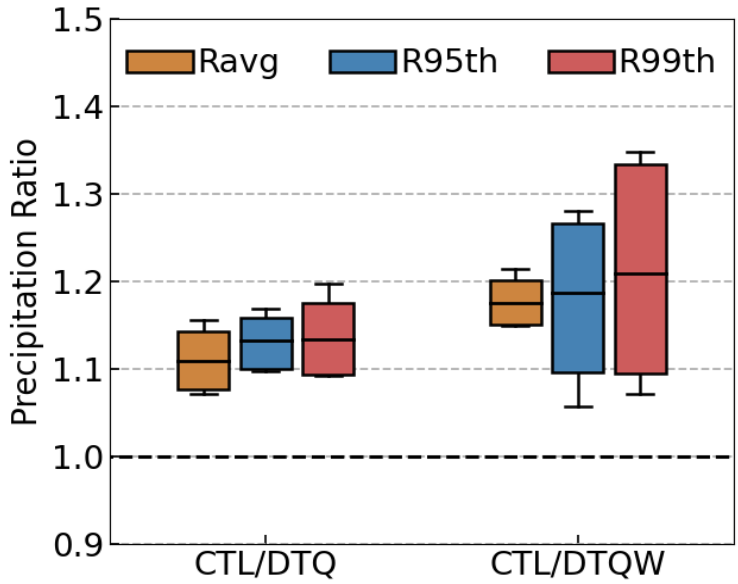


***Figure 4.11*** *Box and whisker plot of ratios of the simulated 4-day mean (brown bars), 95$^{th}$ (blue bars) and 99$^{th}$ percentile (red bars) of daily precipitation (units: mm d$^{-1}$) averaged over December 14-17 in PRD, in the CTL run relative to the DTQ and DTQW runs.*

## 4.4 Underlying mechanisms

### 4.4.1 Large-scale circulation changes

As previously stated, changes in extreme precipitation caused by human forcing are not only determined by moisture-related thermodynamic effects, but also by dynamic effects associated with wind circulation change. We first examine human influences on the large-scale distribution of temperature and geopotential height, as well as horizontal wind patterns at different pressure levels. In the low-level (850 hPa) troposphere (**Figure 4.12**), CTL-DTQ warming overall tends to be stronger across mainland China than SCS and adjacent continents (see **Figure 4.12b**). The thermal contrast is accompanied by southerly and southwesterly wind anomalies over coastal areas of SC (see vectors in **Figure 4.12f**). Meanwhile, the warmer air over central than northern areas of SC induced anomalous northerly winds, implying a strengthened winter monsoon circulation under human-induced warming in this event. These

two airflows converged into an anomalous low-pressure system over southern China (see shading in **Figure 4.12f**), resulting in a strengthened low-level wind convergence (see vectors in **Figure 4.12f**). Besides, CTL-DTQW shows the highest warming over PRD inland, which is likely related to urbanization effects, and supports anomalous southerlies (see **Figure 4.12c**). In the mid-level (500 hPa) troposphere, accompanied by anomalous southerly winds (see vectors in **Figure 4.13f**), temperature anomaly in CTL-DTQW shows faster warming over land than over ocean, with the largest increment over central SC (see **Figure 4.13c**). Such anomalous temperature gradients, however, were not seen in CTL-DTQ that has a relatively uniform warming pattern, especially over the PRD (see **Figure 4.13b**). The low-level anthropogenic warming also results in higher geopotential at 500 hPa in CTL, with a larger increase over SC when compared to DTQW than DTQ (see shading in **Figures 4.13e, f**); this gives rise to anomalous anticyclonic winds over ESC in CTL-DTQW. Unlike the low-level warming, the upper-level (250 hPa) temperature in CTL increases more robust over the low-latitudes (south of 19°N) than subtropics, compared to DTQ (see **Figure 4.14b**), which can also be seen in **Figures 4.7a, b** and Fig. S8 in Laua & Kim (2015). In contrast, CTL-DTQW has no distinct warming gradient (see **Figure 4.14c**); it also shows the anomalous high pressure over SC with stronger southerlies (see **Figure 4.14f**), consistent with temperature changes below 250 hPa.

Changes in wind divergences at 250 hPa and 850 hPa are also examined and presented in **Figure 4.15**. CTL patterns indicate that the low-level wind convergence center covers the PRD region and upper-level divergence appears over the SC, suggesting strong vertical convection (**Figures 4.15a, d**). Such low-level wind convergences over the PRD were greatly intensified compared to DTQW due to human influences (see **Figure 4.15f**). On the other hand, human activities have little impact on the upper-level convergence over PRD but intensified the convergence north of PRD (**Figure 4.15c**), which is related to wind changes (**Figure 4.14f**). In

contrast, CTL-DTQ shows a much smaller difference (see **Figures 4.14b, e**), for no horizontal wind anomalies involved in DTQ.

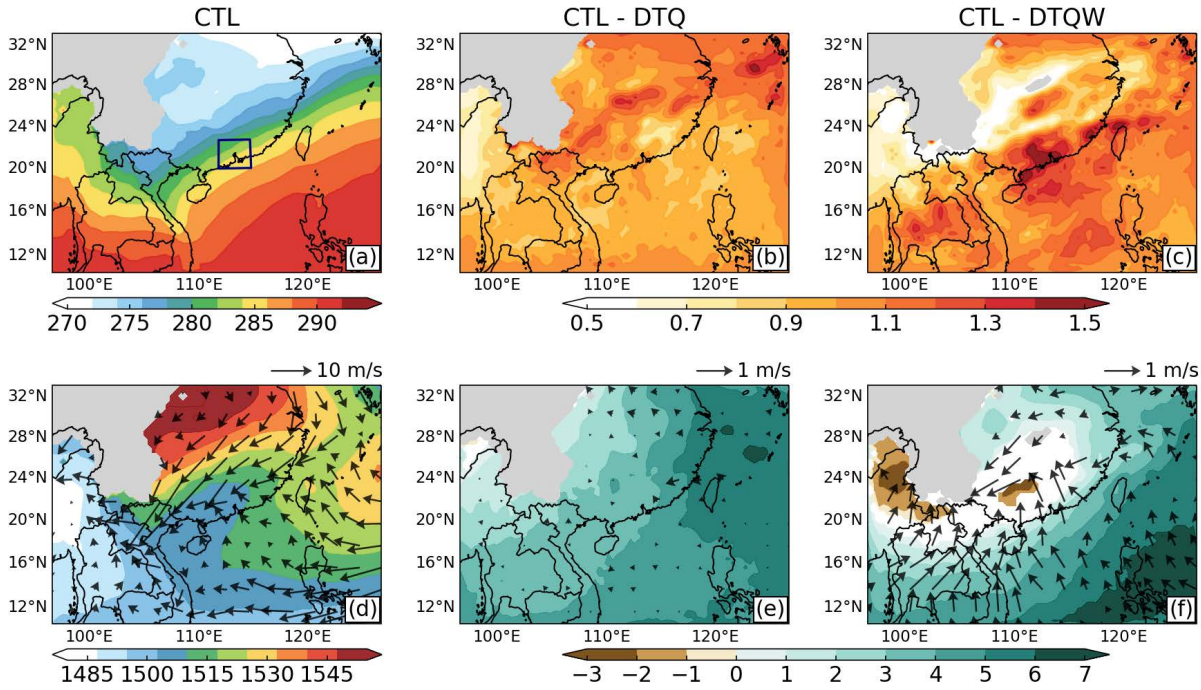


***Figure 4.12*** *Composite map of (a, b, c) the 850-hPa temperature (shading, units: K) and (d, e, f) geopotential height (shading, units: m) overlapped with horizontal winds at 850 hPa (vectors; see scale arrow at top right in units of m* $s^{-1}$*), averaged from Dec 14 to 17 over the outermost domain, in the (a, d) CTL runs, as well as their differences between (b, e) CTL and DTQ, (c, f) CTL and DTQW that passed the 90% confidence level. Missing values over Tibetan Plateau are masked by grey shading. The dark box in figure (a) outlines the PRD region.*

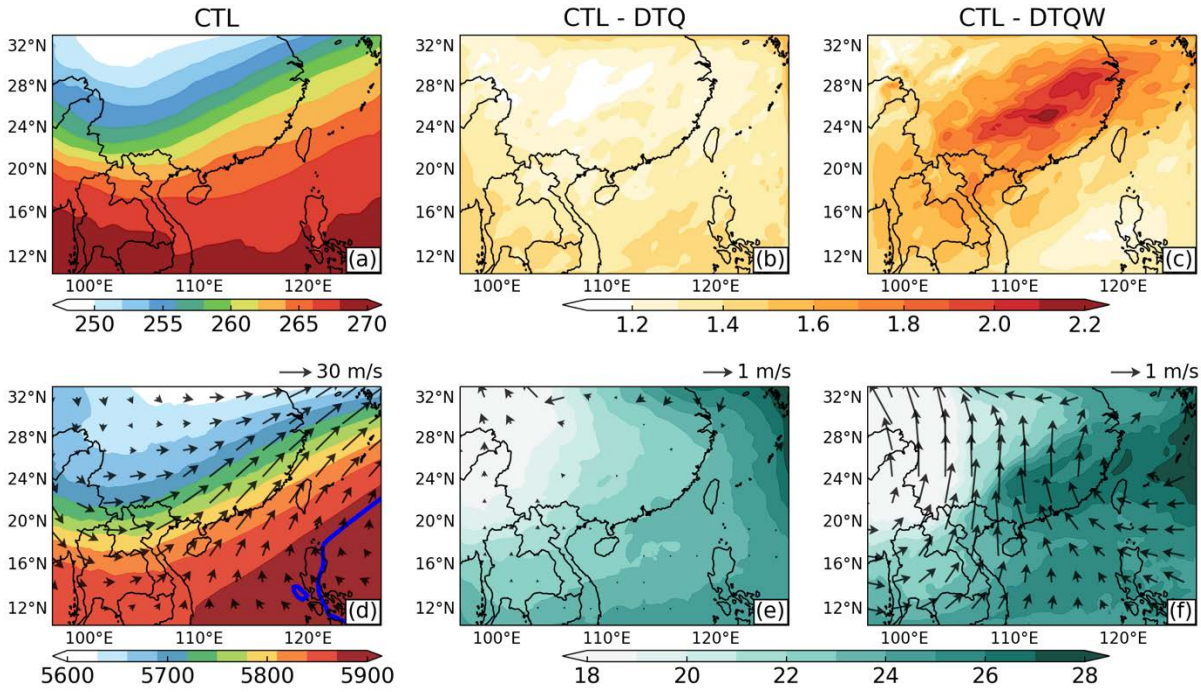


***Figure 4.13*** *Same as* ***Figure 4.12****, but for variables at 500 hPa. Blue thick line denotes 5880-m geopotential height contour.*

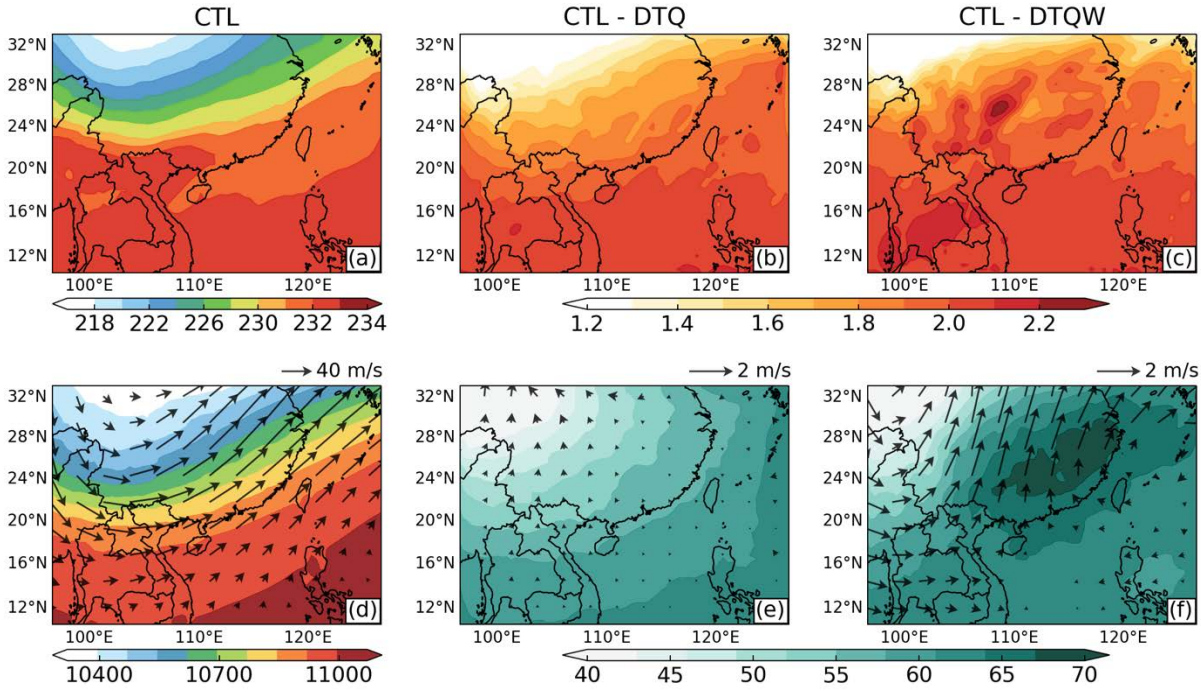


***Figure 4.14*** *Same as* ***Figure 4.12****, but for variables at 250 hPa.*

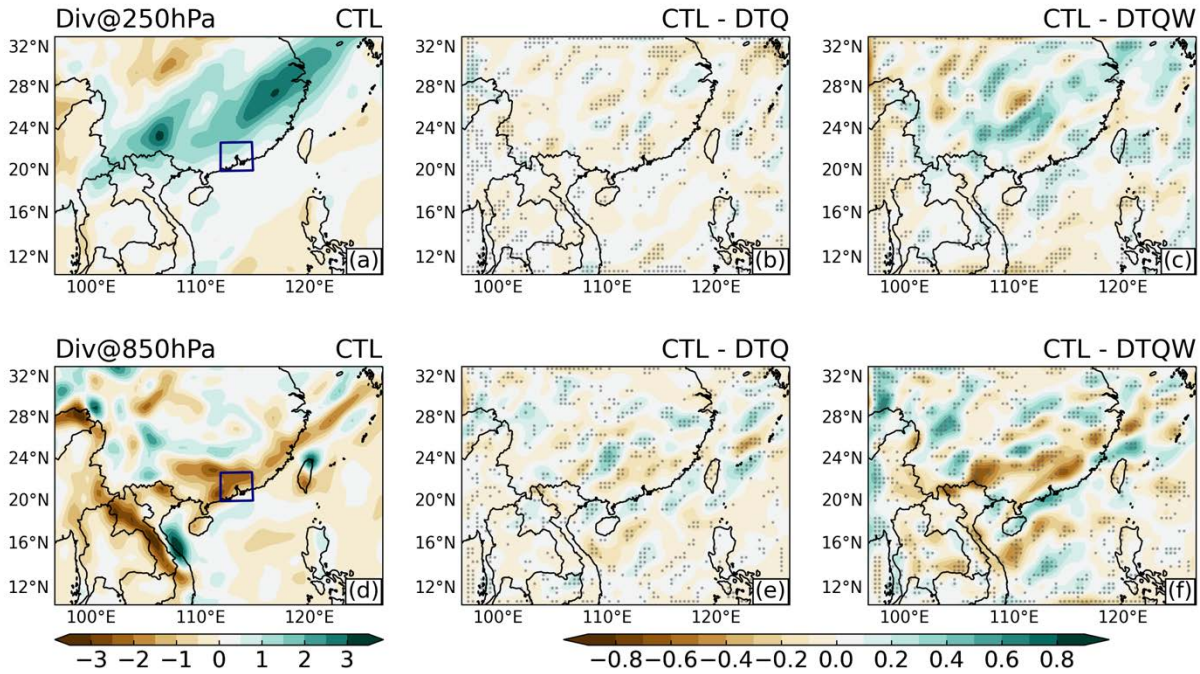


***Figure 4.15*** *Composites of divergences (shading, units: $10^{-5}$ $s^{-1}$) at (a, b, c) 250 hPa and (d, e, f) 850 hPa averaged over Dec 14-17 in the (a, d) CTL runs, and differences between (b, e) CTL and DTQ, (c, f) CTL and DTQW. Grey dots mark divergence differences at the 90% confidence level. Dark boxes outline the PRD region.*

### 4.4.2 Thermodynamic versus dynamic contributions

We next inspect the PRD regional-scale responses of thermodynamic and dynamic processes to human forcing. To probe the anomalous thermodynamic processes involved, we examine the evolution of temperature and specific humidity changes as given in **Figure 4.16**. The difference between CTL and DTQ indicates that human activities have raised temperature throughout the troposphere, with a 1-1.2 K increase in the low levels (below 500 hPa) and 1.5-2 K in the upper troposphere (see **Figure 4.16a**). A robust increase in specific humidity is also seen below 700 hPa, peaking at 0.7-1 g $kg^{-1}$ during the rainfall period (see **Figure 4.16c**). The difference between CTL and DTQW is even more pronounced for both variables. During the peak rainy days, near-surface temperature increases by more than 2 K, and low-level (below 700 hPa) specific humidity rises by about 1.6 g $kg^{-1}$ (see **Figures 4.16b, d**). This suggests that

additional wind circulation changes could further intensify anthropogenic warming, and thus filling a wetter environment in this case.

Human impacts on frontal intensity are then investigated by comparing the meridional gradient of 850-hPa equivalent potential temperature in CTL with perturbed runs (see **Figure 4.17**). A larger negative value represents a higher temperature gradient, indicative of more intense cold and dry air intrusion into the PRD region and thus enhanced frontal intensity. From CTL, a strong cold front approached the PRD on December 14, with eastward progression and became strongest on December 15 and 16, corresponding to the peak rainfall day. Compared to CTL, the cold front became weaker in the perturbed runs, with a larger reduction in DTQW than in DTQ, during the whole event period (see black dashed lines in **Figure 4.17**). This suggests that the human-influenced wind circulation anomaly can affect temperature changes in turn, such that altering precipitation characteristics.

To infer the dynamic processes under human-induced climatic change, we have inspected the variations in temporal-spatial evolution of 850-hPa horizontal wind components, as illustrated in **Figure 4.18**. Negative values in **Figures 4.18a, b, c** indicate a strong easterly wind, and positive values in **Figures 4.18d, e, f** denote a southerly wind. As presented in the CTL run (see **Figures 4.18a, d**), low-level southeasterlies dominated PRD from December 13 to 16, before shifting to northwesterly winds once the cold front arrived on December 17; meanwhile southerlies increased with time. The 850-hPa low-level jets with wind speed excessing 10 m $s^{-1}$ were found on December 15, with southerlies over eastern PRD and easterlies over western PRD corresponding to precipitation centers (see also **Figure 4.8a**). Compared with CTL, the low-level wind pattern in DTQ does not change considerably, except for slightly weaker jets (see **Figures 4.18b, e**). However in DTQW, the easterly jets appear to be more vigorous but with weaker southerlies (see **Figures 4.18c, f**). In other words, human activities induced an anomalous southwesterly over PRD during peak rainfall days in the CTL experiment.

In addition to the horizontal winds, vertical motion responses to human influences are also assessed. **Figure 4.19** presents the frequency distribution of the difference in 500-hPa pressure velocity in PRD between CTL and two perturbed runs, taken as strength of atmospheric vertical motion (Emori & Brown, 2005). Relative to DTQ, the stronger ascending motion, i.e., smaller than -0.6 Pa $s^{-1}$, tends to occur more frequently in CTL, while both weaker ascents and descents ($< \pm 0.6$ Pa $s^{-1}$) become less frequent (blue line in **Figure 4.19**). It suggests that human-induced thermodynamic effects on rainfall increase can be attributed to the more frequent occurrence of those stronger ascents. Note that frequency changes in CTL-DTQW are more upward motion (negative) but less downward motion (positive) in general (see red line in **Figure 4.19**). In fact, the frequency of upward motion changes displays a bimodal distribution with a primary peak at relatively weaker ascents of -0.45 Pa $s^{-1}$ and a minor peak at stronger ascents of -1.2 Pa $s^{-1}$, which probably explains the rainfall frequency changes in CTL-DTQW (see blue line in **Figure 4.10**).

Finally, we conducted moisture budget analyses to examine human-forced thermodynamic and dynamic contributions to precipitation variations. **Figure 4.20** presents the changes in daily precipitation and 1000-100 hPa vertically integrated moisture fluxes and convergences (VIMFC), as well as thermodynamic and dynamic terms for CTL minus perturbed runs, in terms of their spatial distribution (upper panels) and regional mean (bottom panels) during this event. As expected, the pattern of total moisture flux convergence changes greatly resembles the precipitation anomaly pattern, for both perturbed runs (see **Figures 4.20a, b, e, f**). It means that the moisture flux convergence change can well explain human-induced rainfall anomalies, such as an intensified southwest-northeast rainband and lower rainfall along the rainband's edges. Enhanced northward moisture transport in CTL-DTQW also supports a further increase in precipitation, due to the stronger southerly winds (see vectors in **Figure 4.20f**). The moisture flux convergence is then decomposed into two terms: a thermodynamic term, i.e., $-\int \nabla \cdot$

$\left(\vec{V}_{CTL}\delta q\right) dP$, dictated by specific humidity anomaly, and a dynamic term, i.e., $-\int \nabla \cdot \left(q_{CTL}\delta\vec{V}\right) dP$, determined by horizontal wind anomalies. For the thermodynamic term, overall its pattern is similar to the VIMFC anomaly pattern in CTL-DTQ, albeit with slightly less intensity, while in CTL-DTQW it contributes little or even negatively to VIMFC changes over the southeastern coast (see **Figures 4.20 c, g**). A quick check for negative thermodynamic contribution indicates that the anomalous moisture increase over the eastern SC (east of 114°E) was concentrated within lower levels (below 750 hPa), where easterly winds dominate in CTL and transported plentiful moisture to the west (rainband area) and dry the east, resulting in a negative contribution; on the contrary, human-caused moisture increase in the west extended from the surface up to higher altitudes (~600 hPa) accompanied with southwesterly in CTL, resulting in positive outcomes (not shown). For the dynamic term, CTL-DTQ shows its largest contribution to the VIMFC increase that occurred over the northwestern corner of PRD and Zhanjiang city (see **Figure 4.20d**). In contrast, CTL-DTQW dynamic term is highly consistent with the anomalous VIMFC and has a comparable magnitude to precipitation variations (see **Figure 4.20h**).

The bottom panels in **Figure 4.20** compare PRD-averaged moisture flux convergence changes and thermodynamic, dynamic terms for simulations from the six-member ensemble mean (bars) and individual members (error bars). The domain-mean in CTL-DTQ shows that both dynamic and thermodynamic terms contributed equally to the overall enhancement in moisture flux convergence under human-induced warmer and wetter climates (**Figure 4.20i**). Moreover, while individual members of simulations show a good agreement in the thermodynamic term, the dynamic term exhibits a relatively large variability across the members, as has been found by previous studies (Endo & Kitoh, 2014; Lee et al., 2017). This implies that the model uncertainty in simulating moisture flux convergence is more likely to be affected by the variability of the dynamic term. The CTL-DTQW domain-mean results confirm that the rainfall

increase is mostly driven by the increase in the dynamic term, with a minor contribution from the thermodynamic term (see **Figure 4.20j**), which is consistent with previous studies (Ali & Mishra, 2018). The nonlinear term (NL) and biases (Res) between changes in precipitation and moisture flux convergence are much smaller than other terms and can be neglected (Lee et al., 2017; Seager et al., 2010). More importantly, differences between two perturbed runs suggest that the human-caused dynamic effects are critical to the additional increase in this extreme precipitation.

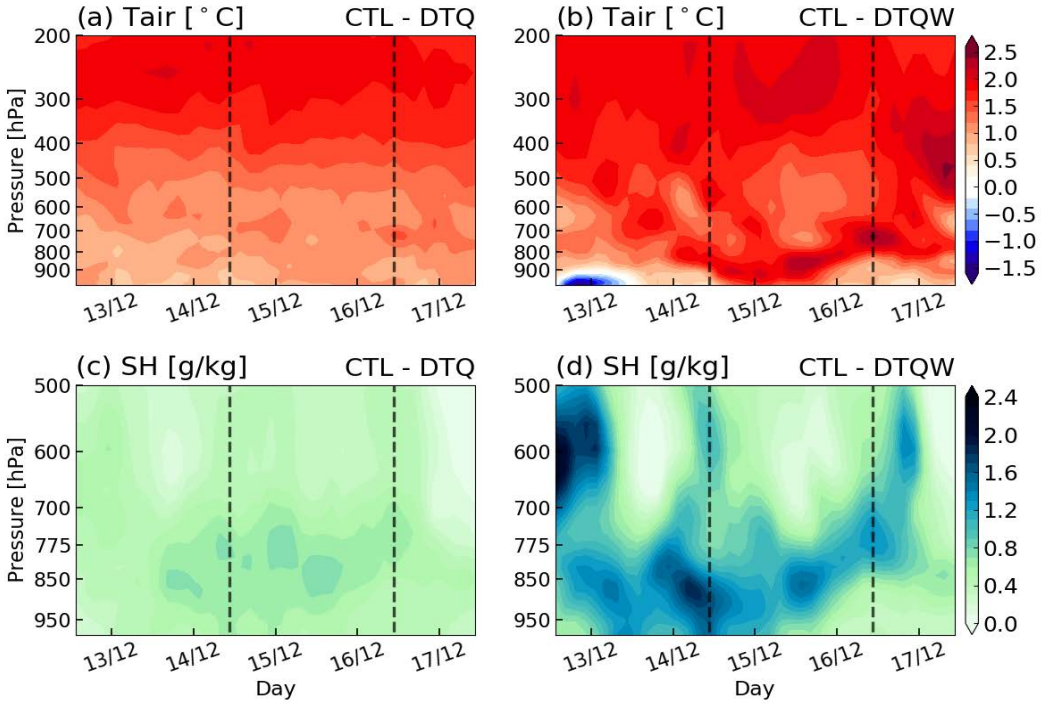


***Figure 4.16*** *Time evolution of differences in (a, b) air temperature (units: K) and (c, d) specific humidity (units: g kg$^{-1}$) averaged over PRD between (a, c) CTL and DTQ runs, (b, d) CTL and DTQW runs. Black dashed lines indicate the peak rainfall days on December 15 and 16.*

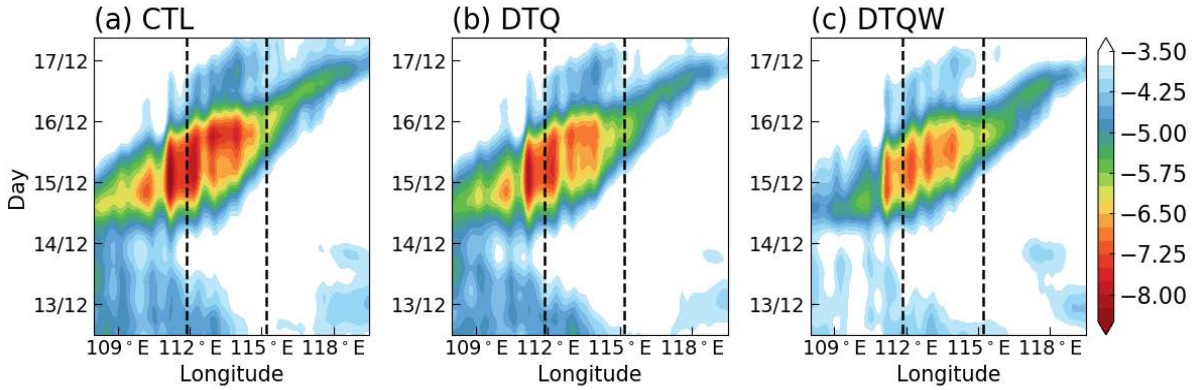


***Figure 4.17*** *Time-longitude cross-section of meridional gradient of the 850-hPa equivalent potential temperature (units: K 100 km$^{-1}$) averaged between 21.5°N-24.2°N in the (a) CTL, (b) DTQ and (c) DTQW runs, respectively. The black dashed lines outline meridional boundaries of the PRD region. See text for more details.*

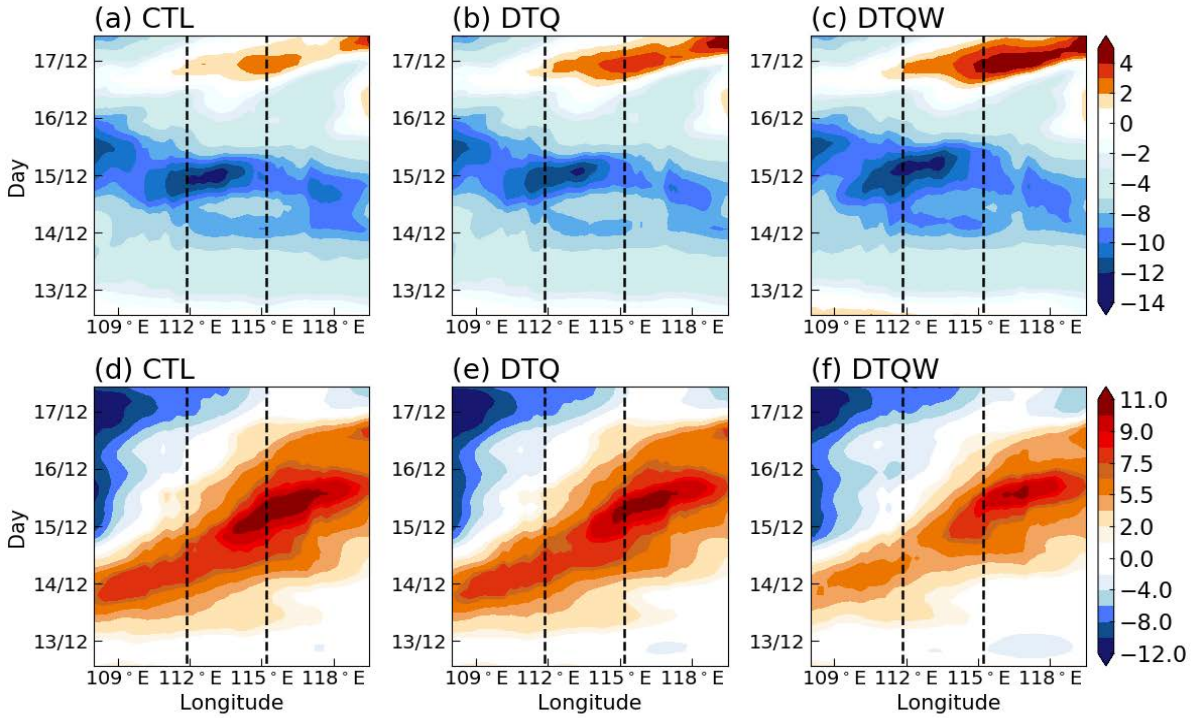


***Figure 4.18*** *Same as* ***Figure 4.17****, but for the 850-hPa (a-c) zonal and (d-f) meridional winds (units: m s$^{-1}$).*

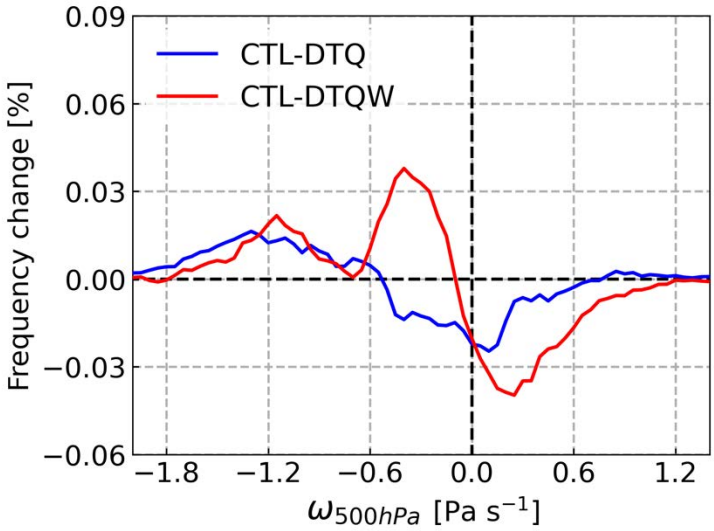


***Figure 4.19*** *Difference in the frequency of 500-hPa pressure velocity (units: Pa s$^{-1}$) over PRD for December 14-17, between CTL and DTQ (blue line), CTL and DTQW (red line).*

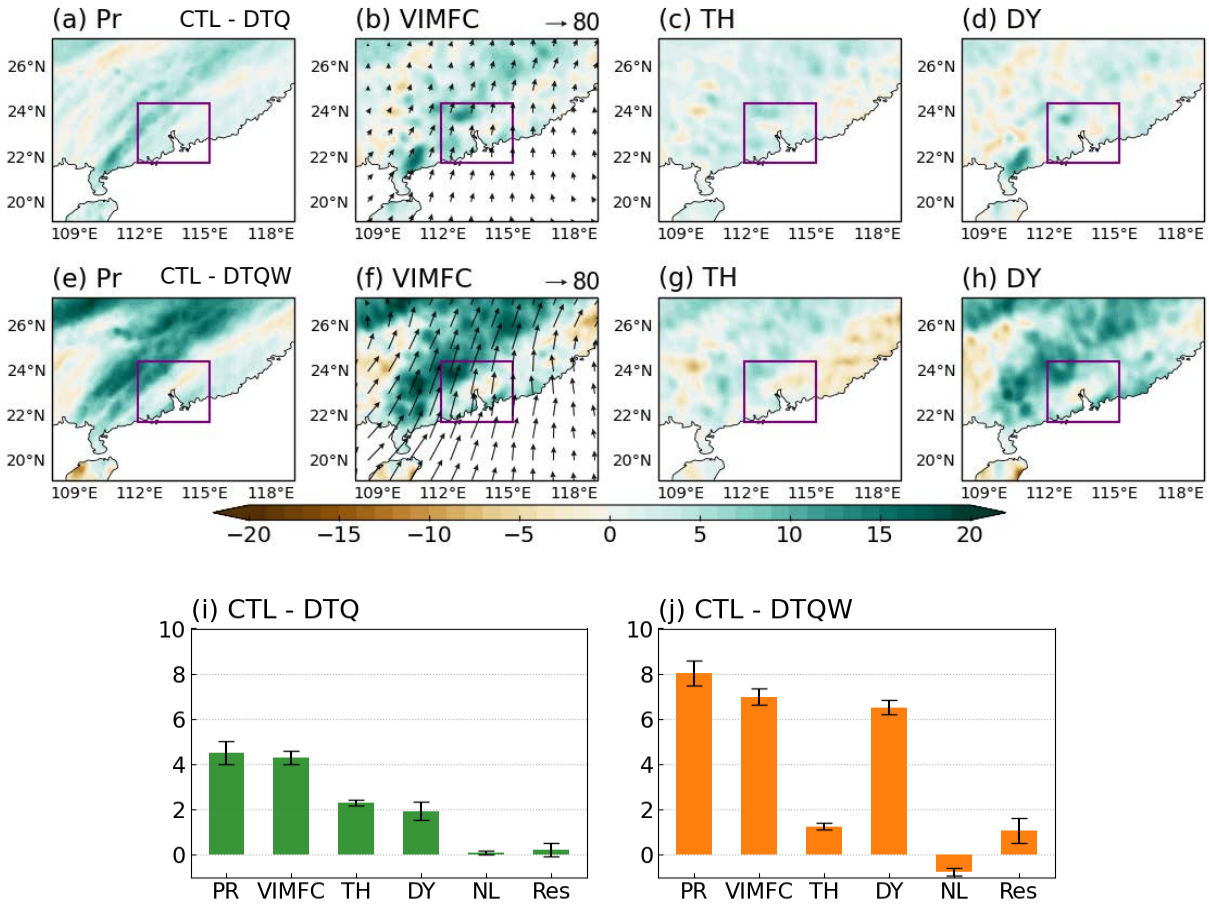


***Figure 4.20*** *Differences between (a-d) CTL and DTQ, (e-h) CTL and DTQW in (a, e) 4-day mean precipitation (PR), (b, f) 1000-100 hPa vertical-integrated moisture fluxes (vectors; see the scale at top right in units of kg* $m^{-1}s^{-1}$*) and convergences (VIMFC; shading), as well as the separated (c, g) thermodynamic (TH) and (d, h) dynamic (DY) terms, averaged over the event period. Also shown are the regional-averaged changes in PR, VIMFC, DY, TH, and a nonlinear term (NL, i.e., VIMFC-TH-DY) and residuals (Res, i.e., PR-VIMFC) that passed the 90% confidence level, for (i) CTL-DTQ and (j) CTL-DTQW. All these terms are in units of mm per day for comparison. Purple boxes in upper panels outline the PRD region.*

## 4.5 Brief summary

We examined the sensitivity of an extraordinary precipitation event in winter 2013 over PRD to human influence using the WRF model, and explored underlying mechanisms for the

simulated rainfall anomaly. Based on a multi-physics ensemble, the WRF well reproduced the observed rainfall, in terms of its rainband location and evolution. The quantitative attribution analysis was conducted by re-simulating this event in WRF, forced at the initial and boundary climate with human-induced temperature and humidity anomalies removed (DTQ), and the additional wind circulation anomalies removed on top of DTQ (DTQW). Simply, CTL-DTQ represents the thermodynamic effects and CTL-DTQW indicates the combined effects of thermodynamic and dynamic changes induced by human forcing.

Spatial patterns of four-day mean precipitation illustrate that human activities have caused the intensity of rainfall center over the northwestern PRD to increase by 7-10% and 13-15% under a 1.2 K warming in CTL-DTQ and a 2 K warming in CTL-DTQW, respectively. We then quantified such human impacts by computing the rate of daily rainfall change with near-surface warming at each grid over PRD. The frequency of rainfall changes peaks at 10% $K^{-1}$ in CTL-DTQ, whereas it shows a bimodal distribution peaking at 10% $K^{-1}$ and 36% $K^{-1}$ in CTL-DTQW. On top of that, we examined the sensitivity of the average and extreme precipitation to human influences, and found that CTL-DTQ rainfall was enhanced by 11% and 13% for the mean and both extremes, respectively; CTL-DTQW shows larger increases of 17% and 19% (21%) in the mean and $95^{th}$ ($99^{th}$) percentile rainfall. Based on these findings, we conclude that 1) human-induced dynamic changes can accelerate the thermodynamic-driven rainfall increase in this event, i.e., higher probability in CTL-DTQW than CTL-DTQ; 2) daily mean rainfall changes are roughly consistent with the CC scaling of ~7% $K^{-1}$, whereas the extreme rainfall increase reaches nearly super-CC rate.

The underlying mechanisms for the human-related rainfall changes are summarized as follows:

(1) From the large-scale perspective, a noticeable low-level (850 hPa) temperature contrast between the China continent and SCS was found in CTL-DTQ, favoring anomalous southerly winds that bring sufficient moisture and warmer air from SCS towards the inland areas. Also,

the low-level wind convergence over SC and upper-level divergence over the north of PRD were strengthened with the help of human-forced thermodynamic and dynamic effects (CTL-DTQW), which stimulates the intense convection activities and thus increases rainfall.

(2) From the local-scale perspective, the cold frontal intensity tends to get stronger in PRD, as more warm moist air moved northward and conflicted with the southward dry cold air due to the stronger wind convergence mentioned above. It also facilitates the strong ascending motions to occur more frequently. As a result, the dynamic component turned to be a major contributor to the rainfall increase in CTL-DTQW, while the moisture-driven thermodynamic contribution was limited. On the other hand, the thermodynamic and dynamic changes contributed equally to anomalous rainfall in CTL-DTQ.

# Chapter 5 Attribution a pre-monsoon heavy rainfall event to anthropogenic influences

In Chapter 3, multi-case attribution analysis revealed a seasonally dependent response of PRD heavy precipitation to human influences, with CC scaling in MJJAS but super-CC scaling in non-MJJAS rainfall. This super-CC behavior was further investigated by studying a wintertime extreme rainfall event, and the underlying physical mechanisms for such additional intensification were examined in Chapter 4. This chapter focuses on the sensitivity of the so-called pre-monsoon rainfall changes to human forcing and possible causes.

Summer monsoon precipitation responses to human influences have been investigated in many previous studies (Ueda et al., 2006; Burke & Stott, 2017; Lee et al., 2018). However, human impacts on pre-monsoon heavy precipitation over PRD remain unclear, despite the importance of pre-monsoon rainfall; for instance, it contributes about half of the annual precipitation in the Guangdong Province (Luo et al., 2017). Interestingly, CMIP5 global models results indicate that the 95$^{th}$ percentile extreme rainfall in May over PRD appears to be reduced due to human activities (see **Figure 5.1**). Here we examine in details a pre-monsoon heavy rainfall case in May 2016, and carry out an attribution analysis using a convection-resolving model.

## 5.1 Synoptic background

The pre-monsoon heavy precipitation event in Guangdong took place on May 15, 2016. A rain belt was found spanning the cities of Guangzhou, Foshan, and Jiangmen, where the accumulative daily rainfall reached at least 50 mm and the maximum rainfall exceeded 80 mm, based on TRMM 3B42 (**Figure 5.4a**). **Figure 5.2** depicts the synoptic background of this event, showing the spatial distribution of precipitable water, equivalent potential temperature and horizontal winds at the 850 hPa level. This case is characterized by a strong gradient of

equivalent potential temperature ($\theta_e$) accompanied by strong low-level northerly winds. The latter advected the cold and dry air southward to the "25-30°N" band over the continental area. Near the coast, low-level westerly and southwesterly transported warm and moist air northward; together with the southward cold airflows over the north of the coastline, an intense front system was found with large $\theta_e$ gradient. In particular, maximum $\theta_e$ (343K) was located along the coast, such as the PRD inland areas. We also found that precipitable water, i.e., total amount of water vapor integrated over the entire tropospheric column reached about 50-60 g $kg^{-1}$ from the Guangdong to Zhejiang Province. These aforementioned meteorological conditions contribute to the heavy rainfall in PRD on that particular day.

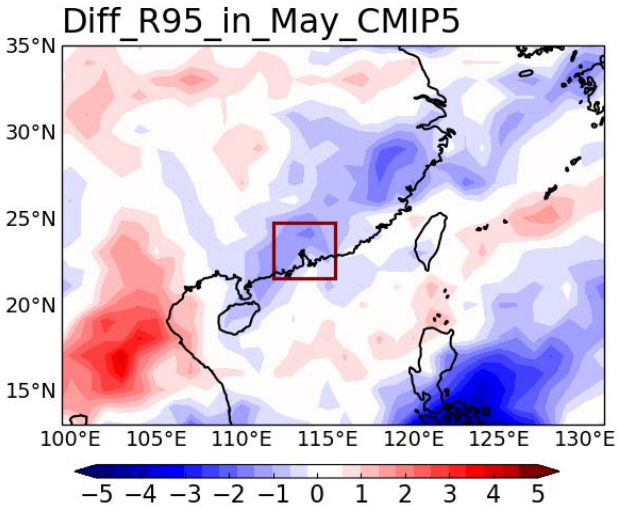


***Figure 5.1*** *Difference in the 95$^{th}$ percentile of daily precipitation (units: mm $d^{-1}$), averaged over May of 1986-2005, between historical and natural runs from CMIP5 GCMs ensemble mean. The red box outlines the PRD region.*

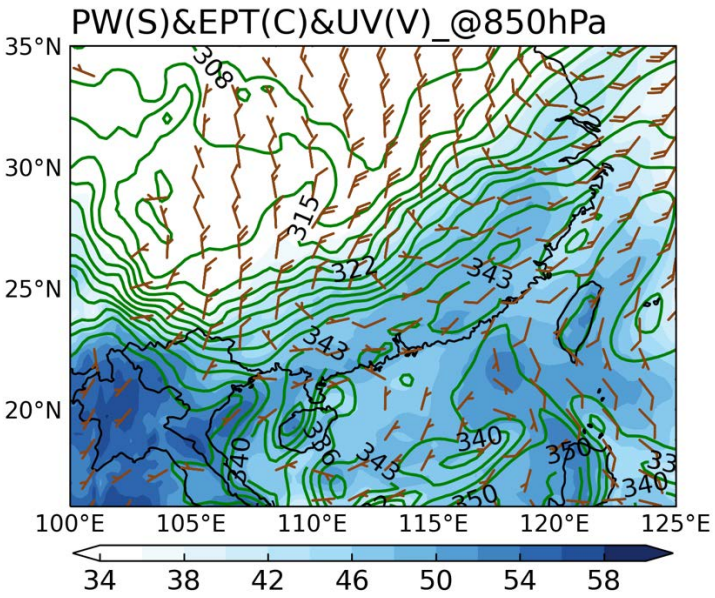


***Figure 5.2*** *Precipitable water (shading; units: kg m$^{-2}$), equivalent potential temperature (green counters; units: K) and horizontal winds (vectors; units: m s$^{-1}$) at 850 hPa averaged on May 15, based on ERA5 reanalysis.*

## 5.2 Evaluation of the simulated event

We have conducted three sets of experiments by downscaling this event under the historical (CTL run) and two different counterfactual initial and boundary conditions (IBCs) separately. Each set of simulations was run with 14 ensemble members comprising different microphysics schemes and starting times (see more details in Chapter 2.3.2). The ensemble mean of simulations outperformed individual runs (not shown), so the former was used in the following analysis. The meteorological variables, including horizontal winds, geopotential height, and temperature at various pressure levels, produced by the WRF CTL run from the ensemble of fourteen members were compared against reanalysis, and results are shown in **Figure 5.3**. It is evident that the simulated horizontal U- and V-wind components were in good agreement with reanalysis, except for a slight underprediction of zonal winds exceeding about 17 m s$^{-1}$ (see **Figures 5.3a-f**). Unlike the horizontal winds, the WRF model overestimated the observed geopotential height by 30 m at 250 hPa and 20 m at 500 hPa, while an underestimation of ~80

m at 850 hPa was found (see **Figures 5.3g, h, i**). It was noteworthy that the simulated 850-hPa temperature compares well with reanalysis data (see **Figures 5.3j, k, l**). On the other hand, the model tends to generate a warmer mid-level troposphere and colder upper layers, with a ~0.4℃ positive bias for 500-hPa and a 0.1-0.5℃ negative bias for 250 hPa temperature. We also evaluated the specific humidity and pressure velocity over PRD in the control run (see **Figure 5.4**). Overall, variations of specific humidity with time and altitudes were reasonably well captured by WRF, with the maximum moisture amount concentrated at the 850 hPa layer on May 14 and 15 (see **Figure 5.4a, b**). Strong ascending motion (negative pressure velocity), associated with the rainfall peak on May 15, was well simulated, albeit with weaker intensity (especially in the 400-600 hPa layer). The simulated downward motion from 600 to 800 hPa on May 15 and 16 was also underestimated compared with ERA5. Model daily precipitation during the peak of this event was also compared with TRMM 3B42 data. As can be seen from **Figure 5.5**, a rain belt extending from the Guangdong to Fujian Province was reproduced by the WRF CTL run, despite the model's limitations in simulating its actual magnitude and location. For instance, the model rain belt was displaced southward thus located closer to the coast and was less intense; the latter underestimation is consistent with the weaker upward motion in the model. Overall, WRF is capable of replicating the main features of this event, although there are some biases in the upper-air variables and rainfall, in terms of their intensities.

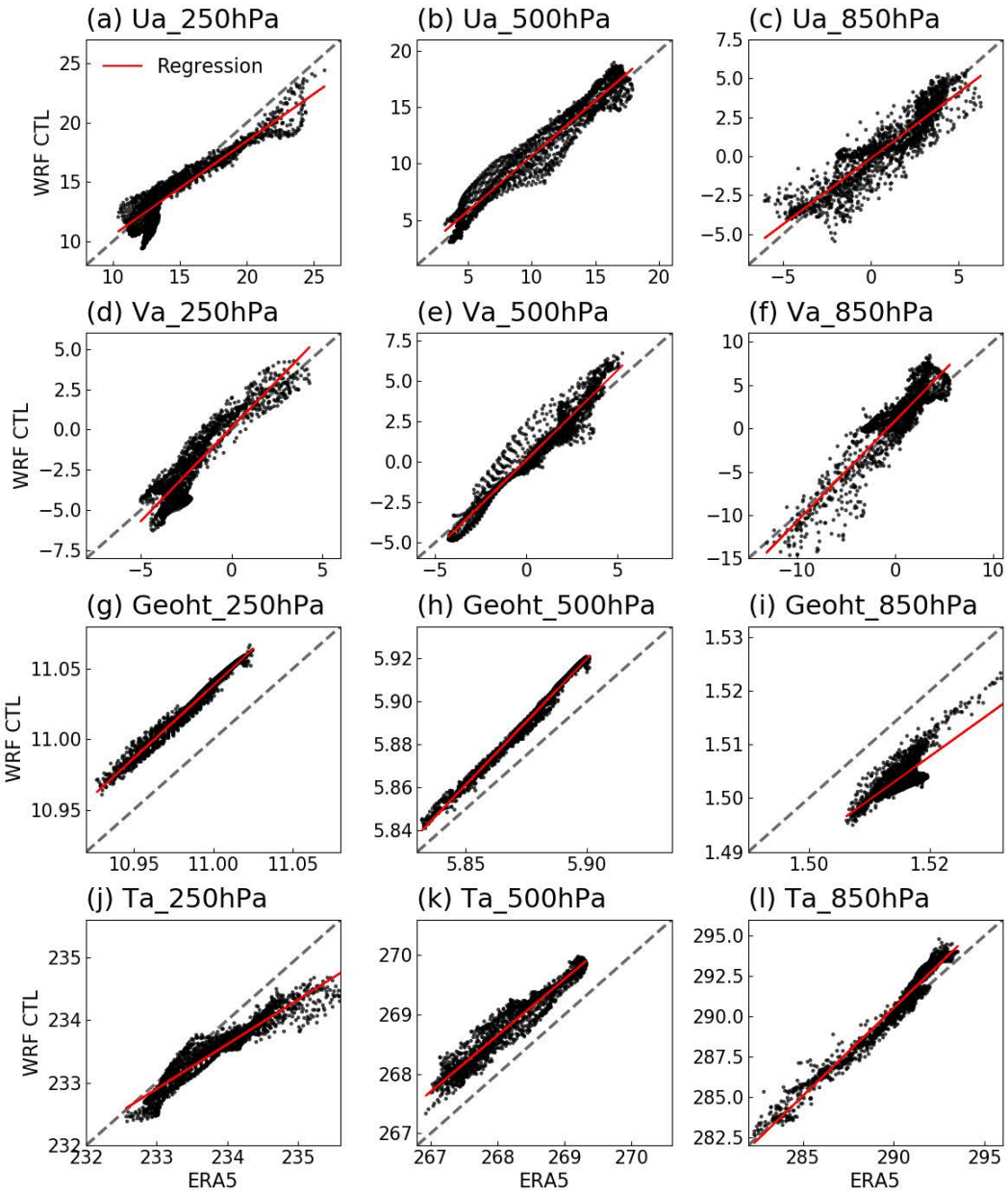


***Figure 5.3*** *Bias scattering plots of (a-c) horizontal U-wind and (d-f) V-wind components (units: m s$^{-1}$), (g-i) geopotential height (units: km) and (j-l) air temperature (units: K) at 250 hPa (left column), 500 hPa (middle column), and 850 hPa (right column) over domain 2 (SC) on May 2016, derived from the ensemble mean of WRF CTL simulations versus ERA5 reanalysis.*

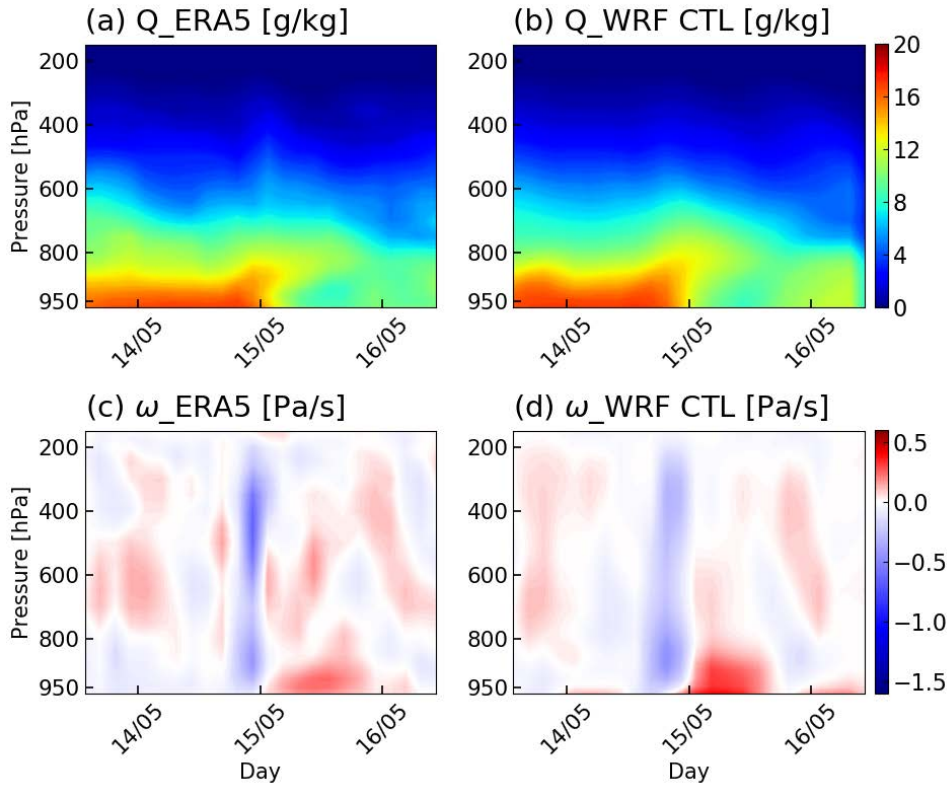


***Figure 5.4*** *Time evolution of (a, b) specific humidity (units: g kg$^{-1}$) and (c, d) pressure velocity (units: Pa s$^{-1}$) over PRD for (a, c) ERA5 reanalysis and (b, d) WRF CTL ensemble.*

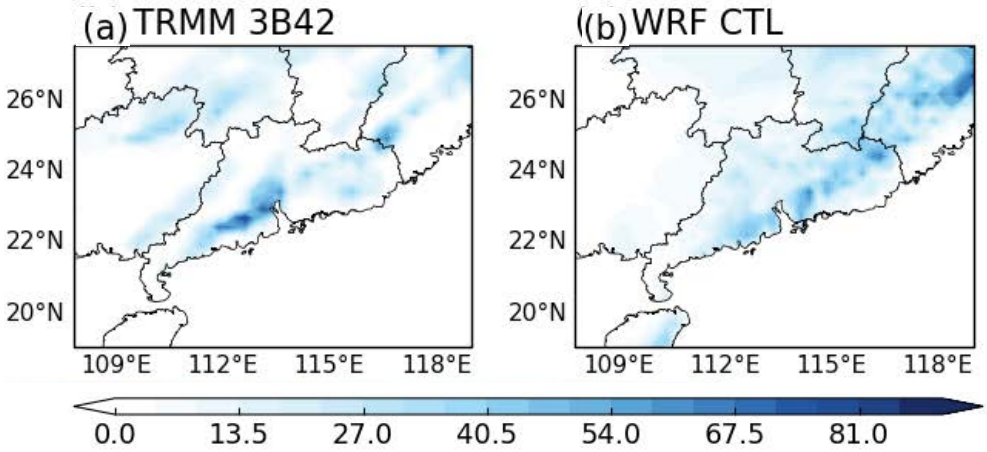


***Figure 5.5*** *Daily precipitation (units: mm d$^{-1}$) over domain 2 (SC) on May 15, obtained from (a) TRMM 3B42 observations and (b) WRF CTL ensemble.*

## 5.3 Human-induced pre-monsoon rainfall changes

To assess the impacts of human forcing, two counterfactual experiments as aforementioned were carried out: in DTQ run, the model was forced with IBCs that had human-forced temperature and specific humidity anomalies subtracted from the IBCs in CTL, and in DTQW run the same anomalous signals as in DTQ as well as human-induced horizontal wind anomalies were removed. We first examine the pre-monsoon daily precipitation responses to human influences. **Figure 5.6** presents the spatial patterns of daily precipitation on May 15 in CTL and significant rainfall differences between CTL and those two perturbed runs. From **Figure 5.6a**, strong daily rainfall is found mainly over the coastal and neighbouring northern inland areas, with maximum rain rates reaching 45 mm. A noticeable spatially dependent response to anthropogenic forcing was seen for both perturbed runs. Surprisingly, due to human-related thermodynamic forcing, rainfall rates over the central and eastern PRD were significantly reduced in CTL relative to DTQ (see **Figure 5.6b**). In particular, the rainfall center within Huizhou city (23.06°N, 114.24°E) has experienced a maximum rainfall reduction of more than 18 mm (around 70% relative to DTQ). This result is different from previous findings that rainfall increases under human forcing at the rate of CC or super-CC scaling. On the other hand, rainfall over southwestern areas was found to be 5-14 mm (25%-40%) greater in CTL than DTQ. Possible mechanisms for the unexpected rainfall change will be explored in the following section.

Compared to DTQW, CTL rainfall in southwestern and parts of northern areas has intensified, with the largest increase in Zhongshan city; however, rainfall over the eastern parts was slightly reduced due to anthropogenic forcing (see **Figure 5.6c**). By comparing the two perturbed runs, rainfall increases over the west are larger in CTL-DTQW than in CTL-DTQ; more importantly, rainfall decreases in CTL-DTQ were partially alleviated in CTL-DTQW by human-induced wind circulation changes. This result suggests that human-induced dynamic changes have a

positive impact on this pre-monsoon rainfall, whereas thermodynamic changes appear to have a more complicated impact.

To qualify this pre-monsoon precipitation variation with anthropogenic warming, we computed the daily rainfall changes, defined as the difference of rainfall in CTL relative to DTQ and DTQW, per degree of warming in the 2-m temperature. Its frequency distribution for all grid points over PRD was shown in **Figure 5.7**. For this particular event, the most likely changes are found to be negative, with a decrease of ~20% and 16% per K warming for CTL relative to DTQ and DTQW, respectively. Compared with DTQ, DTQW rainfall frequency is displaced to more positive rainfall changes, consistent with the above rainfall pattern results (see **Figure 5.6c**).

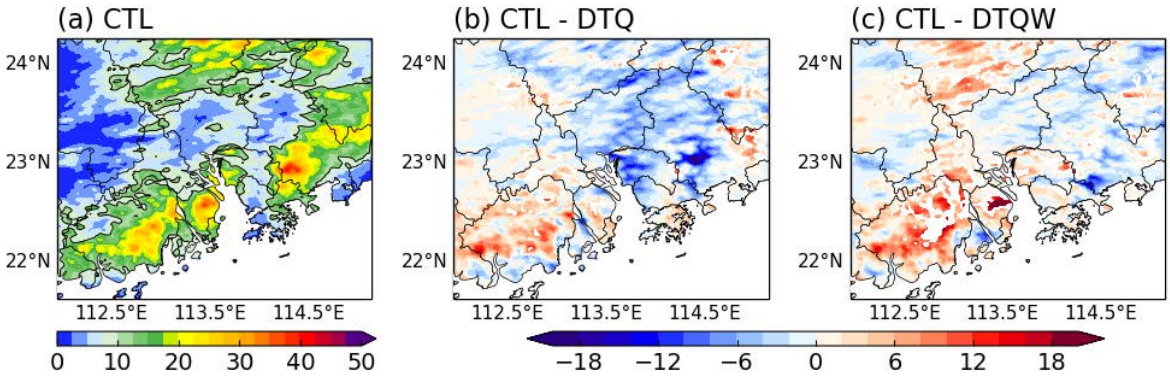


***Figure 5.6*** *Spatial distribution of daily precipitation (units: mm $d^{-1}$) on May 15 over PRD, from (a) WRF CTL run, where rain rates greater than 10 mm $d^{-1}$ were outlined by black contours. Also shown are the precipitation differences between (b) CTL and DTQ, (c) CTL and DTQW that passed the 90% significance level.*

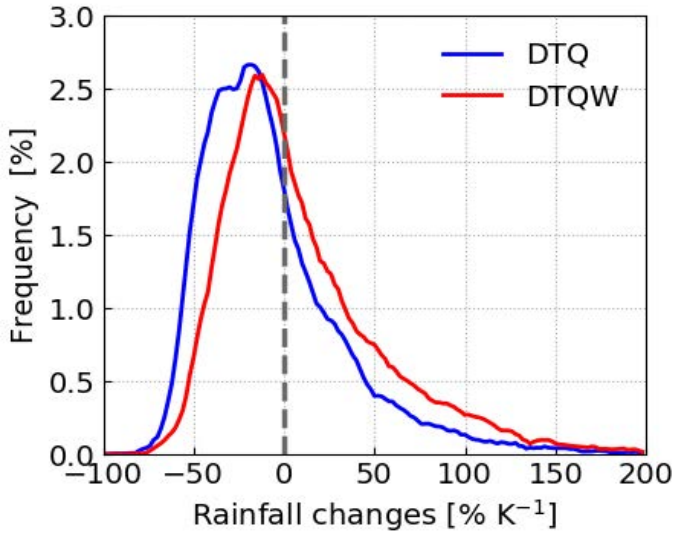


***Figure 5.7*** *Frequency distribution of percentage changes in daily precipitation per K of 2-m warming on May 15 over PRD, in CTL compared to DTQ (blue line) and DTQW (red line). The rainfall change was calculated at each model grid that passed the 90% significance level.*

## 5.4 Physical mechanisms for rainfall changes

We first investigate human influences due to thermodynamic effects. **Figure 5.8** gives the difference in the low-level (1000-700 hPa) mean temperature, 850-hPa specific and relative humidity on May 15, between CTL and the perturbed runs. The temperature difference indicates a warmer lower troposphere by more than 0.8℃ due to human activities, with minimum warming in southwestern PRD (Zhongshan and Jiangmen cities) and strong warming of 1-1.3℃ in the rest of PRD (see **Figures 5.8a, b**). From DTQW run, the human-induced wind circulation anomaly resulted in further warming in the low levels (**Figure 5.8b**). The low-level specific humidity change, however, gives very different spatial patterns (see **Figures 5.8c, d**), with water vapor amount increasing more substantially in the west (> ~1.0 g kg$^{-1}$) than in the central and eastern part of the domain (< 0.7 g kg$^{-1}$). Due to the higher (smaller) moisture enhancement under a weaker (intense) low-level warming in the west (east) of PRD, the low-level relative humidity was enhanced (reduced) accordingly by at most 4% (3%), as shown in

**Figures 5.8e, f**. Although the moisture increase with temperature did not strictly follow the CC relation in some areas, it still holds in the regional-averaged sense, since at the regional scale the PRD domain-mean relative humidity remains constant. Comparing these to the rainfall suppression in the east of 113.5°E (see **Figures 5.6b, c**), the latter seems likely to be related to the reduced relative humidity in that region. The relation between reduction in rainfall intensity and relative humidity is more striking near the coast where rainfall was concentrated (see **Figure 5.6a**). Therefore, human-induced thermodynamic and dynamic processes play equally important roles in modulating rainfall, a point which we will further elaborate on later.

Changes of those thermodynamic anomalies at different pressure levels are also illustrated in **Figure 5.9**. Relative to both perturbed runs, CTL results show that eastern PRD (east of 113.5°E) is warmer than the west, especially for the 800-500 hPa layer (see shading in **Figures 5.9a, b**). However, specific humidity increased less in the east throughout the low-to-mid troposphere (below 500 hPa). In fact, the largest increase was found in the western part of the domain at 1000-850 hPa; with the smallest rise in temperature (see black contours in **Figures 5.9a,b**), this leads to the increase of relative humidity (see green contours in **Figures 5.9a,b**). On the other hand, relative humidity above 850 hPa was reduced in eastern PRD, due to excessive warming and less increase in moisture amount. Thus rainfall reduction (increase) was related, more specifically, to the 1000-850 hPa relative humidity decrease (increase).

The PRD area-averaged vertical profiles of these anomalous variables are shown in the bottom panels of **Figure 5.9**. Due to human activities, the regional-mean temperature below 700 hPa was raised by 0.9 ℃ (~1 ℃) in CTL-DTQ (CTL-DTQW); however, CTL-DTQ has a warmer 700-500 hPa layer and became colder above 500 hPa, compared to CTL-DTQW (see **Figure 5.9c**). Below 850 hPa, specific humidity was enhanced by ~0.7 g $kg^{-1}$ in CTL-DTQ and ~0.9 g $kg^{-1}$ in CTL-DTQW (see **Figure 5.9d**). While there are slight increases in relative humidity below 850 hPa due to its noticeable increase over western PRD, it was reduced by around 2.5%

in the low-to-mid levels in CTL relative to both perturbed runs (see **Figure 5.9e**). Further comparison between DTQ and DTQW indicates that CTL-DTQW appears to have a low-level (below 850 hPa) warmer and wetter troposphere than CTL-DTQ, which accounts for more rainfall in CTL-DTQW than in CTL-DTQ (**Figures 5.6b, c**). More notably, while increments in CAPE in two perturbed runs were very similar, CIN above 850 hPa in CTL-DTQ was much higher than in CTL-DTQW, as shown in **Figure 5.10**.

We have also examined how the frontal system in this event responses to anthropogenic warming by computing the difference in meridional gradients of 850-hPa equivalent potential temperature $\theta_e$ in CTL relative to two perturbed runs separately. **Figure 5.11** shows that there are positive (negative) gradients, denoting a weaker (stronger) front intensity due to human activities. The zonal mean $\theta_e$ gradients clearly illustrate that the front tends to be more intense in western PRD but weaker in the central and eastern parts. It is noteworthy that CTL-DTQW gives stronger negative gradients in the western part of the domain than CTL-DTQ, which shows that the front was further intensified due to dynamic effects, consistent with a larger rainfall increase in CTL-DTQW.

The physical mechanism for those findings from thermodynamic aspects can be summarized as follows: human-induced strong tropospheric warming alone resulted in a decrease in low-level relative humidity and consequently increased CIN values together with the weaker front intensity, leading to reductions of pre-monsoon extreme rainfall; on the other hand, human-caused enhancements in both specific and relative humidity due to minor warming, and the strengthened front intensity jointly contributed to the rainfall increase.

To further examine human influences due to dynamic effects, **Figure 5.12** presents the anomalous pressure velocity and zonal wind changes along longitudes and altitudes. Over the eastern PRD (113.5°E-114.5°E), CTL-DTQ shows much weaker vertical motion (positive anomalous omega) throughout the troposphere than CTL-DTQW (see shading in **Figures**

**5.12a, b**). In particular, the weakest vertical motion occurred around the longitude of 114.4°E, collocated with rainfall reduction signals in CTL-DTQ. In the west of 113.5°E, CTL-DTQW obviously shows a stronger ascending motion (negative anomalous omega) that supports precipitation intensification, whereas CTL-DTQ shows no significant change. The domain-averaged profiles of pressure velocity indicate that CTL-DTQ has weaker vertical motion above 900 hPa, with strongest perturbations of ~0.031 Pa $s^{-1}$ at 500 hPa; the vertical motion in CTL-DTQW, on the contrary, shows no substantial change, except for the 500-hPa weaker ascents and relatively stronger ascents near the surface (see **Figure 5.12c**). Besides, anomalous easterly winds below 400 hPa and westerly winds above 400 hPa are found in CTL relative to both the perturbed runs, suggesting strengthened vertical zonal wind shears caused by human influences (see contours in **Figures 5.12a, b**). The stronger upper-level westerlies belong to the southern wind branch related to the anomalous 250-hPa cyclone over SC, as inferred from the CMIP5 ensemble (not shown). This anomalous cyclonic pattern is likely to inhibit the upward motion restrain large-scale convections, resulting in the overall rainfall reduction (see **Figure 5.7**).

Human-related low-level wind circulation changes over SC are further addressed. **Figure 5.13** depicts the horizontal winds and temperature at 850 hPa in the control run, as well as their differences from the perturbed runs. CTL clearly shows the low-level wind convergence of strong northerly with southwesterly winds across the northwest of Guangdong (see vectors in **Figure 5.13a**). However, in comparison to DTQW, these northerlies in CTL became weaker, and anomalous southerly winds dominate the SC, with significantly warmer land temperatures than the ocean (see **Figure 5.13c**). In contrast, there was no substantial wind anomaly over Guangdong in CTL-DTQ (see **Figure 5.13b**). Human-forced anomalies in precipitable water and vertically integrated moisture fluxes are also illustrated in **Figure 5.14**. Compared to both perturbed runs, precipitable water in CTL was enhanced more substantially in the western parts

of Guangdong than in the east (see shading in **Figures 5.14b, c**), which is mostly contributed by the 850-hPa specific humidity increases (see **Figures 5.8c, d**). Furthermore, CTL-DTQW tends to have a greater increase in total moisture amount than CTL-DTQ, accompanied by the anomalous northward moisture transport; this indicates that more sufficient moisture was delivered from SCS to the inland, creating a favorable condition to offset the rainfall decrease in CTL-DTQ (see vectors in **Figure 5.14c**).

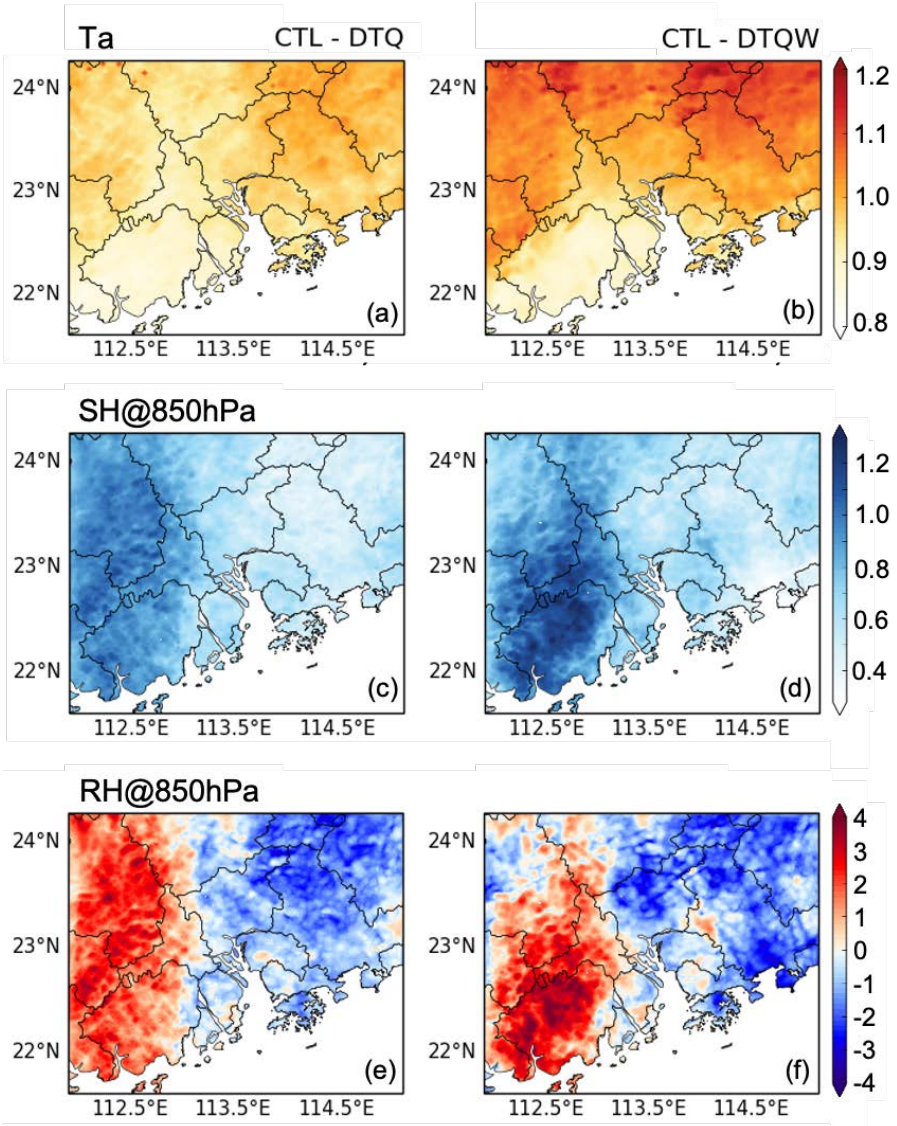


***Figure 5.8*** *Anomalous distributions of (a, b) 1000-700 hPa averaged temperature (units: K), (c, d) 850-hPa specific humidity (units: g kg$^{-1}$) and (e, f) 850-hPa relative humidity (units: %) on May 15, between (a, c, e) CTL and DTQ, (b, d, f) CTL and DTQW.*

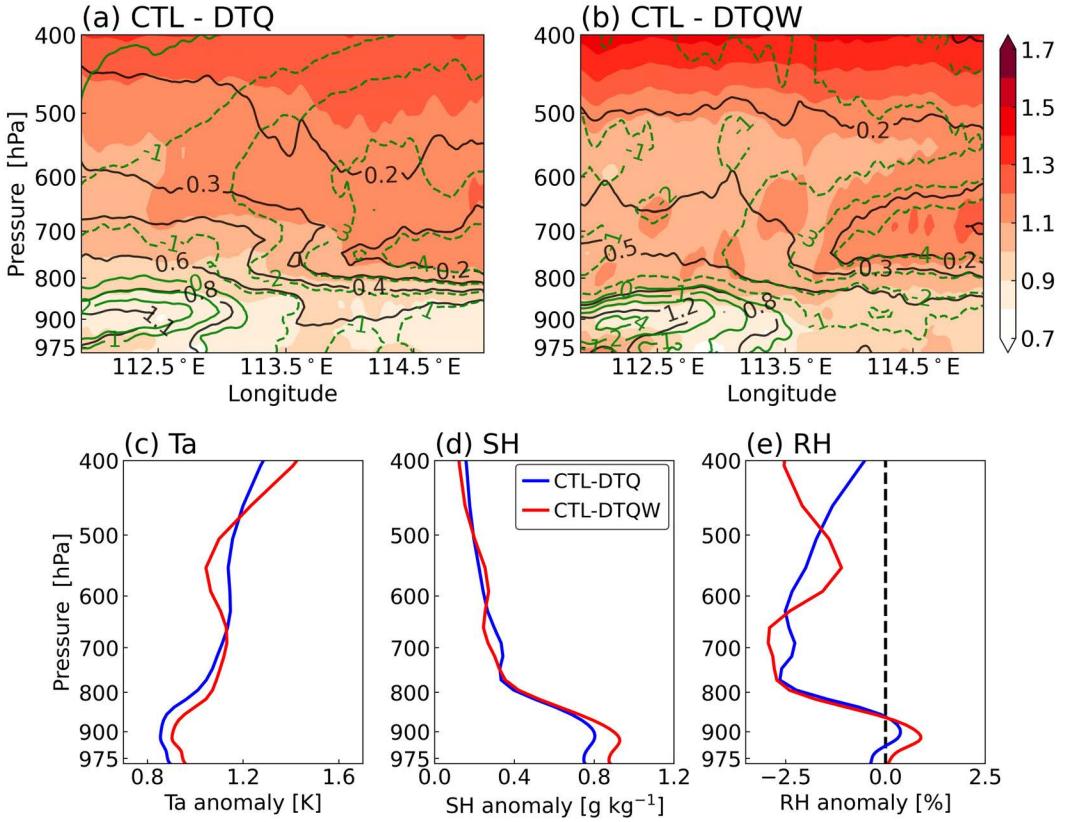


***Figure 5.9*** *Longitude-pressure cross section of anomalous air temperature (shading, units: K), specific humidity (black contours, units: g kg$^{-1}$), and relative humidity (green contours, units: %) averaged over latitudes of 21.7-24.1°N on May 15, for (a) CTL minus DTQ, and (b) CTL minus DTQW; (c), (d), (e) show the vertical profile of PRD-averaged anomalous temperature, specific and relative humidity for CTL-DTQ (blue line) and CTL-DTQW (red line), respectively.*

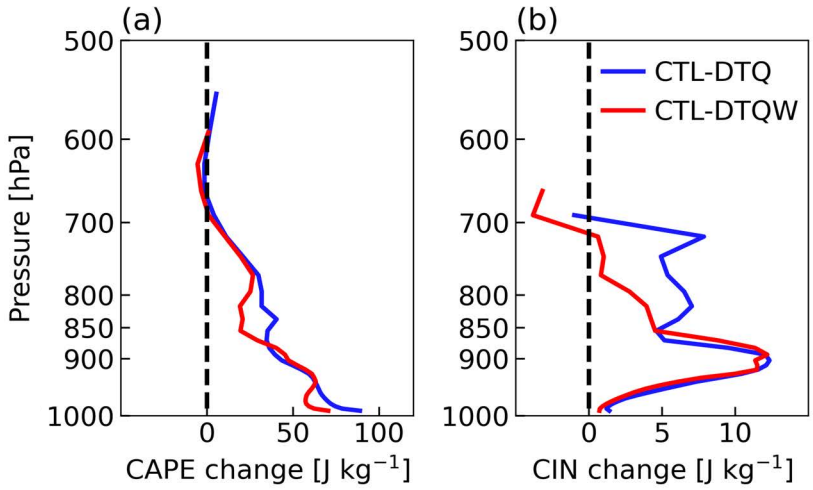


***Figure 5.10*** *Vertical profiles of changes in (a) convective available potential energy (CAPE), and (b) convective inhibition (CIN) averaged over the PRD on May 15, for CTL minus DTQ (blue line) and CTL minus DTQW (red line).*

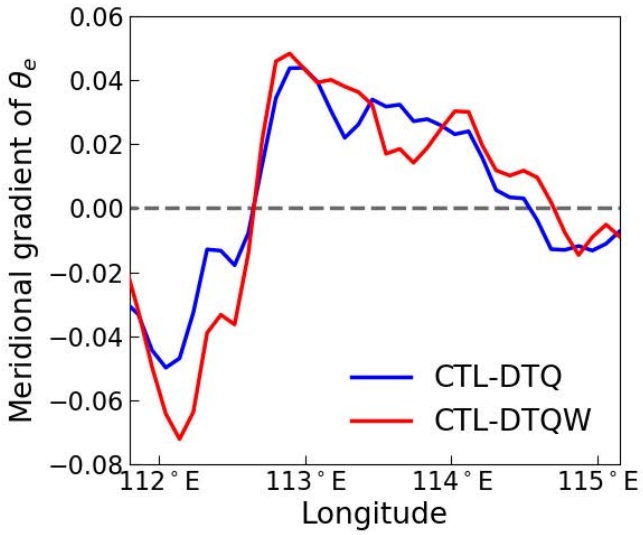


***Figure 5.11*** *Differences in the meridional gradient of 850-hPa equivalent potential temperature (units: K 100 km$^{-1}$) varies with longitudes, averaged over latitudes of 21.7°N-24.1°N (boundary of PRD) on May 15, between CTL and DTQ (blue line), CTL and DTQW (red line).*

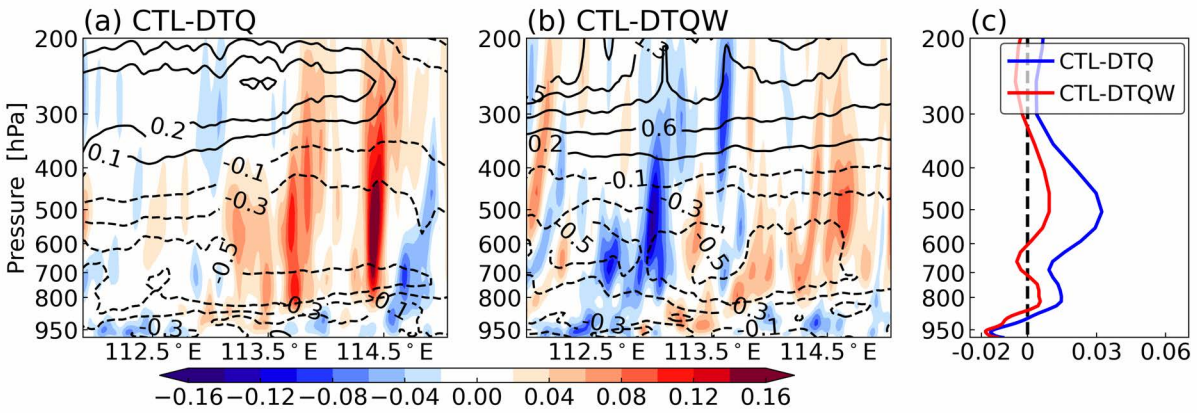


***Figure 5.12*** *Same as Figure 5.9, but for (a), (b) anomalous pressure velocity (shading, units: Pa s$^{-1}$) and zonal winds (contours, units: m s$^{-1}$), as well as the (c) vertical profile of anomalous pressure velocity.*

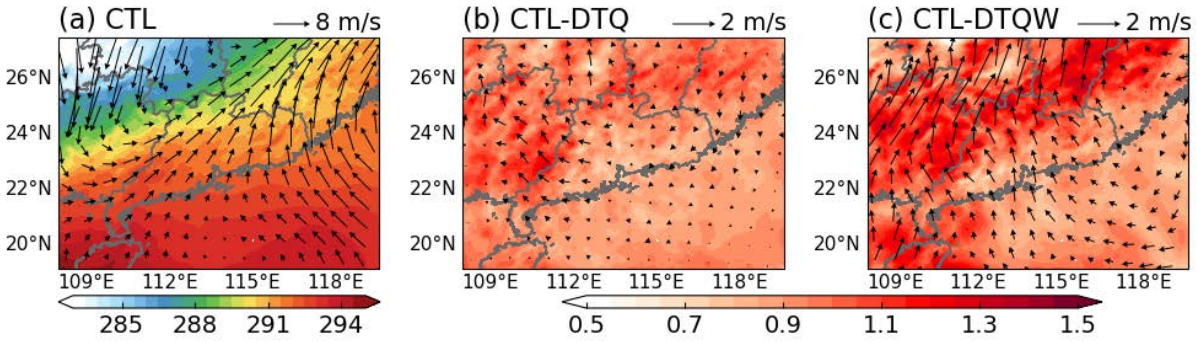


***Figure 5.13*** *Temperature (shading, units: K) and horizontal winds (vectors; see scales at top right in units of m s$^{-1}$) at 850 hPa on May 15 in (a) CTL, and their differences between (b) CTL and DTQ, and (c) CTL and DTQW.*

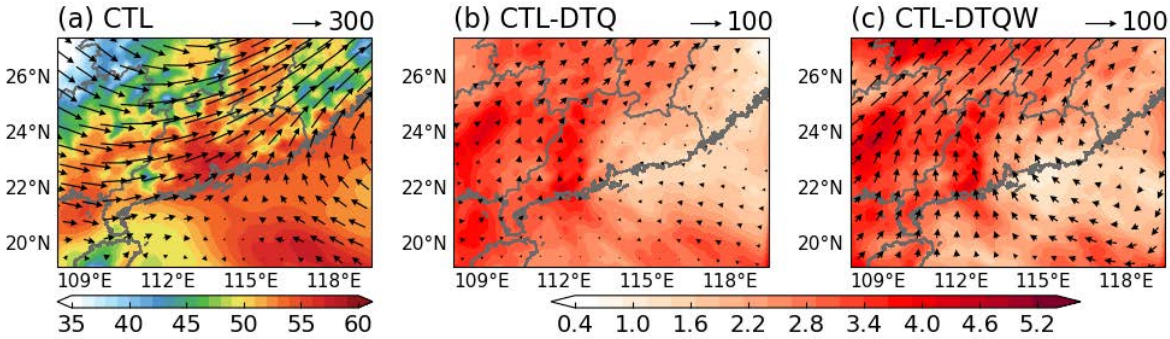


***Figure 5.14*** *Same as* ***Figure 5.13****, but for precipitable water (shading, units: kg m$^{-2}$) and vertically-integrated moisture fluxes (vectors; see scales at top right in units of kg m$^{-1}$ s$^{-1}$).*

## 5.5 Brief summary

Attributing a pre-monsoon heavy rainfall change to human influences was conducted using the WRF model in this chapter. A 14-member ensemble was used to reduce the internal model variability, and the ensemble of simulations agrees well with the observed precipitation and the associated synoptic conditions during this event. In contrast to previous findings that extreme rainfall increases consistently with human forcing, the ensemble results of this event indicates that human-induced thermodynamic forcing could have reduced the intensity of the maximum rainfall center over Huizhou city by at least 70%, despite the increased water vapor amount under anthropogenic warming (CTL-DTQ). On the other hand, rainfall over the western PRD is enhanced by 25%-40% due to human-related thermodynamic effects, with a further increase caused by dynamic effect (CTL-DTQW). The probability distribution of rainfall changes with warming shows that rainfall in this event is more likely to decrease by around 20% per kelvin near-surface warming. However, the rainfall reduction is partially alleviated by human-related dynamic effects (16% $K^{-1}$).

The main causes for the spatial-dependent rainfall responses to human forcing are summarized as follows:

(1) Precipitation reduction in the eastern PRD jointly resulted from the weaker cold-frontal intensity and higher CIN associated with the decreased relative humidity, as well as the dominance of weaker ascending motions under a warmer climate.

(2) On the other hand, rainfall increase over western PRD can be attributed to substantial enhancements in both specific and relative humidity at lower levels, as well as a strengthened front intensity. Besides, human-induced stronger southerly winds and enhanced northward moisture transport further intensify this pre-monsoon extreme rainfall, reflecting a positive dynamic effect.

Above all, human-caused thermodynamic and dynamic contributions are equally crucial in determining precipitation changes in this event.

# Chapter 6 Discussion and conclusion

In this chapter, we first discuss the limitations and potential impacts of extreme events selection and attribution approach on results, as well as uncertainties of model simulations. The main conclusions of this study are then recapitulated, followed by a brief summarize of innovation and significance of this thesis. Finally, we present a research outlook based on the current studies of extreme rainfall event attribution and the latest IPCC AR6 report.

## 6.1 Discussion

### 6.1.1 Definition and selection of extreme events

As mentioned in Chapter 1.1.1, there are dozens of indices used to define extreme precipitation, in terms of intensity, frequency, and duration. In this study, we used 95$^{th}$ percentile thresholds as the definition of extreme rainfall. Meanwhile, we define these events over a long time period (1998-2018) such that the natural variability is properly incorporated. In this way, over 200 extreme rainfall events were identified. These events, however, may not be detected by using other indices. In other words, how the metrics being used can influence how extreme rainfall case selection, the result of which might affect an inference on human impacts. More extreme rainfall is found to be more sensitive to anthropogenic warming (Min et al., 2011; Zhang et al., 2017). Therefore, one should be more careful when comparing attribution results to those from previous studies, even for the same region.

In the multi-case attribution (see Chapter 3), extreme precipitation events are selected based on the TRMM 3B42 product due to unavailable in-situ data with dense spatial and temporal coverage. However, TRMM 3B42 has biases in rainfall estimates, such as overestimating heavy rainfall over China (Zhao & Yatagai, 2014; Huang et al., 2018) or failing to capture the

spatial-temporal evolution of storm rainfall (Anjum et al., 2016). Some intense rainfall in reality might not appear or is simply displaced out of the target region in TRMM 3B42. Nonetheless, we evaluated the simulations of TRMM-based extremes against rain gauge-based observations before conducting attribution analysis to ensure accurate simulations.

### 6.1.2 Model uncertainties

One of the biggest challenges in this attribution study is the capability of WRF for reproducing some extreme events, particularly precipitation extremes associated with convection (Zhang et al., 2017). Though we used a 2km × 2km convection-resolving resolution in the simulations, the results are still sensitive to different parameterization schemes (Singh & O'Gorman, 2014). Precipitation characteristics are predominantly sensitive to cumulus parameterizations and less to PBL and microphysics schemes (Crétat et al., 2012). Furthermore, the model bias for heavy precipitation over Southern Great Plains can be significantly reduced by using optimal input parameters in the KF scheme (Yang et al., 2012). This optimization can be applied to our simulations for additional research to check whether it is transferable to the PRD region, but it is beyond the scope of this study. The rainfall simulations are not only sensitive to physical schemes but also the forcing data. Take the pre-monsoon heavy precipitation event as an example, its simulation using ERA5 as IBCs performs better than using ERA-Interim reanalysis due to the better representation of synoptic conditions in ERA5 data (Hoffmann et al., 2019). Apart from these factors, the WRF model bias could be owing to the simulations not fully considering aerosol effects (Yun et al., 2020), given the relatively high aerosol concentrations in Guangzhou city. Nonetheless, we ran a variety of sensitivity tests to reduce model biases, such as applying the spectral nudging technique to improve rainfall simulation despite being artificial to some extent (see details in Chapter 2).

Another source of uncertainty comes from the CMIP5 global model bias, especially in circulation simulations. In Chapter 4, we compared human-induced synoptic anomalies from a seven-model ensemble to results from Laua & Kim (2015). The comparison suggests that the difference is mainly from human-related horizontal wind anomalies, whereas greenhouse-gas warming is consistent. This is consistent with the fact that there exists a larger range of uncertainties across CMIP5 models in simulating the large-scale circulation (Pfahl et al., 2017), and a lack of reliable reanalysis products to constrain their dynamics in models (Tandon et al., 2018). Differences in wind anomalies between the two studies are probably due to the use of different CMIP5 GCMs. In fact, there are lots of approaches for selecting the subset of CMIP5 models from which anthropogenic signals are extracted (McSweeney et al., 2015). This study chose an ensemble of seven GCMs with varying parameters of each model, based on their ability to simulate surface temperature and its historical trend. The anthropogenic signal may differ from this if alternative selection methods are applied. This potential uncertainty in attribution assessments could be estimated through Bayesian methods as reported by Paciorek et al. (2018). Further experiments with different sets of CMIP5 or CMIP6 models are necessary for validation.

### 6.1.3 Limitations on PGW method

The shortcoming of PGW is that it imposes unrealistic constraints on interseasonal and internal variability. In this method, perturbations due to monthly anthropogenic forcing as inferred from GCMs were removed from 6-hourly forcing data in WRF, assuming that those forcing remain constant over a month. While this assumption is plausible for anthropogenic warming with relatively small changes measured at that scale, it may introduce errors for more variable wind anomalies caused by human influences. This bias can be inferred from the comparison of

anomalies from GCMs and WRF simulations (see Figure 4.7 in Chapter 4). More evaluations of the PGW approach can be carried out to further fine-tune this method.

### 6.1.4 Moisture budget decomposition

We have assessed the thermodynamic and dynamic contributions to human-forced extreme rainfall changes using the moisture budget equation. There are some caveats in this approach. First, the thermodynamic term involves human-caused specific humidity changes only with the fixed wind circulations. Seager et al. (2010) previously checked thermodynamic contributions to precipitation anomaly due to changes in specific and relative humidity independently, and concluded that increased specific humidity explains the whole thermodynamic contribution to rainfall change for all regions and seasons. This allows the assumption of constant relative humidity under warming. It was also noted that moisture amounts can be partly altered by circulation changes owing to global warming, which can be seen from the difference between DTQ and DTQW runs in specific event attribution (see Chapters 4 and 5). Thus, it is impossible to clearly isolate thermodynamic contribution from dynamic contribution. Despite such limitations, the moisture budget decomposition is useful for analyzing the cause of rainfall variations. Using this method, a larger contribution of the dynamic component was found for PRD extreme rainfall, which is consistent with the results of SC rainfall using the CESM model (Li et al., 2019). However, there are also studies showing negative dynamic contributions to the tropical rainfall extremes based on CMIP3 outputs (Chou et al., 2012). These previous results indicate the spatial spread of dynamic effects, which might be also related to the global model bias, limited sample size, and different methods for extracting human-induced warming signals. Thus, more examinations of dynamic effects on regional extreme rainfall are necessary.

Second, the thermodynamic and dynamic contributions can be further separated into two parts: changes in moisture advection and moisture divergence or convergence. This decomposition

has been done, and enhanced moisture convergence from dynamic changes is found to be the primary cause of the occurrence of extreme rainfall in Indian (Roxy et al., 2017). Horizontal advection, on the other hand, is crucial for the decrease in very extreme rainfall in the subtropics (Chen et al., 2019). Explaining all of these processes will help disentangle the involved physical mechanisms. In this regard, more research into the role of these components in human-induced changes in the PRD extremes is warranted.

Last but not least, the transient eddy term is neglected in the breakdown of the moisture budget in this study, due to its small contribution (Lee et al., 2017). Nonetheless, transient eddies changes can drive changes in wind circulation and moisture fluxes as a result of global warming, which remains to be studied further to acquire a deeper understanding of hydrological cycle changes (Seager et al., 2010, 2014).

### 6.1.5 Other uncertainties involved

Precipitation variations are not only controlled by anthropogenic factors but also by the climate variability. For example, the El Niño Southern Oscillation (ENSO) - the main control of rainfall inter-annual variability – accounts for the extreme rainfall in May 2016 over Yangtze River Valley in China (Li et al., 2018); while ENSO has little impacts on Rx5day extreme rainfall in Southeast Australia (King et al., 2013). The contribution of such climate variability to the PRD extremes remains unclear. Although this study focuses on anthropogenic impacts on extremes, we did not exclude extreme rainfall cases occurred during El Niño/La Niña years. This would have little effect on the results because we ran parallel experiments with the main difference being human forcing.

The magnitude of extreme rainfall response to human activities differs from case to case and is dependent on several factors, such as weather systems and types of extremes, models utilized and threshold for extreme events. For instance, our results indicate that anthropogenic warming

has intensified the 2013 PRD winter rainstorm caused by cold air intrusion by 17%, with an interquartile range of 15%-20%, but reduced the pre-monsoon heavy rainfall in western PRD by about 70%; Wang et al. (2018) concluded that it contributed to the 2017 Hurricane Harvey's extreme rainfall by about 20%, with a range of 13%-37%. This discrepancy in rainfall intensity changes is due to their different synoptic systems. Besides the intensity, anthropogenic forcing has led to a 10%-30% increase in the frequency of extreme rainfall in MJJAS using WRF simulations. This differs from (Burke et al., 2016) in which the probability of the PRD's rainfall that greater than extreme rainfall in May 2015 was enhanced by 66% $\pm$ 19% based on GCMs. Multiple factors including differences in model ability to simulate rainfall, attribution methods, thresholds used to define extreme rainfall as well as time periods appear to have contributed to this discrepancy, however a detailed discussion is beyond the scope of this thesis. More research on quantitatively examine extreme precipitation responses to human forcing at various regions is in urgent need. Last but not least, the effect of sampling variability related to limited extreme events and model ensemble sizes on attribution estimates can be quantified using a statistical framework as presented by Paciorek et al. (2018).

## 6.2 Conclusion

This study has attributed multiple extreme precipitation events over PRD in different seasons to anthropogenic influences. The main findings are summarized in chapter order by responding to the objectives proposed at the beginning of this thesis.

(1) In the multi-case study, the intensity and location of rainfall centers, as well as the associated synoptic conditions, are well replicated by the WRF model. The attribution results are outlined as follows:

- Based on simulations of the selected 40 events, human activities have intensified daily precipitation by 10% up to 85% over inland and suppressed the coastal rainfall by 25%

at most, for a 0.9 K warming troposphere (1000-500hPa) over PRD for both MJJAS and non-MJJAS seasons. Notably, the magnitude of heavy rainfall ($\geq 95^{th}$ percentile or rain rates above ~80 mm per day) in MJJAS increases at a rate of 8-9.5% (roughly CC scaling), whereas the change in non-MJJAS peaks at 12.4% (nearly super-CC scaling); their frequencies have increased by 10%-30% in MJJAS and 20%-40% in non-MJJAS as a result of human influence.

- The involved mechanisms are examined from the thermodynamic (TH) and dynamic (DY) perspectives. From TH's view, anthropogenic warming leads to enhanced precipitable water and moisture transport from SCS towards the inland that feeds the PRD heavy rainfall in both seasons. While DY contribution to rainfall change differs with seasons. In MJJAS, human influences have led to stronger low-level southerly winds as well as more frequent strong vertical motion and less weak motion. In the non-MJJAS season, there is a strengthened low-level wind convergence accompanied by more (less) frequent updrafts (downdrafts), which is likely the reason for the super-CC increase of heavy rainfall. Based on regional average, the intensification of daily-mean rainfall is substantially contributed by the TH term for both seasons and the DY term contributing as a secondary factor for non-MJJAS cases. On the contrary, the DY term dominates the $95^{th}$ percentile rainfall increase. These findings all point to the non-MJJAS receiving more intense and frequent heavy rainfall modulation due to human activities than MJJAS, which is mostly attributed to the DY contribution.

We then focused on human-forced DY and TH effects on two specific extreme rainfall events in different seasons over PRD.

(2) One is a rare wintertime extreme rainfall event in 2013 caused by cold-air intrusion. Ensemble of simulation results closely matches the observed precipitation. The quantitative attribution analysis of this event shows that:

- Human-induced TH forcing alone contributed to an 11% increase in the mean rainfall of this event for 1.2 K near-surface warming on average, whereas the sum of DY and TH (hereafter ALL) forcing contributed to a 17% increase for 2 K warming. Both TH and ALL forcing have led to a roughly CC scaling for the increase in mean rainfall intensity and a super-CC increase for the 95$^{th}$ and 99$^{th}$ percentiles (13%-21%), with ALL forcing producing relatively higher increments. The rainfall probability is most likely to be enhanced by 10% K$^{-1}$ due to TH forcing, and it increases by 10% K$^{-1}$ and 36% K$^{-1}$ due to ALL forcing. Differences between results from the two forcings reflect the DY effect on this event.

- Under TH forcing only, an anomalous low-level thermal contrast exists between the SCS and the China continents, facilitating northward moisture transport and increasing cold-front intensity over PRD. Together with the help of low-level convergences and stronger updrafts, the rainfall increased as a result. Under ALL forcing, thermal contrasts became more noticeable, which favors anomalous southerly winds in PRD and thus dramatically strengthens low-level wind convergence. The anomalous wind pattern in turn intensified the front system and ascending motions, resulting in a higher amplitude of rainfall change compared to TH-forced changes. In general, the TH and DY contribute equally to 4-day mean rainfall increases. While the wind-related DY contribution accounts for extreme rainfall changes, with the TH contribution being limited and negligible.

(3) Another heavy rainfall event studied in detail is one that occurred in May 2016. The average of a large ensemble captured the observed rainband location with a reasonable intensity. We finally arrived at the attribution results:

- Unlike previous studies, human-related TH forcing has reduced the intensity of the rainfall center in the eastern PRD by 70% or more, despite the enhanced moisture amount with 0.8-1 K low-level warming. Meanwhile, precipitation over southwestern PRD was

enhanced as high as 25%-40% by TH forcing. In contrast, the ALL forcing alleviates the TH-forced rainfall reduction and slightly amplifies the rainfall increase. During this pre-monsoon event, the frequency of rainfall is most likely to decrease with warming at a rate of 20% $K^{-1}$ and 16% $K^{-1}$ under the TH and ALL forcing, respectively.

- The reason for rainfall reduction under both forcing climates is that fast warming at lower layers over the eastern PRD resulted in decreased relative humidity and thus increased CIN, as well as the weakened front. Furthermore, the TH-induced more striking rainfall decrease is primarily due to the higher CIN and weaker updrafts, given the similar frontal intensity and CAPE between TH and ALL forcing. On the other hand, rainfall increases in the southwestern PRD can be attributed to the substantial increases in both humidities and intensified front. The amplified intensification of rainfall due to ALL forcing reflects a positive DY effect on this pre-monsoon rainfall. Moreover, both the TH and DY effects are important in determining heavy rainfall change in this event. This event attribution case indicates that human-caused warming may not always intensify PRD precipitation extremes, highlighting the critical need for more studies regarding the role of weather type, seasons of occurrence and background circulation, and so on.

## 6.3 Innovation and significance

This thesis focuses on the attribution of the PRD rainfall extremes to human influence and takes one step forward towards revealing the underlying physical mechanisms. Chapter 3 aims to address the seasonal responses of extreme precipitation to human impacts by conducting multi-case attribution. Chapter 4 and 5 present two case studies aiming to further analyze such human impacts and physical processes involved. The innovation and significance of this thesis can be summed up in two parts:

(1) We firstly applied the reversed PGW approach to construct a “counterfactual” climate in PRD by removing human forcings from the initial and boundary conditions in the WRF model (see details in Chapter 2.4.3). This method was originally introduced by Haustein et al. (2016) though it was only applied to SST patterns. Later, Oldenborgh et al. (2018) have tried but failed to apply this method in rainfall attribution analysis as the regional model they used is unable to capture extreme precipitation well. Our findings clearly show human influences on extreme rainfall in PRD, implying that this technique could be used to attribute extreme weather events, for instance, heatwaves in this region.

(2) Previous studies have attributed some specific events in China to anthropogenic forcing, as mentioned in Chapter 1.3. We extend previous research by attributing multiple extreme events that occurred in different seasons in order to investigate the seasonal responses to such forcing. Previous studies revealed that heavy rainfall changes on a global basis are mostly contributed by thermodynamic effects related to moisture changes due to human forcing, with dynamic contributions being negligible; however, there are large uncertainties at regional scales (see Chapter 1.2.3.2). Our findings highlight the importance of dynamic effects associated with intense updrafts and low-level wind convergences. Besides, results of two case studies expand our knowledge of how human-induced warming may or may not always enhance PRD heavy rainfall. Overall, this work complements the attribution map and ultimately provides invaluable insights for the PRD's future climate resilience.

## 6.4 Research outlook

### 6.4.1 Use of CMIP6 data

In this study, we obtained human forcing from CMIP5 models. The new generation CMIP6 models have been released, which have higher horizontal and vertical resolutions and improved

parameterization schemes for physical and biogeochemical processes (Eyring et al., 2016). Recent studies have examined CMIP6 models' capability of reproducing the current climate (Bock et al., 2020; Dunne et al., 2020). Compared to CMIP5 models, the average of a large number of CMIP6 models tracks observed surface and vertical warming better, especially in the 21st century (Bock et al., 2020). Although the overall performances of CMIP5 and CMIP6 models in simulating global precipitation extremes are similar (IPCC, 2021), the latter is more representative of the observed extreme precipitation over China (Zhu et al., 2020). Also, as reported in the IPCC AR6, CMIP6 models can capture the large-scale tropospheric circulation (IPCC, 2021). The improvements of CMIP6 models may provide us with greater confidence in attributing temperature and precipitation changes to human influence. In this regard, we intend to use CMIP6-projected human forcing and re-run this study in the follow-up work. However, it should be noted that greenhouse gas concentrations are updated in future scenarios and forcing datasets in CMIP6 models (Wyser et al., 2020). Therefore, it is difficult to directly compare the greenhouse-gas effect in CMIP5 to that in CMIP6 models. In other words, caution should be exercised when interpreting the differences between the results of this study and future work using CMIP6.

### 6.4.2 Attribution of sub-daily rainfall extremes

This study focused on daily rainfall extremes. Short-duration or sub-daily rainfall extremes are also important as they can cause flash flooding. Observed changes in sub-daily extremes under human-related greenhouse warming have been examined (Lenderink et al., 2017; Ali et al., 2018; Guerreiro et al., 2018; Chen et al., 2021). The common conclusion reached by these studies is that sub-daily rainfall extremes intensify with warming following the CC rate at most locations worldwide, while increasing at super-CC rates in some regions. Such as in northern Australia, hourly extreme rainfall changes exceed three times of CC rate, which is not

explained by natural variability (Guerreiro et al., 2018). However, there is limited modeling evidence of variations in sub-daily extremes and their responses to human influences under warmer scenarios (Fowler et al., 2021; IPCC, 2021). We first plan to carry out a 10-year WRF simulation over the PRD region, and then assess the long-term behavior of hourly or 6-hourly extreme precipitation indices to check whether the observed relationship between those extremes and dew-point temperatures still holds. Furthermore, we apply the pseudo global warming method to attribute the sub-daily heavy rainfall-derived floods to external variability. The findings aim to provide more modeling understanding of extreme precipitation at sub-daily scales and insights into human-related climate change adaptation.

### 6.4.3 Attribution of TC-induced rainfall

Observational records have found that the probability and proportion of major TC intensities has increased over the past four decades (Kossin et al., 2020). These changes, however, cannot be explained by natural variability alone (Bhatia et al., 2019). Studies on attribution of TC-related rainfall events projected that the average and maximum rain rates increase in a warming climate; the growing rate reaches the CC scaling (~7% $K^{-1}$) and even exceeds that rate in some regions because of enhanced low-level moisture convergence caused by the intensification of TC winds (Liu et al., 2019). However, there is significant uncertainty in the projected changes of TC activities and also the magnitude of the related rainfall changes due to the uncertainty in atmospheric circulations and storm dynamics (IPCC 2021). A high-resolution regional model is needed to reduce these uncertainties, and attribution analysis of TC-caused extreme rainfall and the physical mechanisms involved will be examined in the future work.

### 6.4.4 Impacts of anthropogenic aerosol forcing

We have detected the anthropogenic influence (greenhouse warming) on PRD rainfall extremes. However, the concentration of anthropogenic aerosols (AA) has increased rapidly in this region

during the past 50 years, yet its impact on those simulated extremes is short of study. Previous research illustrates that AA forcing reduces the probability of heavy monsoon rainfall events by reducing atmospheric warming (Zhou et al., 2020) and weakening the South Asian summer monsoon system (Bollasina et al., 2011). A more recent study argues that AA reduced in the future that allows heavy rainfall in the Yangtze River to occur more frequently (Zhou et al., 2021). But they used GCMs in which internal variability may not be excluded completely, large ensemble simulations using high-resolution regional models are required for the detection and attribution of AA forcing on rainfall extremes. Physical mechanisms, such as AA-cloud-rainfall interactions, deserve further study.

# Bibliography


Alexander, L. V., Zhang, X., Peterson, T. C., Caesar, J., Gleason, B., Klein Tank, A. M. G., Haylock, M., Collins, D., Trewin, B., Rahimzadeh, F., Tagipour, A., Rupa Kumar, K., Revadekar, J., Griffiths, G., Vincent, L., Stephenson, D. B., Burn, J., Aguilar, E., Brunet, M., … Vazquez-Aguirre, J. L. (2006). Global observed changes in daily climate extremes of temperature and precipitation. *Journal of Geophysical Research Atmospheres*. https://doi.org/10.1029/2005JD006290

Ali, H., Fowler, H. J., & Mishra, V. (2018). Global Observational Evidence of Strong Linkage Between Dew Point Temperature and Precipitation Extremes. *Geophysical Research Letters*. https://doi.org/10.1029/2018GL080557

Ali, H., & Mishra, V. (2018). Contributions of Dynamic and Thermodynamic Scaling in Subdaily Precipitation Extremes in India. *Geophysical Research Letters*. https://doi.org/10.1002/2018GL077065

Allan, R. P., & Soden, B. J. (2008). Atmospheric warming and the amplification of precipitation extremes. *Science*. https://doi.org/10.1126/science.1160787

Allan, R. P., Soden, B. J., John, V. O., Ingram, W., & Good, P. (2010). Current changes in tropical precipitation. *Environmental Research Letters*. https://doi.org/10.1088/1748-9326/5/2/025205

Allen, M. (2003). Liability for climate change. In *Nature*. https://doi.org/10.1038/421891a

Allen, M. R., & Ingram, W. J. (2002). Constraints on future changes in climate and the hydrologic cycle. In *Nature*. https://doi.org/10.1038/nature01092

Anjum, M. N., Ding, Y., Shangguan, D., Ijaz, M. W., & Zhang, S. (2016). Evaluation of High-Resolution Satellite-Based Real-Time and Post-Real-Time Precipitation Estimates during 2010 Extreme Flood Event in Swat River Basin, Hindukush Region. *Advances in Meteorology*. https://doi.org/10.1155/2016/2604980

Asadieh, B., & Krakauer, N. Y. (2015). Global trends in extreme precipitation: Climate models versus observations. *Hydrology and Earth System Sciences*. https://doi.org/10.5194/hess-19-877-2015

Banacos, P. C., & Schultz, D. M. (2005). The use of moisture flux convergence in forecasting convective initiation: Historical and operational perspectives. *Weather and Forecasting*. https://doi.org/10.1175/WAF858.1

Berg, P., Haerter, J. O., Thejll, P., Piani, C., Hagemann, S., & Christensen, J. H. (2009). Seasonal characteristics of the relationship between daily precipitation intensity and surface temperature. *Journal of Geophysical Research Atmospheres*. https://doi.org/10.1029/2009JD012008

Bhatia, K. T., Vecchi, G. A., Knutson, T. R., Murakami, H., Kossin, J., Dixon, K. W., &

Whitlock, C. E. (2019). Recent increases in tropical cyclone intensification rates. *Nature Communications*. https://doi.org/10.1038/s41467-019-08471-z

Bock, L., Lauer, A., Schlund, M., Barreiro, M., Bellouin, N., Jones, C., Meehl, G. A., Predoi, V., Roberts, M. J., & Eyring, V. (2020). Quantifying Progress Across Different CMIP Phases With the ESMValTool. *Journal of Geophysical Research: Atmospheres*. https://doi.org/10.1029/2019JD032321

Bollasina, M. A., Ming, Y., & Ramaswamy, V. (2011). Anthropogenic aerosols and the weakening of the south asian summer monsoon. *Science*. https://doi.org/10.1126/science.1204994

Borodina, A., Fischer, E. M., & Knutti, R. (2017). Models are likely to underestimate increase in heavy rainfall in the extratropical regions with high rainfall intensity. *Geophysical Research Letters*. https://doi.org/10.1002/2017GL074530

Bougeault, P., & Lacarrere, P. (1989). Parameterization of orography-induced turbulence in a mesobeta-scale model. *Monthly Weather Review*. https://doi.org/10.1175/1520-0493(1989)117<1872:POOITI>2.0.CO;2

Burke, C., & Stott, P. (2017). Impact of anthropogenic climate change on the East Asian summer monsoon. *Journal of Climate*. https://doi.org/10.1175/JCLI-D-16-0892.1

Burke, C., Stott, P., Sun, Y., & Ciavarella, A. (2016). Attribution of extreme rainfall in Southeast China during May 2015. *Bulletin of the American Meteorological Society*. https://doi.org/10.1175/BAMS-D-16-0144.1

Chen, G., Norris, J., David Neelin, J., Lu, J., Ruby Leung, L., & Sakaguchi, K. (2019). Thermodynamic and dynamic mechanisms for hydrological cycle intensification over the full probability distribution of precipitation events. *Journal of the Atmospheric Sciences*. https://doi.org/10.1175/JAS-D-18-0067.1

Chen, J., Dai, A., Zhang, Y., & Rasmussen, K. L. (2020). Changes in convective available potential energy and convective inhibition under global warming. *Journal of Climate*. https://doi.org/10.1175/JCLI-D-19-0461.1

Chen, M., Shi, W., Xie, P., Silva, V. B. S., Kousky, V. E., Higgins, R. W., & Janowiak, J. E. (2008). Assessing objective techniques for gauge-based analyses of global daily precipitation. *Journal of Geophysical Research Atmospheres*. https://doi.org/10.1029/2007JD009132

Chen, S., Li, W. B., Du, Y. D., Mao, C. Y., & Zhang, L. (2015). Urbanization effect on precipitation over the Pearl River Delta based on CMORPH data. *Advances in Climate Change Research*. https://doi.org/10.1016/j.accre.2015.08.002

Chen, Y., Li, W., Jiang, X., Zhai, P., & Luo, Y. (2021). Detectable intensification of hourly and daily scale precipitation extremes across eastern China. *Journal of Climate*. https://doi.org/10.1175/JCLI-D-20-0462.1

Cheong, W. K., Timbal, B., Golding, N., Sirabaha, S., Kwan, K. F., Cinco, T. A., Archevarahuprok, B., Vo, V. H., Gunawan, D., & Han, S. (2018). Observed and modelled temperature and precipitation extremes over Southeast Asia from 1972 to 2010.

*International Journal of Climatology*. https://doi.org/10.1002/joc.5479

Choi, G., Collins, D., Ren, G., Trewin, B., Baldi, M., Fukuda, Y., Afzaal, M., Pianmana, T., Gomboluudev, P., Huong, P. T. T., Lias, N., Kwon, W. T., Boo, K. O., Cha, Y. M., & Zhou, Y. (2009). Changes in means and extreme events of temperature and precipitation in the Asia-Pacific Network region, 1955-2007. *International Journal of Climatology*. https://doi.org/10.1002/joc.1979

Chou, C., Chen, C. A., Tan, P. H., & Chen, K. T. (2012). Mechanisms for global warming impacts on precipitation frequency and intensity. *Journal of Climate*. https://doi.org/10.1175/JCLI-D-11-00239.1

Chou, C., Chiang, J. C. H., Lan, C. W., Chung, C. H., Liao, Y. C., & Lee, C. J. (2013). Increase in the range between wet and dry season precipitation. *Nature Geoscience*. https://doi.org/10.1038/ngeo1744

Chou, C., Neelin, J. D., Chen, C. A., & Tu, J. Y. (2009). Evaluating the "rich-get-richer" mechanism in tropical precipitation change under global warming. *Journal of Climate*. https://doi.org/10.1175/2008JCLI2471.1

Christensen, J. H., & Christensen, O. B. (2003). Severe summertime flooding in Europe. *Nature*. https://doi.org/10.1038/421805a

Cook, B. I., Mankin, J. S., & Anchukaitis, K. J. (2018). Climate Change and Drought: From Past to Future. In *Current Climate Change Reports*. https://doi.org/10.1007/s40641-018-0093-2

Crétat, J., Pohl, B., Richard, Y., & Drobinski, P. (2012). Uncertainties in simulating regional climate of Southern Africa: Sensitivity to physical parameterizations using WRF. *Climate Dynamics*. https://doi.org/10.1007/s00382-011-1055-8

Dai, A. (2001a). Global precipitation and thunderstorm frequencies. Part II: Diurnal variations. *Journal of Climate*. https://doi.org/10.1175/1520-0442(2001)014<1112:GPATFP>2.0.CO;2

Dai, A. (2001b). Global precipitation and thundertstorm frequencies. Part I: Seasonal and interannual variations. *Journal of Climate*. https://doi.org/10.1175/1520-0442(2001)014<1092:GPATFP>2.0.CO;2

Dai, Aiguo. (2006). Precipitation characteristics in eighteen coupled climate models. *Journal of Climate*. https://doi.org/10.1175/JCLI3884.1

Dai, Aiguo, Rasmussen, R. M., Liu, C., Ikeda, K., & Prein, A. F. (2020). A new mechanism for warm-season precipitation response to global warming based on convection-permitting simulations. *Climate Dynamics*. https://doi.org/10.1007/s00382-017-3787-6

Dai, Aiguo, & Trenberth, K. E. (2004). The diurnal cycle and its depiction in the community climate system model. *Journal of Climate*. https://doi.org/10.1175/1520-0442(2004)017<0930:TDCAID>2.0.CO;2

Day, J. A., Fung, I., & Liu, W. (2018). Changing character of rainfall in eastern China, 1951–2007. *Proceedings of the National Academy of Sciences of the United States of America*.

https://doi.org/10.1073/pnas.1715386115

Dee, D. P., Uppala, S. M., Simmons, A. J., Berrisford, P., Poli, P., Kobayashi, S., Andrae, U., Balmaseda, M. A., Balsamo, G., Bauer, P., Bechtold, P., Beljaars, A. C. M., van de Berg, L., Bidlot, J., Bormann, N., Delsol, C., Dragani, R., Fuentes, M., Geer, A. J., … Vitart, F. (2011). The ERA-Interim reanalysis: Configuration and performance of the data assimilation system. *Quarterly Journal of the Royal Meteorological Society*. https://doi.org/10.1002/qj.828

Dey, R., Lewis, S. C., Arblaster, J. M., & Abram, N. J. (2019). A review of past and projected changes in Australia's rainfall. In *Wiley Interdisciplinary Reviews: Climate Change*. https://doi.org/10.1002/wcc.577

Diffenbaugh, N. S., Swain, D. L., Touma, D., & Lubchenco, J. (2015). Anthropogenic warming has increased drought risk in California. *Proceedings of the National Academy of Sciences of the United States of America*. https://doi.org/10.1073/pnas.1422385112

Ding, Y., Wang, Z., & Sun, Y. (2008). Inter-decadal variation of the summer precipitation in East China and its association with decreasing Asian summer monsoon. Part I: Observed evidences. *International Journal of Climatology*. https://doi.org/10.1002/joc.1615

Donat, M. G., Lowry, A. L., Alexander, L. V., O'Gorman, P. A., & Maher, N. (2016). More extreme precipitation in the worldâ €TM s dry and wet regions. *Nature Climate Change*. https://doi.org/10.1038/nclimate2941

Dong, L., Leung, L. R., Lu, J., & Gao, Y. (2019). Contributions of Extreme and Non-Extreme Precipitation to California Precipitation Seasonality Changes Under Warming. *Geophysical Research Letters*. https://doi.org/10.1029/2019GL084225

Dong, L., Leung, L. R., & Song, F. (2018). Future Changes of Subseasonal Precipitation Variability in North America During Winter Under Global Warming. *Geophysical Research Letters*, *45*(22), 12,467-12,476. https://doi.org/10.1029/2018GL079900

Dong, S., Sun, Y., Li, C., Zhang, X., Min, S. K., & Kim, Y. H. (2021). Attribution of extreme precipitation with updated observations and CMIP6 simulations. *Journal of Climate*. https://doi.org/10.1175/JCLI-D-19-1017.1

Duan, W., He, B., Nover, D., Fan, J., Yang, G., Chen, W., Meng, H., & Liu, C. (2016). Floods and associated socioeconomic damages in China over the last century. *Natural Hazards*. https://doi.org/10.1007/s11069-016-2207-2

Dunn, R. J. H., Alexander, L. V., Donat, M. G., Zhang, X., Bador, M., Herold, N., Lippmann, T., Allan, R., Aguilar, E., Barry, A. A., Brunet, M., Caesar, J., Chagnaud, G., Cheng, V., Cinco, T., Durre, I., de Guzman, R., Htay, T. M., Wan Ibadullah, W. M., … Bin Hj Yussof, M. N. A. (2020). Development of an Updated Global Land In Situ-Based Data Set of Temperature and Precipitation Extremes: HadEX3. *Journal of Geophysical Research: Atmospheres*. https://doi.org/10.1029/2019JD032263

Dunne, J. P., Horowitz, L. W., Adcroft, A. J., Ginoux, P., Held, I. M., John, J. G., Krasting, J. P., Malyshev, S., Naik, V., Paulot, F., Shevliakova, E., Stock, C. A., Zadeh, N., Balaji, V., Blanton, C., Dunne, K. A., Dupuis, C., Durachta, J., Dussin, R., … Zhao, M. (2020). The GFDL Earth System Model Version 4.1 (GFDL-ESM 4.1): Overall Coupled Model

Description and Simulation Characteristics. *Journal of Advances in Modeling Earth Systems*. https://doi.org/10.1029/2019MS002015

Dwyer, J. G., & O'Gorman, P. A. (2017). Changing duration and spatial extent of midlatitude precipitation extremes across different climates. *Geophysical Research Letters*. https://doi.org/10.1002/2017GL072855

Easterling, D. R., Evans, J. L., Groisman, P. Y., Karl, T. R., Kunkel, K. E., & Ambenje, P. (2000). Observed variability and trends in extreme climate events: A brief review. In *Bulletin of the American Meteorological Society*. https://doi.org/10.1175/1520-0477(2000)081<0417:OVATIE>2.3.CO;2

Emori, S., & Brown, S. J. (2005). Dynamic and thermodynamic changes in mean and extreme precipitation under changed climate. *Geophysical Research Letters*. https://doi.org/10.1029/2005GL023272

Endo, H., & Kitoh, A. (2014). Thermodynamic and dynamic effects on regional monsoon rainfall changes in a warmer climate. *Geophysical Research Letters*. https://doi.org/10.1002/2013GL059158

Evans, J. P., Ekström, M., & Ji, F. (2012). Evaluating the performance of a WRF physics ensemble over South-East Australia. *Climate Dynamics*. https://doi.org/10.1007/s00382-011-1244-5

Eyring, V., Bony, S., Meehl, G. A., Senior, C. A., Stevens, B., Stouffer, R. J., & Taylor, K. E. (2016). Overview of the Coupled Model Intercomparison Project Phase 6 (CMIP6) experimental design and organization. *Geoscientific Model Development*. https://doi.org/10.5194/gmd-9-1937-2016

Fan, J., Wang, Y., Rosenfeld, D., & Liu, X. (2016). Review of aerosol-cloud interactions: Mechanisms, significance, and challenges. In *Journal of the Atmospheric Sciences*. https://doi.org/10.1175/JAS-D-16-0037.1

Fischer, E. M., & Knutti, R. (2015). Anthropogenic contribution to global occurrence of heavy-precipitation and high-temperature extremes. *Nature Climate Change*. https://doi.org/10.1038/nclimate2617

Fischer, E. M., & Knutti, R. (2016). Observed heavy precipitation increase confirms theory and early models. In *Nature Climate Change*. https://doi.org/10.1038/nclimate3110

Fowler, H. J., Lenderink, G., Prein, A. F., Westra, S., Allan, R. P., Ban, N., Barbero, R., Berg, P., Blenkinsop, S., Do, H. X., Guerreiro, S., Haerter, J. O., Kendon, E. J., Lewis, E., Schaer, C., Sharma, A., Villarini, G., Wasko, C., & Zhang, X. (2021). Anthropogenic intensification of short-duration rainfall extremes. In *Nature Reviews Earth and Environment*. https://doi.org/10.1038/s43017-020-00128-6

Frame, D. J., Rosier, S. M., Noy, I., Harrington, L. J., Carey-Smith, T., Sparrow, S. N., Stone, D. A., & Dean, S. M. (2020). Climate change attribution and the economic costs of extreme weather events: a study on damages from extreme rainfall and drought. *Climatic Change*. https://doi.org/10.1007/s10584-020-02729-y

Fu, G., Yu, J., Yu, X., Ouyang, R., Zhang, Y., Wang, P., Liu, W., & Min, L. (2013). Temporal

variation of extreme rainfall events in China, 1961-2009. *Journal of Hydrology*. https://doi.org/10.1016/j.jhydrol.2013.02.021

Grell, G. A., & Dévényi, D. (2002). A generalized approach to parameterizing convection combining ensemble and data assimilation techniques. *Geophysical Research Letters*. https://doi.org/10.1029/2002GL015311

Greve, P., Orlowsky, B., Mueller, B., Sheffield, J., Reichstein, M., & Seneviratne, S. I. (2014). Global assessment of trends in wetting and drying over land. *Nature Geoscience*. https://doi.org/10.1038/NGEO2247

Groisman, P. Y., & Knight, R. W. (2008). Prolonged dry episodes over the conterminous United States: New tendencies emerging during the last 40 years. *Journal of Climate*. https://doi.org/10.1175/2007JCLI2013.1

Groisman, P. Y., Knight, R. W., Easterling, D. R., Karl, T. R., Hegerl, G. C., & Razuvaev, V. N. (2005). Trends in intense precipitation in the climate record. *Journal of Climate*. https://doi.org/10.1175/JCLI3339.1

Groisman, P. Y., Knight, R. W., & Karl, T. R. (2012). Changes in intense precipitation over the Central United States. *Journal of Hydrometeorology*. https://doi.org/10.1175/JHM-D-11-039.1

Gudmundsson, L., & Seneviratne, S. I. (2016). Anthropogenic climate change affects meteorological drought risk in Europe. *Environmental Research Letters*. https://doi.org/10.1088/1748-9326/11/4/044005

Guerreiro, S. B., Fowler, H. J., Barbero, R., Westra, S., Lenderink, G., Blenkinsop, S., Lewis, E., & Li, X. F. (2018). Detection of continental-scale intensification of hourly rainfall extremes. In *Nature Climate Change*. https://doi.org/10.1038/s41558-018-0245-3

Haerter, J. O., & Berg, P. (2009). Unexpected rise in extreme precipitation caused by a shift in rain type? In *Nature Geoscience*. https://doi.org/10.1038/ngeo523

Haerter, J. O., Berg, P., & Hagemann, S. (2010). Heavy rain intensity distributions on varying time scales and at different temperatures. *Journal of Geophysical Research Atmospheres*. https://doi.org/10.1029/2009JD013384

Hannart, A., Pearl, J., Otto, F. E. L., Naveau, P., & Ghil, M. (2016). Causal counterfactual theory for the attribution of weather and climate-related events. *Bulletin of the American Meteorological Society*. https://doi.org/10.1175/BAMS-D-14-00034.1

Hardwick Jones, R., Westra, S., & Sharma, A. (2010). Observed relationships between extreme sub-daily precipitation, surface temperature, and relative humidity. *Geophysical Research Letters*. https://doi.org/10.1029/2010GL045081

Harris, I., Jones, P. D., Osborn, T. J., & Lister, D. H. (2014). Updated high-resolution grids of monthly climatic observations - the CRU TS3.10 Dataset. *International Journal of Climatology*. https://doi.org/10.1002/joc.3711

Haustein, K., Otto, F. E. L., Uhe, P., Schaller, N., Allen, M. R., Hermanson, L., Christidis, N., McLean, P., & Cullen, H. (2016). Real-time extreme weather event attribution with

forecast seasonal SSTs. In *Environmental Research Letters*. https://doi.org/10.1088/1748-9326/11/6/064006

Held, I. M., & Soden, B. J. (2006). Robust responses of the hydrological cycle to global warming. *Journal of Climate*. https://doi.org/10.1175/JCLI3990.1

Herring, S. C., Christidis, N., Hoell, A., Kossin, J. P., Schreck, C. J., & Stott, P. A. (2018). Explaining Extreme Events of 2016 from a Climate Perspective. *Bulletin of the American Meteorological Society*. https://doi.org/10.1175/bams-explainingextremeevents2016.1

Hersbach, H., Bell, B., Berrisford, P., Hirahara, S., Horányi, A., Muñoz-Sabater, J., Nicolas, J., Peubey, C., Radu, R., Schepers, D., Simmons, A., Soci, C., Abdalla, S., Abellan, X., Balsamo, G., Bechtold, P., Biavati, G., Bidlot, J., Bonavita, M., … Thépaut, J. N. (2020). The ERA5 global reanalysis. *Quarterly Journal of the Royal Meteorological Society*. https://doi.org/10.1002/qj.3803

Hoffmann, L., Günther, G., Li, D., Stein, O., Wu, X., Griessbach, S., Heng, Y., Konopka, P., Müller, R., Vogel, B., & Wright, J. S. (2019). From ERA-Interim to ERA5: The considerable impact of ECMWF's next-generation reanalysis on Lagrangian transport simulations. *Atmospheric Chemistry and Physics*. https://doi.org/10.5194/acp-19-3097-2019

Hoffmann, P., & Spekat, A. (2021). Identification of possible dynamical drivers for long-term changes in temperature and rainfall patterns over Europe. *Theoretical and Applied Climatology*. https://doi.org/10.1007/s00704-020-03373-3

Hong, S. (2006). Hongandlim-JKMS-2006. *Journal of the Korean Meteorological Society*.

Howarth, M. E., Thorncroft, C. D., & Bosart, L. F. (2019). Changes in extreme precipitation in the northeast United States: 1979-2014. *Journal of Hydrometeorology*. https://doi.org/10.1175/JHM-D-18-0155.1

Huang, H., Winter, J. M., Osterberg, E. C., Horton, R. M., & Beckage, B. (2017). Total and extreme precipitation changes over the Northeastern United States. *Journal of Hydrometeorology*. https://doi.org/10.1175/JHM-D-16-0195.1

Huang, W., He, X., Yang, Z., Qiu, T., Wright, J. S., Wang, B., & Lin, D. (2018). Moisture Sources for Wintertime Extreme Precipitation Events Over South China During 1979–2013. *Journal of Geophysical Research: Atmospheres*. https://doi.org/10.1029/2018JD028485

Huang, W., Yang, Z., He, X., Lin, D., Wang, B., Wright, J. S., Chen, R., Ma, W., & Li, F. (2019). A possible mechanism for the occurrence of wintertime extreme precipitation events over South China. *Climate Dynamics*. https://doi.org/10.1007/s00382-018-4262-8

Huang, X., Wang, D., Liu, Y., Feng, Z., & Wang, D. (2018). Evaluation of extreme precipitation based on satellite retrievals over China. *Frontiers of Earth Science*. https://doi.org/10.1007/s11707-017-0643-2

Huffman, G. J., Adler, R. F., Bolvin, D. T., Gu, G., Nelkin, E. J., Bowman, K. P., Hong, Y., Stocker, E. F., & Wolff, D. B. (2007). The TRMM Multisatellite Precipitation Analysis (TMPA): Quasi-global, multiyear, combined-sensor precipitation estimates at fine scales.

*Journal of Hydrometeorology*. https://doi.org/10.1175/JHM560.1

Hulme, M. (1992). Rainfall changes in Africa: 1931–1960 to 1961–1990. *International Journal of Climatology*. https://doi.org/10.1002/joc.3370120703

Iacono, M. J., Delamere, J. S., Mlawer, E. J., Shephard, M. W., Clough, S. A., & Collins, W. D. (2008). Radiative forcing by long-lived greenhouse gases: Calculations with the AER radiative transfer models. *Journal of Geophysical Research Atmospheres*. https://doi.org/10.1029/2008JD009944

Janjic, Z. I. (1994). The step-mountain eta coordinate model: further developments of the convection, viscous sublayer, and turbulence closure schemes. *Monthly Weather Review*. https://doi.org/10.1175/1520-0493(1994)122<0927:TSMECM>2.0.CO;2

Jiang, J., Zhou, T., Chen, X., & Zhang, L. (2020). Future changes in precipitation over Central Asia based on CMIP6 projections. *Environmental Research Letters*. https://doi.org/10.1088/1748-9326/ab7d03

Jones, G. S., Stott, P. A., & Christidis, N. (2013). Attribution of observed historical near-surface temperature variations to anthropogenic and natural causes using CMIP5 simulations. *Journal of Geophysical Research Atmospheres*. https://doi.org/10.1002/jgrd.50239

Joshi, M. M., Gregory, J. M., Webb, M. J., Sexton, D. M. H., & Johns, T. C. (2008). Mechanisms for the land/sea warming contrast exhibited by simulations of climate change. *Climate Dynamics*. https://doi.org/10.1007/s00382-007-0306-1

Kain, J. S., & Kain, J. (2004). The Kain - Fritsch convective parameterization: An update. *Journal of Applied Meteorology*. https://doi.org/10.1175/1520-0450(2004)043<0170:TKCPAU>2.0.CO;2

Karl, T. R., & Knight, R. W. (1998). Secular Trends of Precipitation Amount, Frequency, and Intensity in the United States. *Bulletin of the American Meteorological Society*. https://doi.org/10.1175/1520-0477(1998)079<0231:STOPAF>2.0.CO;2

Kharin, V. V., Zwiers, F. W., Zhang, X., & Wehner, M. (2013). Changes in temperature and precipitation extremes in the CMIP5 ensemble. *Climatic Change*. https://doi.org/10.1007/s10584-013-0705-8

Kharin, Viatcheslav V., Zwiers, F. W., Zhang, X., & Hegerl, G. C. (2007). Changes in temperature and precipitation extremes in the IPCC ensemble of global coupled model simulations. *Journal of Climate*. https://doi.org/10.1175/JCLI4066.1

Khouakhi, A., Villarini, G., & Vecchi, G. A. (2017). Contribution of tropical cyclones to rainfall at the global scale. *Journal of Climate*. https://doi.org/10.1175/JCLI-D-16-0298.1

Kim, I. W., Oh, J., Woo, S., & Kripalani, R. H. (2019). Evaluation of precipitation extremes over the Asian domain: observation and modelling studies. *Climate Dynamics*. https://doi.org/10.1007/s00382-018-4193-4

Kim, K. Y., & Kim, B. S. (2020). The effect of regional warming on the East Asian summer monsoon. *Climate Dynamics*. https://doi.org/10.1007/s00382-020-05169-7

Kimura, F., & Kitoh, A. (2007). Downscaling by Pseudo Global Warning Method. In *The Final Report of ICCAP*.

King, A. D., Lewis, S. C., Perkins, S. E., Alexander, L. V., Donat, M. G., Karoly, D. J., & Black, M. T. (2013). Limited evidence of anthropogenic influence on the 2011-12 Extreme Rainfall over Southeast Australia. In *Bulletin of the American Meteorological Society*.

Kirchmeier-Young, M. C., & Zhang, X. (2020). Human influence has intensified extreme precipitation in North America. *Proceedings of the National Academy of Sciences of the United States of America*. https://doi.org/10.1073/pnas.1921628117

Kociuba, G., & Power, S. B. (2015). Inability of CMIP5 models to simulate recent strengthening of the walker circulation: Implications for projections. *Journal of Climate*. https://doi.org/10.1175/JCLI-D-13-00752.1

Konapala, G., Mishra, A. K., Wada, Y., & Mann, M. E. (2020). Climate change will affect global water availability through compounding changes in seasonal precipitation and evaporation. *Nature Communications*. https://doi.org/10.1038/s41467-020-16757-w

Kossin, J. P., Knapp, K. R., Olander, T. L., & Velden, C. S. (2020). Global increase in major tropical cyclone exceedance probability over the past four decades. *Proceedings of the National Academy of Sciences of the United States of America*. https://doi.org/10.1073/pnas.1920849117

Kreienkamp, F., Philip, S. Y., Tradowsky, J. S., Kew, S. F., Lorenz, P., Arrighi, J., Belleflamme, A., Bettmann, T., Caluwaerts, S., Chan, S. C., Ciavarella, A., De Cruz, L., de Vries, H., Demuth, N., Ferrone, A., Fischer, E. M., Fowler, H. J., Goergen, K., Heinrich, D., … L Otto, F. E. (2021). Rapid attribution of heavy rainfall events leading to the severe flooding in Western Europe during July 2021. *World Weather Attribution*.

Kumari, S., Haustein, K., Javid, H., Burton, C., Allen, M. R., Paltan, H., Dadson, S., & Otto, F. E. L. (2019). Return period of extreme rainfall substantially decreases under 1.5 °c and 2.0 °c warming: A case study for Uttarakhand, India. *Environmental Research Letters*. https://doi.org/10.1088/1748-9326/ab0bce

Lau, K. M., & Wu, H. T. (2007). Detecting trends in tropical rainfall characteristic, 1979-2003. *International Journal of Climatology*. https://doi.org/10.1002/joc.1454

Lau, K. M., & Wu, H. T. (2011). Climatology and changes in tropical oceanic rainfall characteristics inferred from Tropical Rainfall Measuring Mission (TRMM) data (1998-2009). *Journal of Geophysical Research Atmospheres*. https://doi.org/10.1029/2011JD015827

Lau, W. K. M., Kim, K. M., & Ruby Leung, L. (2017). Changing circulation structure and precipitation characteristics in Asian monsoon regions: greenhouse warming vs. aerosol effects. *Geoscience Letters*, *4*(1). https://doi.org/10.1186/s40562-017-0094-3

Lau, W. K. M., Wu, H. T., & Kim, K. M. (2013). A canonical response of precipitation characteristics to global warming from CMIP5 models. *Geophysical Research Letters*. https://doi.org/10.1002/grl.50420

Laua, W. K. M., & Kim, K. M. (2015). Robust Hadley circulation changes and increasing global dryness due to CO2 warming from CMIP5 model projections. *Proceedings of the National Academy of Sciences of the United States of America*. https://doi.org/10.1073/pnas.1418682112

Lauer, A., Zhang, C., Elison-Timm, O., Wang, Y., & Hamilton, K. (2013). Downscaling of climate change in the hawaii region using CMIP5 results: On the choice of the forcing fields*. *Journal of Climate*. https://doi.org/10.1175/JCLI-D-13-00126.1

Lee, D., Min, S. K., Fischer, E., Shiogama, H., Bethke, I., Lierhammer, L., & Scinocca, J. F. (2018). Impacts of half a degree additional warming on the Asian summer monsoon rainfall characteristics. *Environmental Research Letters*. https://doi.org/10.1088/1748-9326/aab55d

Lee, D., Min, S. K., Jin, J., Lee, J. W., Cha, D. H., Suh, M. S., Ahn, J. B., Hong, S. Y., Kang, H. S., & Joh, M. (2017). Thermodynamic and dynamic contributions to future changes in summer precipitation over Northeast Asia and Korea: a multi-RCM study. *Climate Dynamics*. https://doi.org/10.1007/s00382-017-3566-4

Lenderink, G., Barbero, R., Loriaux, J. M., & Fowler, H. J. (2017). Super-Clausius-Clapeyron scaling of extreme hourly convective precipitation and its relation to large-scale atmospheric conditions. *Journal of Climate*. https://doi.org/10.1175/JCLI-D-16-0808.1

Lenderink, G., Mok, H. Y., Lee, T. C., & Van Oldenborgh, G. J. (2011). Scaling and trends of hourly precipitation extremes in two different climate zones - Hong Kong and the Netherlands. *Hydrology and Earth System Sciences*. https://doi.org/10.5194/hess-15-3033-2011

Lenderink, Geert, & Van Meijgaard, E. (2008). Increase in hourly precipitation extremes beyond expectations from temperature changes. *Nature Geoscience*. https://doi.org/10.1038/ngeo262

Lewis, S. C., & Karoly, D. J. (2015). Are estimates of anthropogenic and natural influences on Australia's extreme 2010–2012 rainfall model-dependent? *Climate Dynamics*. https://doi.org/10.1007/s00382-014-2283-5

Li, Chun, & Sun, J. (2015). Role of the subtropical westerly jet waveguide in a southern China heavy rainstorm in December 2013. *Advances in Atmospheric Sciences*. https://doi.org/10.1007/s00376-014-4099-y

Li, Chunxiang, Tian, Q., Yu, R., Zhou, B., Xia, J., Burke, C., Dong, B., Tett, S. F. B., Freychet, N., Lott, F., & Ciavarella, A. (2018). Attribution of extreme precipitation in the lower reaches of the Yangtze River during May 2016. *Environmental Research Letters*. https://doi.org/10.1088/1748-9326/aa9691

Li, D., Zhou, T., & Zhang, W. (2019). Extreme precipitation over east asia under 1.5 °c and 2°c global warming targets: A comparison of stabilized and overshoot projections. *Environmental Research Communications*. https://doi.org/10.1088/2515-7620/ab3971

Li, H., Chen, H., & Wang, H. (2017). Effects of anthropogenic activity emerging as intensified extreme precipitation over China. *Journal of Geophysical Research*. https://doi.org/10.1002/2016JD026251

Li, J., Wu, Z., Jiang, Z., & He, J. (2010). Can global warming strengthen the East Asian summer monsoon? *Journal of Climate*. https://doi.org/10.1175/2010JCLI3434.1

Li, P., Guo, Z., Furtado, K., Chen, H., Li, J., Milton, S., Field, P. R., & Zhou, T. (2019). Prediction of heavy precipitation in the eastern China flooding events of 2016: Added value of convection-permitting simulations. *Quarterly Journal of the Royal Meteorological Society*. https://doi.org/10.1002/qj.3621

Li, W., Jiang, Z., Zhang, X., & Li, L. (2018). On the Emergence of Anthropogenic Signal in Extreme Precipitation Change Over China. *Geophysical Research Letters*. https://doi.org/10.1029/2018GL079133

Li, Z., & O'Gorman, P. A. (2020). Response of vertical velocities in extratropical precipitation extremes to climate change. *Journal of Climate*. https://doi.org/10.1175/JCLI-D-19-0766.1

Lin, Z., Dong, B., & Wen, Z. (2020). The effects of anthropogenic greenhouse gases and aerosols on the inter-decadal change of the South China Sea summer monsoon in the late twentieth century. *Climate Dynamics*. https://doi.org/10.1007/s00382-020-05175-9

Liu, Bingjun, Tan, X., Gan, T. Y., Chen, X., Lin, K., Lu, M., & Liu, Z. (2020). Global atmospheric moisture transport associated with precipitation extremes: Mechanisms and climate change impacts. In *Wiley Interdisciplinary Reviews: Water*. https://doi.org/10.1002/wat2.1412

Liu, Binhui, Xu, M., Henderson, M., & Qi, Y. (2005). Observed trends of precipitation amount, frequency, and intensity in China, 1960-2000. *Journal of Geophysical Research D: Atmospheres*. https://doi.org/10.1029/2004JD004864

Liu, C., Ikeda, K., Rasmussen, R., Barlage, M., Newman, A. J., Prein, A. F., Chen, F., Chen, L., Clark, M., Dai, A., Dudhia, J., Eidhammer, T., Gochis, D., Gutmann, E., Kurkute, S., Li, Y., Thompson, G., & Yates, D. (2017). Continental-scale convection-permitting modeling of the current and future climate of North America. *Climate Dynamics*. https://doi.org/10.1007/s00382-016-3327-9

Liu, M., Vecchi, G. A., Smith, J. A., & Knutson, T. R. (2019). Causes of large projected increases in hurricane precipitation rates with global warming. *Npj Climate and Atmospheric Science*. https://doi.org/10.1038/s41612-019-0095-3

Liu, P., Tsimpidi, A. P., Hu, Y., Stone, B., Russell, A. G., & Nenes, A. (2012). Differences between downscaling with spectral and grid nudging using WRF. *Atmospheric Chemistry and Physics*. https://doi.org/10.5194/acp-12-3601-2012

Longobardi, A., & Villani, P. (2010). Trend analysis of annual and seasonal rainfall time series in the Mediterranean area. *International Journal of Climatology*. https://doi.org/10.1002/joc.2001

Luo, Y., Zhang, R., Wan, Q., Wang, B., Wong, W. K., Hu, Z., Jou, B. J. D., Lin, Y., Johnson, R. H., Chang, C. P., Zhu, Y., Zhang, X., Wang, H., Xia, R., Ma, J., Zhang, D. L., Gao, M., Zhang, Y., Liu, X., … Xiao, Y. (2017). The southern China monsoon rainfall experiment (SCMREX). *Bulletin of the American Meteorological Society*. https://doi.org/10.1175/BAMS-D-15-00235.1

Ma, S., Zhou, T., Dai, A., & Han, Z. (2015). Observed changes in the distributions of daily precipitation frequency and amount over China from 1960 to 2013. *Journal of Climate*. https://doi.org/10.1175/JCLI-D-15-0011.1

Ma, S., Zhou, T., Stone, D. A., Polson, D., Dai, A., Stott, P. A., Storch, H. von, Qian, Y., Burke, C., Wu, P., Zou, L., & Ciavarella, A. (2017). Detectable anthropogenic shift toward heavy precipitation over eastern China. *Journal of Climate*. https://doi.org/10.1175/JCLI-D-16-0311.1

Ma, Y., Yang, Y., Mai, X., Qiu, C., Long, X., & Wang, C. (2016). Comparison of Analysis and Spectral Nudging Techniques for Dynamical Downscaling with the WRF Model over China. *Advances in Meteorology*. https://doi.org/10.1155/2016/4761513

Mariotti, A., Pan, Y., Zeng, N., & Alessandri, A. (2015). Long-term climate change in the Mediterranean region in the midst of decadal variability. *Climate Dynamics*. https://doi.org/10.1007/s00382-015-2487-3

Mathbout, S., Lopez-Bustins, J. A., Royé, D., Martin-Vide, J., Bech, J., & Rodrigo, F. S. (2018). Observed Changes in Daily Precipitation Extremes at Annual Timescale Over the Eastern Mediterranean During 1961–2012. *Pure and Applied Geophysics*. https://doi.org/10.1007/s00024-017-1695-7

McSweeney, C. F., Jones, R. G., Lee, R. W., & Rowell, D. P. (2015). Selecting CMIP5 GCMs for downscaling over multiple regions. *Climate Dynamics*. https://doi.org/10.1007/s00382-014-2418-8

Min, S. K., Zhang, X., Zwiers, F. W., & Hegerl, G. C. (2011). Human contribution to more-intense precipitation extremes. *Nature*. https://doi.org/10.1038/nature09763

Minamiguchi, Y., Shimadera, H., Matsuo, T., & Kondo, A. (2018). Numerical simulation of heavy rainfall in August 2014 over Japan and analysis of its sensitivity to sea surface temperature. *Atmosphere*. https://doi.org/10.3390/atmos9030084

Myhre, G., Alterskjær, K., Stjern, C. W., Hodnebrog, Marelle, L., Samset, B. H., Sillmann, J., Schaller, N., Fischer, E., Schulz, M., & Stohl, A. (2019). Frequency of extreme precipitation increases extensively with event rareness under global warming. *Scientific Reports*. https://doi.org/10.1038/s41598-019-52277-4

Nicholson, S. E., Funk, C., & Fink, A. H. (2018). Rainfall over the African continent from the 19th through the 21st century. *Global and Planetary Change*. https://doi.org/10.1016/j.gloplacha.2017.12.014

Nie, J., Shaevitz, D. A., & Sobel, A. H. (2016). Forcings and feedbacks on convection in the 2010 Pakistan flood: Modeling extreme precipitation with interactive large-scale ascent. *Journal of Advances in Modeling Earth Systems*. https://doi.org/10.1002/2016MS000663

Nie, J., Sobel, A. H., Shaevitz, D. A., & Wang, S. (2018). Dynamic amplification of extreme precipitation sensitivity. *Proceedings of the National Academy of Sciences of the United States of America*. https://doi.org/10.1073/pnas.1800357115

Norris, J., Chen, G., & David Neelin, J. (2019). Thermodynamic versus dynamic controls on extreme precipitation in a warming climate from the Community Earth System Model

Large Ensemble. *Journal of Climate*. https://doi.org/10.1175/JCLI-D-18-0302.1

O'Gorman, P. A. (2015). Precipitation Extremes Under Climate Change. In *Current Climate Change Reports*. https://doi.org/10.1007/s40641-015-0009-3

O'Gorman, P. A., & Schneider, T. (2009). The physical basis for increases in precipitation extremes in simulations of 21st-century climate change. *Proceedings of the National Academy of Sciences of the United States of America*. https://doi.org/10.1073/pnas.0907610106

Otto, F. E. L., Van Der Wiel, K., Van Oldenborgh, G. J., Philip, S., Kew, S. F., Uhe, P., & Cullen, H. (2018). Climate change increases the probability of heavy rains in Northern England/Southern Scotland like those of storm Desmond - A real-time event attribution revisited. *Environmental Research Letters*. https://doi.org/10.1088/1748-9326/aa9663

Otto, F. E. L., Wolski, P., Lehner, F., Tebaldi, C., Van Oldenborgh, G. J., Hogesteeger, S., Singh, R., Holden, P., Fučkar, N. S., Odoulami, R. C., & New, M. (2018). Anthropogenic influence on the drivers of the Western Cape drought 2015-2017. *Environmental Research Letters*. https://doi.org/10.1088/1748-9326/aae9f9

Paciorek, C. J., Stone, D. A., & Wehner, M. F. (2018). Quantifying statistical uncertainty in the attribution of human influence on severe weather. *Weather and Climate Extremes*. https://doi.org/10.1016/j.wace.2018.01.002

Paik, S., Min, S. K., Zhang, X., Donat, M. G., King, A. D., & Sun, Q. (2020). Determining the Anthropogenic Greenhouse Gas Contribution to the Observed Intensification of Extreme Precipitation. *Geophysical Research Letters*. https://doi.org/10.1029/2019GL086875

Pall, P., Aina, T., Stone, D. A., Stott, P. A., Nozawa, T., Hilberts, A. G. J., Lohmann, D., & Allen, M. R. (2011). Anthropogenic greenhouse gas contribution to flood risk in England and Wales in autumn 2000. *Nature*. https://doi.org/10.1038/nature09762

Park, C., Min, S. K., Lee, D., Cha, D. H., Suh, M. S., Kang, H. S., Hong, S. Y., Lee, D. K., Baek, H. J., Boo, K. O., & Kwon, W. T. (2016). Evaluation of multiple regional climate models for summer climate extremes over East Asia. *Climate Dynamics*. https://doi.org/10.1007/s00382-015-2713-z

Paul, S., Ghosh, S., Mathew, M., Devanand, A., Karmakar, S., & Niyogi, D. (2018). Increased Spatial Variability and Intensification of Extreme Monsoon Rainfall due to Urbanization. *Scientific Reports*. https://doi.org/10.1038/s41598-018-22322-9

Pendergrass, A. G., Knutti, R., Lehner, F., Deser, C., & Sanderson, B. M. (2017). Precipitation variability increases in a warmer climate. *Scientific Reports*. https://doi.org/10.1038/s41598-017-17966-y

Pfahl, S., O'Gorman, P. A., & Fischer, E. M. (2017). Understanding the regional pattern of projected future changes in extreme precipitation. *Nature Climate Change*. https://doi.org/10.1038/nclimate3287

Prakash, S., Mitra, A. K., Pai, D. S., & AghaKouchak, A. (2016). From TRMM to GPM: How well can heavy rainfall be detected from space? *Advances in Water Resources*. https://doi.org/10.1016/j.advwatres.2015.11.008

Prein, A. F., Rasmussen, R. M., Ikeda, K., Liu, C., Clark, M. P., & Holland, G. J. (2017). The future intensification of hourly precipitation extremes. *Nature Climate Change*. https://doi.org/10.1038/nclimate3168

Qian, Y., Wang, W., Leung, L. R., & Kaiser, D. P. (2007). Variability of solar radiation under cloud-free skies in China: The role of aerosols. *Geophysical Research Letters*. https://doi.org/10.1029/2006GL028800

Raghuraman, S. P., Paynter, D., & Ramaswamy, V. (2021). Anthropogenic forcing and response yield observed positive trend in Earth's energy imbalance. *Nature Communications*. https://doi.org/10.1038/s41467-021-24544-4

Rayner, N. A., Parker, D. E., Horton, E. B., Folland, C. K., Alexander, L. V., Rowell, D. P., Kent, E. C., & Kaplan, A. (2003). Global analyses of sea surface temperature, sea ice, and night marine air temperature since the late nineteenth century. *Journal of Geophysical Research: Atmospheres*. https://doi.org/10.1029/2002jd002670

Rimi, R. H., Haustein, K., Barbour, E. J., & Allen, M. R. (2019). Risks of pre-monsoon extreme rainfall events of Bangladesh: Is anthropogenic climate change playing a role? *Bulletin of the American Meteorological Society*. https://doi.org/10.1175/BAMS-D-18-0152.1

Risser, M. D., & Wehner, M. F. (2017). Attributable Human-Induced Changes in the Likelihood and Magnitude of the Observed Extreme Precipitation during Hurricane Harvey. *Geophysical Research Letters*. https://doi.org/10.1002/2017GL075888

Rosenfeld, D., Lohmann, U., Raga, G. B., O'Dowd, C. D., Kulmala, M., Fuzzi, S., Reissell, A., & Andreae, M. O. (2008). Flood or drought: How do aerosols affect precipitation? In *Science*. https://doi.org/10.1126/science.1160606

Ross, R. J., & Elliot, W. P. (2001). Radiosonde-based Northern Hemisphere tropospheric water vapor trends. *Journal of Climate*. https://doi.org/10.1175/1520-0442(2001)014<1602:RBNHTW>2.0.CO;2

Roxy, M. K., Ghosh, S., Pathak, A., Athulya, R., Mujumdar, M., Murtugudde, R., Terray, P., & Rajeevan, M. (2017). A threefold rise in widespread extreme rain events over central India. *Nature Communications*. https://doi.org/10.1038/s41467-017-00744-9

Sabeerali, C. T., Rao, S. A., Dhakate, A. R., Salunke, K., & Goswami, B. N. (2015). Why ensemble mean projection of south Asian monsoon rainfall by CMIP5 models is not reliable? *Climate Dynamics*. https://doi.org/10.1007/s00382-014-2269-3

Santer, B. D., Mears, C., Wentz, F. J., Taylor, K. E., Gleckler, P. J., Wigley, T. M. L., Barnett, T. P., Boyle, J. S., Brüggemann, W., Gillette, N. P., Klein, S. A., Meehl, G. A., Nozawa, T., Pierce, D. W., Stott, P. A., Washington, W. M., & Wehner, M. F. (2007). Identification of human-induced changes in atmospheric moisture content. *Proceedings of the National Academy of Sciences of the United States of America*. https://doi.org/10.1073/pnas.0702872104

Sato, T., Kimura, F., & Kitoh, A. (2007). Projection of global warming onto regional precipitation over Mongolia using a regional climate model. *Journal of Hydrology*. https://doi.org/10.1016/j.jhydrol.2006.07.023

Schär, C., Frei, C., Lüthi, D., & Davies, H. C. (1996). Surrogate climate-change scenarios for regional climate models. *Geophysical Research Letters*. https://doi.org/10.1029/96GL00265

Seager, R., Naik, N., & Vecchi, G. A. (2010). Thermodynamic and dynamic mechanisms for large-scale changes in the hydrological cycle in response to global warming. *Journal of Climate*. https://doi.org/10.1175/2010JCLI3655.1

Seager, R., Neelin, D., Simpson, I., Liu, H., Henderson, N., Shaw, T., Kushnir, Y., Ting, M., & Cook, B. (2014). Dynamical and thermodynamical causes of large-scale changes in the hydrological cycle over North America in response to global warming. *Journal of Climate*. https://doi.org/10.1175/JCLI-D-14-00153.1

Seong, M. G., Min, S. K., Kim, Y. H., Zhang, X., & Sun, Y. (2021). Anthropogenic greenhouse gas and aerosol contributions to extreme temperature changes during 1951-2015. *Journal of Climate*. https://doi.org/10.1175/JCLI-D-19-1023.1

Shahid, S. (2011). Trends in extreme rainfall events of Bangladesh. *Theoretical and Applied Climatology*. https://doi.org/10.1007/s00704-010-0363-y

Sheikh, M. M., Manzoor, N., Ashraf, J., Adnan, M., Collins, D., Hameed, S., Manton, M. J., Ahmed, A. U., Baidya, S. K., Borgaonkar, H. P., Islam, N., Jayasinghearachchi, D., Kothawale, D. R., Premalal, K. H. M. S., Revadekar, J. V., & Shrestha, M. L. (2015). Trends in extreme daily rainfall and temperature indices over South Asia. *International Journal of Climatology*. https://doi.org/10.1002/joc.4081

Shen, Y., & Xiong, A. (2016). Validation and comparison of a new gauge-based precipitation analysis over mainland China. *International Journal of Climatology*. https://doi.org/10.1002/joc.4341

Shepherd, T. G. (2014). Atmospheric circulation as a source of uncertainty in climate change projections. In *Nature Geoscience*. https://doi.org/10.1038/NGEO2253

Sherwood, S. C., Ingram, W., Tsushima, Y., Satoh, M., Roberts, M., Vidale, P. L., & O'Gorman, P. A. (2010). Relative humidity changes in a warmer climate. *Journal of Geophysical Research Atmospheres*. https://doi.org/10.1029/2009JD012585

Singh, D., Horton, D. E., Tsiang, M., Haugen, M., Ashfaq, M., Mei, R., Rastogi, D., Johnson, N. C., Charland, A., Rajaratnam, B., & Diffenbaugh, N. S. (2014). 17. Severe precipitation in Northern India in June 2013: Causes, historical context, and changes in probability. *Bulletin of the American Meteorological Society*.

Singh, M. S., & O'Gorman, P. A. (2014). Influence of microphysics on the scaling of precipitation extremes with temperature. *Geophysical Research Letters*. https://doi.org/10.1002/2014GL061222

Skamarock WC, et al. (2008). A description of the advanced research WRF version 3, NCAR Tech. Note, NCAR/TN-468+STR. *Natl. Cent. for Atmos. Res. Boulder, Colorado*. https://doi.org/10.5065/D68S4MVH

Song, F., Leung, L. R., Lu, J., & Dong, L. (2018). Future Changes in Seasonality of the North Pacific and North Atlantic Subtropical Highs. *Geophysical Research Letters*.

https://doi.org/10.1029/2018GL079940

Song, F., Leung, L. R., Lu, J., Dong, L., Zhou, W., Harrop, B., & Qian, Y. (2021). Emergence of seasonal delay of tropical rainfall during 1979–2019. *Nature Climate Change*. https://doi.org/10.1038/s41558-021-01066-x

Song, F., Zhou, T., & Qian, Y. (2014). Responses of East Asian summer monsoon to natural and anthropogenic forcings in the 17 latest CMIP5 models. *Geophysical Research Letters*. https://doi.org/10.1002/2013GL058705

Spracklen, D. V., & Garcia-Carreras, L. (2015). The impact of Amazonian deforestation on Amazon basin rainfall. *Geophysical Research Letters*. https://doi.org/10.1002/2015GL066063

Stephens, G. L., L'Ecuyer, T., Forbes, R., Gettlemen, A., Golaz, J. C., Bodas-Salcedo, A., Suzuki, K., Gabriel, P., & Haynes, J. (2010). Dreary state of precipitation in global models. *Journal of Geophysical Research Atmospheres*. https://doi.org/10.1029/2010JD014532

Stone, D. A., & Allen, M. R. (2005). The end-to-end attribution problem: From emissions to impacts. *Climatic Change*. https://doi.org/10.1007/s10584-005-6778-2

Stott, P. A., Christidis, N., Otto, F. E. L., Sun, Y., Vanderlinden, J. P., van Oldenborgh, G. J., Vautard, R., von Storch, H., Walton, P., Yiou, P., & Zwiers, F. W. (2016). Attribution of extreme weather and climate-related events. *Wiley Interdisciplinary Reviews: Climate Change*. https://doi.org/10.1002/wcc.380

Sun, J. Q., & Ao, J. (2013). Changes in precipitation and extreme precipitation in a warming environment in China. *Chinese Science Bulletin*. https://doi.org/10.1007/s11434-012-5542-z

Sun, Q., Zhang, X., Zwiers, F., Westra, S., & Alexander, L. V. (2021). A global, continental, and regional analysis of changes in extreme precipitation. *Journal of Climate*. https://doi.org/10.1175/JCLI-D-19-0892.1

Tabari, H., Madani, K., & Willems, P. (2020). The contribution of anthropogenic influence to more anomalous extreme precipitation in Europe. *Environmental Research Letters*. https://doi.org/10.1088/1748-9326/abb268

Tandon, N. F., Zhang, X., & Sobel, A. H. (2018). Understanding the Dynamics of Future Changes in Extreme Precipitation Intensity. *Geophysical Research Letters*. https://doi.org/10.1002/2017GL076361

Tao, Y., Wang, W., Song, S., & Ma, J. (2018). Spatial and temporal variations of precipitation extremes and seasonality over China from 1961~2013. *Water (Switzerland)*. https://doi.org/10.3390/w10060719

Taylor, K. E., Stouffer, R. J., & Meehl, G. A. (2012). An overview of CMIP5 and the experiment design. In *Bulletin of the American Meteorological Society*. https://doi.org/10.1175/BAMS-D-11-00094.1

Tewari, M., Chen, F., Wang, W., Dudhia, J., LeMone, M. A., Mitchell, K., Ek, M., Gayno, G., Wegiel, J., & Cuenca, R. H. (2004). Implementation and verification of the unified noah

land surface model in the WRF model. *Bulletin of the American Meteorological Society*.

Thompson, G., Field, P. R., Rasmussen, R. M., & Hall, W. D. (2008). Explicit forecasts of winter precipitation using an improved bulk microphysics scheme. Part II: Implementation of a new snow parameterization. *Monthly Weather Review*. https://doi.org/10.1175/2008MWR2387.1

Tian, D., Guo, Y., & Dong, W. (2015). Future changes and uncertainties in temperature and precipitation over China based on CMIP5 models. *Advances in Atmospheric Sciences*. https://doi.org/10.1007/s00376-014-4102-7

Trenberth, K. E. (2011). Changes in precipitation with climate change. *Climate Research*. https://doi.org/10.3354/cr00953

Trenberth, K. E., Dai, A., Rasmussen, R. M., & Parsons, D. B. (2003). The changing character of precipitation. In *Bulletin of the American Meteorological Society*. https://doi.org/10.1175/BAMS-84-9-1205

Trenberth, K. E., Fasullo, J., & Smith, L. (2005). Trends and variability in column-integrated atmospheric water vapor. *Climate Dynamics*. https://doi.org/10.1007/s00382-005-0017-4

Trenberth, K. E., Fasullo, J. T., & Shepherd, T. G. (2015). Attribution of climate extreme events. In *Nature Climate Change*. https://doi.org/10.1038/nclimate2657

Trenberth, K. E., & Zhang, Y. (2018). How often does it really rain? *Bulletin of the American Meteorological Society*. https://doi.org/10.1175/BAMS-D-17-0107.1

Trenberth, K. E., Zhang, Y., & Gehne, M. (2017). Intermittency in precipitation: Duration, frequency, intensity, and amounts using hourly data. *Journal of Hydrometeorology*. https://doi.org/10.1175/JHM-D-16-0263.1

Ueda, H., Iwai, A., Kuwako, K., & Hori, M. E. (2006). Impact of anthropogenic forcing on the Asian summer monsoon as simulated by eight GCMs. *Geophysical Research Letters*. https://doi.org/10.1029/2005GL025336

van Oldenborgh, G. J., van der Wiel, K., Sebastian, A., Singh, R., Arrighi, J., Otto, F., Haustein, K., Li, S., Vecchi, G., & Cullen, H. (2018). Corrigendum: Attribution of extreme rainfall from Hurricane Harvey, August 2017 (2017 Environ. Res. Lett. 12 124009) . *Environmental Research Letters*. https://doi.org/10.1088/1748-9326/aaa343

Vautard, R., Yiou, P., Otto, F., Stott, P., Christidis, N., Van Oldenborgh, G. J., & Schaller, N. (2016). Attribution of human-induced dynamical and thermodynamical contributions in extreme weather events. *Environmental Research Letters*. https://doi.org/10.1088/1748-9326/11/11/114009

Wang, B., & Ding, Q. (2006). Changes in global monsoon precipitation over the past 56 years. *Geophysical Research Letters*. https://doi.org/10.1029/2005GL025347

Wang, S. Y. S., Zhao, L., Yoon, J. H., Klotzbach, P., & Gillies, R. R. (2018). Quantitative attribution of climate effects on Hurricane Harvey's extreme rainfall in Texas. *Environmental Research Letters*. https://doi.org/10.1088/1748-9326/aabb85

Wang, S., & Zuo, H. (2016). Effect of the East Asian westerly jet's intensity on summer rainfall in the Yangtze River valley and its mechanism. *Journal of Climate*. https://doi.org/10.1175/JCLI-D-15-0259.1

Watterson, I. G. (2008). Calculation of probability density functions for temperature and precipitation change under global warming. *Journal of Geophysical Research Atmospheres*. https://doi.org/10.1029/2007JD009254

Westra, S., Fowler, H. J., Evans, J. P., Alexander, L. V., Berg, P., Johnson, F., Kendon, E. J., Lenderink, G., & Roberts, N. M. (2014). Future changes to the intensity and frequency of short-duration extreme rainfall. In *Reviews of Geophysics*. https://doi.org/10.1002/2014RG000464

Willett, K. M., Gillett, N. P., Jones, P. D., & Thorne, P. W. (2007). Attribution of observed surface humidity changes to human influence. *Nature*. https://doi.org/10.1038/nature06207

Willner, S. N., Otto, C., & Levermann, A. (2018). Global economic response to river floods. *Nature Climate Change*. https://doi.org/10.1038/s41558-018-0173-2

Wu, M., Luo, Y., Chen, F., & Wong, W. K. (2019). Observed link of extreme hourly precipitation changes to urbanization over coastal South China. *Journal of Applied Meteorology and Climatology*. https://doi.org/10.1175/JAMC-D-18-0284.1

Wyser, K., Kjellström, E., Koenigk, T., Martins, H., & Döscher, R. (2020). Warmer climate projections in EC-Earth3-Veg: The role of changes in the greenhouse gas concentrations from CMIP5 to CMIP6. *Environmental Research Letters*. https://doi.org/10.1088/1748-9326/ab81c2

Xiao, C., Wu, P., Zhang, L., & Song, L. (2016). Robust increase in extreme summer rainfall intensity during the past four decades observed in China. *Scientific Reports*. https://doi.org/10.1038/srep38506

Xuan, S., Zhang, Q., & Sun, S. (2011). Anomalous midsummer rainfall in Yangtze River-Huaihe River valleys and its association with the East Asia westerly jet. *Advances in Atmospheric Sciences*. https://doi.org/10.1007/s00376-010-0111-3

Yang, B., Qian, Y., Lin, G., Leung, R., & Zhang, Y. (2012). Some issues in uncertainty quantification and parameter tuning: A case study of convective parameterization scheme in the WRF regional climate model. *Atmospheric Chemistry and Physics*. https://doi.org/10.5194/acp-12-2409-2012

Yihui, D., Ren, G., Guangyu, S., Peng, G., Zheng, X., Zhai, P., er, Z., Zhao, Z.-C., Shaowu, W., Huijun, W., Luo, Y., & Chen, D. (2007). China's National Assessment Report on Climate Change (I): Climate change in China and the future trend. *Adv. Clim. Change Res.*, 1–5.

Yiou, P., Jézéquel, A., Naveau, P., Otto, F. E. L., Vautard, R., & Vrac, M. (2017). A statistical framework for conditional extreme event attribution. *Advances in Statistical Climatology, Meteorology and Oceanography*. https://doi.org/10.5194/ascmo-3-17-2017

Yuan, X., Wang, S., & Hu, Z.-Z. (2018). Do Climate Change and El Niño Increase Likelihood

of Yangtze River Extreme Rainfall? [in "Explaining Extreme Events of 2016 from a Climate Perspective"]. *Bulletin of the American Meteorological Society*.

Yun, Y., Liu, C., Luo, Y., Liang, X., Huang, L., Chen, F., & Rasmmusen, R. (2020). Convection-permitting regional climate simulation of warm-season precipitation over Eastern China. *Climate Dynamics*. https://doi.org/10.1007/s00382-019-05070-y

Zhai, P., Zhang, X., Wan, H., & Pan, X. (2005). Trends in total precipitation and frequency of daily precipitation extremes over China. *Journal of Climate*. https://doi.org/10.1175/JCLI-3318.1

Zhang, C., Wang, Y., Hamilton, K., & Lauer, A. (2016). Dynamical downscaling of the climate for the Hawaiian islands. Part II: Projection for the late twenty-first century. *Journal of Climate*. https://doi.org/10.1175/JCLI-D-16-0038.1

Zhang, Q., Singh, V. P., Sun, P., Chen, X., Zhang, Z., & Li, J. (2011). Precipitation and streamflow changes in China: Changing patterns, causes and implications. *Journal of Hydrology*. https://doi.org/10.1016/j.jhydrol.2011.09.017

Zhang, Q., Zheng, Y., Singh, V. P., Luo, M., & Xie, Z. (2017). Summer extreme precipitation in eastern China: Mechanisms and impacts. *Journal of Geophysical Research*. https://doi.org/10.1002/2016JD025913

Zhang, W., & Zhou, T. (2019). Significant increases in extreme precipitation and the associations with global warming over the global land monsoon regions. *Journal of Climate*. https://doi.org/10.1175/JCLI-D-18-0662.1

Zhang, X., Wan, H., Zwiers, F. W., Hegerl, G. C., & Min, S. K. (2013). Attributing intensification of precipitation extremes to human influence. *Geophysical Research Letters*. https://doi.org/10.1002/grl.51010

Zhang, X., Zwiers, F. W., Li, G., Wan, H., & Cannon, A. J. (2017). Complexity in estimating past and future extreme short-duration rainfall. *Nature Geoscience*. https://doi.org/10.1038/ngeo2911

Zhao, T., & Yatagai, A. (2014). Evaluation of TRMM 3B42 product using a new gauge-based analysis of daily precipitation over China. *International Journal of Climatology*. https://doi.org/10.1002/joc.3872

Zhong, S., Qian, Y., Zhao, C., Leung, R., Wang, H., Yang, B., Fan, J., Yan, H., Yang, X. Q., & Liu, D. (2017). Urbanization-induced urban heat island and aerosol effects on climate extremes in the Yangtze River Delta region of China. *Atmospheric Chemistry and Physics*. https://doi.org/10.5194/acp-17-5439-2017

Zhou, T., Ren, L., & Zhang, W. (2021). Anthropogenic influence on extreme Meiyu rainfall in 2020 and its future risk. *Science China Earth Sciences*. https://doi.org/10.1007/s11430-020-9771-8

Zhou, T., Zhang, L., & Li, H. (2008). Changes in global land monsoon area and total rainfall accumulation over the last half century. *Geophysical Research Letters*. https://doi.org/10.1029/2008GL034881

Zhou, T., Zhang, W., Zhang, L., Zhang, X., Qian, Y., Peng, D., Ma, S., & Dong, B. (2020). The dynamic and thermodynamic processes dominating the reduction of global land monsoon precipitation driven by anthropogenic aerosols emission. *Science China Earth Sciences*. https://doi.org/10.1007/s11430-019-9613-9

Zhu, H., Jiang, Z., Li, J., Li, W., Sun, C., & Li, L. (2020). Does CMIP6 Inspire More Confidence in Simulating Climate Extremes over China? *Advances in Atmospheric Sciences*. https://doi.org/10.1007/s00376-020-9289-1